Biophysical responses of lymphocytes to environmental stress

by

Vivian Hecht

B.S. Bioengineering, University of California, Los Angeles (2010)

Submitted to the Department Of Biological Engineering in Partial Fulfillment of the Requirements for the Degree of

Doctor of Philosophy

at the

Massachusetts Institute of Technology

February 2016

Signature of Author: Signature redacted
Department of Biological Engineering
September 17, 2015

Certified by: Signature redacted
Scott R. Manalis
Professor of Biological and Mechanical Engineering

Accepted by: Signature redacted
Forest White
Graduate Program Chair

Thesis committee members in favor of defense:

Professor John Essigmann

Professor Matthew Vander Heiden

Professor Scott Manalis

Biophysical responses of lymphocytes to environmental stress

By
Vivian Hecht
Submitted to the Department of Biological Engineering
On September 17, 2015, in partial fulfillment of the
Requirements for the degree of
Doctor of Philosophy in Biological Engineering

Abstract

Cellular biophysical properties both reflect and influence cell state. These parameters represent the consequences of the interactions of multiple molecular events, and thus may reveal information otherwise obscured when measuring individual pathways in isolation. Previous work has demonstrated how precise measurements of certain of these properties, such as mass, volume, density and deformability using a suspended microchannel resonator (SMR) can help characterize cellular behavior and physiological role. Here, we expand upon this previous work to demonstrate the necessity of measuring multiple parameters simultaneously to fully determine cellular responses to environmental perturbations, and describe a situation in which changes to density and size promote survival under conditions of limited nutrient availability.

We first investigate the relationship between cell density, volume, buoyant mass, and passage time through a narrow constriction under a variety of environmental stresses. Osmotic stress significantly affects density and volume, as previously shown. In contrast to density and volume, the effect of an osmotic challenge on passage time is relatively small. Deformability, determined by comparing passage times for cells with similar volume, exhibits a strong dependence on osmolarity, indicating that passage time alone does not always provide a meaningful proxy for deformability. Finally, we find that protein synthesis inhibition, cell cycle arrest, protein kinase inhibition, and cytoskeletal disruption result in unexpected relationships between deformability, density, and volume. Taken together, our results suggest that measuring multiple biophysical parameters can detect unique characteristics that more specifically reflect cellular behaviors.

We next examine how cellular biophysical changes occurring immediately after growth factor depletion in lymphocytes promote adaptation to reduced nutrient uptake. We describe an acute biophysical response to growth factor withdrawal, characterized by a simultaneous decrease in cell volume and increase in cell density prior to autophagy initiation, observed in both FL5.12 cells depleted of IL-3 and primary CD8+ T cells depleted of IL-2 and differentiating towards memory cells. The response reduces cell surface area to minimize energy expenditure while conserving biomass, suggesting that the biophysical properties of cells can be regulated to promote survival under conditions of nutrient stress.

Acknowledgements

I would first and foremost like to thank Professor Scott Manalis for his guidance and mentorship during the course of my thesis work. His dedication and enthusiasm helped me succeed and I am very fortunate to have had the chance to work with him. My thesis committee members, Professors John Essigmann and Matthew Vander Heiden, were sources of valuable feedback and perspectives regarding the progress of my work. I would also like to thank Matt for sharing his biological expertise in the area of growth factor dependence in lymphocytes, as well as providing me with the opportunity to collaborate closely with his lab.

Next, I would like to thank the members of the Manalis lab, past and present, an exceptionally talented group of individuals who made for truly excellent colleagues. Andrea Bryan, who trained me when I first arrived, set an excellent example for me and has continued to be a mentor and friend since then. Will Grover continually encouraged me and helped me troubleshoot the dual SMR. Will and Andrea together pioneered the SMR density measurement, enabling me to use the method to answer the biological questions addressed in this work. Sangwon Byun's thoughtful and careful approach to the deformability and density project were essential to its success. Edgar Aranda-Michel and Kevin Hu contributed both their image processing talents and positive outlooks, generating sufficient momentum to push through the challenging periods of developing the affinity chip. Josephine Bagnall was a source of both technical and moral support, and I was very happy to have her as a teammate in the ladies' section during lab meetings. Selim Olcum and Nate Cermak demonstrated unwavering patience and dedication in ensuring that my SMR setup function properly, and always found time to help me identify issues with

electronics in spite of being constantly bombarded with questions from other lab members. Scott Knudsen was a constant source of a wide breadth of useful and entertaining knowledge, and I am indebted to him for both solving many SMR-related problems and sharing with me fascinating science trivia. Mark Stevens and Rob Kimmerling provided invaluable biological guidance as well as comic relief; Rob's input during the affinity chip project was tremendously helpful.

I am also grateful for the support of multiple collaborators. Lucas Sullivan served as a translator and guide through the fascinating and often confusing depths of mammalian cell biology and metabolism. Dong-Hwee Kim's imaging expertise provided a useful complement to our biophysical measurements. Greg Szeto was always willing to share his encyclopedic knowledge of immunology, and provided invaluable support during the affinity chip project.

Finally, I would like to thank my friends and family for their continued support during the course of my thesis work. My parents, who encouraged me from the very beginning, and always reminded to persevere no matter how seemingly difficult the challenge. My older brother, Ariel, first introduced me to microfluidics, and set a stellar example for me to follow; my younger brother, Avi, was always willing to listen to any of my concerns and propose the most reasonable solution. And last of all, I would like to thank my husband, Aaron, whose kindness, patience and sense of humor made this entire work possible.

Contents

List of figures

List of tables

Chapter 1

Introduction

1.1 The interplay between cellular composition and behavior

Cellular composition, describing the relative amounts of all intracellular biomolecular components, is a parameter often predicated upon physiological role. For example, adipocytes, which serve primarily as lipid storage centers, have a high fraction of triglycerides and cholesterol esters. Conversely, myocytes, the cells comprising muscle tissue, contain high levels of glycogen, a readily accessible source of energy, and mitochondria, for generating ATP. As the need for space for energy storage or strength changes, the composition of these cells will adjust accordingly.

In other cases, however, cellular composition can influence specific cellular behaviors. For example, the hormone insulin, released due to elevated blood glucose levels, stimulates cellular ion channels to increase water uptake (1, 2). This increase in cell water content leads to an increase in cell volume that has been shown to upregulate anabolic processes, such as glycogen synthesis, and downregulate catabolic processes, such as gluconeogenesis. Glucagon, released when blood glucose levels decrease, causes the opposite effect, decreasing cell volume and upregulating catabolic processes. Furthermore,

certain neurodegenerative diseases, including Alzheimer's disease, Parkinson's disease, Huntington's disease and amyotrophic lateral sclerosis, are characterized by accumulation of protein aggregates in various categories of neuronal cells. These protein aggregates, caused by stochastic processes, aging, or overexpression of genes responsible for synthesis of specific proteins, tend to overwhelm the native cellular protein degradation machinery (3).

The close relationship between cellular composition and cellular behavior suggests the need to tightly regulate composition to ensure the proper function of cellular machinery. This is made especially clear when considering the significant level of cytoplasmic macromolecular crowding (4). Shifts in concentrations of both macromolecules actively participating in reactions and bystander or inert macromolecules can influence cellular reaction rates and protein equilibria (5). For example, while a higher level of crowding will lead to a decreased reaction rate in diffusion-limited reactions, it will also increase the rate of transition state-limited processes. Furthermore, proteins associated with certain misfolding diseases have been shown to be more likely to form aggregates with increasing total cytoplasmic concentration (6).

To more completely characterize a cell from a biophysical standpoint, its cellular composition must be considered in the context of its size. Size can be described using a variety of parameters, including volume, mass, and buoyant mass (i.e. the mass of a particle measured in a fluid). One of the most fundamental reasons for changes to cell size is progression through the cell cycle, as cellular macromolecules, organelles, and genetic material must be replicated to provide sufficient material for two viable daughter cells. This results in an increase in size until a division event; however, whether any changes occur to the overall composition is not entirely clear, and may depend on cell or organism

type (7, 8). Increases in size caused by physiological need rather than cell cycle stage also occur regularly in certain cell types—for example, kidney and bladder cells will swell or shrink due to changes in water uptake, to maintain an appropriate systemic osmolarity. During apoptosis, certain cell types will undergo changes to volume, likely driven by changes to water content, prior to blebbing and membrane permeabilization (9, 10). Furthermore, lymphocytes will increase in size following activation, and decrease in size during the process of differentiation to memory; the changes to composition that are associated with this process are discussed in greater detail in Chapter 3.

In spite of the significant role that composition and size play in cellular function, many studies disregard these properties in favor of focusing on individual molecular pathways. However, a significant fraction of physiological events occur as a result of the contributions of and interactions between multiple pathways, not all of which can be identified *a priori*. Because composition and size are by nature aggregate parameters, they can, therefore, reveal information about cell state that is obscured when considering individual pathways in isolation.

1.1.1 Methods for determining size and composition

Perhaps the most rudimentary method for determining cellular composition is with direct mass measurements. This technique, still commonly practiced, involves weighing a cell pellet with a previously quantified number of cells, drying the pellet in an oven for 24-48 h, and finally weighing the dried pellet (11). The dry mass and water content per cell can then be calculated. However, this approach is time intensive, limited in precision, and unsuitable for identifying any subpopulations or individual outliers in a sample. Measuring large numbers of cells can reduce the measurement error, but this precludes

applying the technique to rare samples. Furthermore, the substantial amount of cell handling can stress the cell sample and introduce biological artifacts. Finally, once the cells are measured in this method, they are no longer viable and cannot be grown further and analyzed with downstream experiments.

Measuring composition and size with microscopy overcomes many of the shortcomings of direct mass measurements. Particularly useful is interferometry, a microscopic technique in which the phase shift between the wavelengths of two beams of light—one a reference and the other emitted from a sample—is used to obtain information about the sample. This phase shift is caused by a difference between the refractive indices of the reference and the sample. The refractive index in cells is directly proportional to biochemical content, or dry mass; thus, with interferometry, the dry mass of cells can be precisely quantified (12–14). Interferometry has also been used to determine changes in water content of kidney cells (15). More recently, this technique has been adapted to dynamically quantify changes in dry mass of growing cells (16). Using the optically calculated volume and dry mass, a dry mass density can be obtained; this is a measure of the amount of dry mass per total volume. However, interferometry cannot be used to determine absolute water content, and it does not provide information about the composition or chemical makeup of the dry mass. Furthermore, this technique relies on a constant refractive index for all biomolecules in the cell; this assumption holds true for most proteins, but is not always valid for carbohydrates and lipids (17).

Raman spectroscopy, an alternative technique, has proven to be particularly well-suited for determining the chemical composition of cellular dry mass. The method involves illuminating a sample with a monochromatic light source, and measuring the scattered light that is of a different frequency than the incident light. This inelastic scattering is

caused by some fraction of the light interacting with the bonds in the molecules of the specimen. The nature of these interactions depends on the identity of the atoms in the molecule and their arrangement in bonds; thus, the spectrum of frequencies reflects the structure and composition of the molecule. Classes of biomolecules are characterized by specific functional groups, and so the peaks that appear in a Raman spectrum can be traced back to their biomolecules of origin. A stronger signal at a given frequency, represented by a larger peak, suggests that the molecule is present in a greater amount.

In general, however, Raman is best suited for comparative analysis, or for determining the structure of single proteins and molecules; obtaining precise, quantitative values for the total dry mass in a cell can be challenging. Another feature of Raman spectroscopy is its weak signal from water (18, 19). Consequently, any water in a sample will not interfere with signal acquisition of chemical components. However, this limits Raman to measuring biochemical components exclusively, and precludes it from use in determining cellular aqueous content.

Recently, a method has been developed which combines Raman spectroscopy with quantitative phase microscopy, allowing for simultaneous measurement on a pixel-by-pixel basis of the morphology of a cell and its chemical composition (20, 21). This method allows for simultaneous size and composition determination, with a high resolution of information in both. However, this high resolution limits the throughput, rendering the technique suitable for only specific applications.

1.1.2 Single-cell density

We focus on the application of cell density, or the ratio of cell mass to volume, as a proxy for cellular composition. Density reflects the combined contribution of all biochemical

components and water; while density, independently of other metrics, cannot be used to determine the amounts of individual components, it can be used to differentiate between populations of cells, and changes to density typically suggest changes to cellular composition. Previous studies have shown that density can be used to identify circulating tumor cells, distinguish among different populations of liver cell types, differentiate between proliferating and non-proliferating cells, and differentiate between healthy and diseased red blood cells (22–24). Here, we demonstrate the application of density to address fundamental biophysical questions relating to cell state. We combine extremely precise measurements of density with those of volume, size, and deformability, and with orthogonal assays, to provide novel insights into cellular responses to environmental perturbations and nutrient stress, and propose possible biological mechanisms underlying the changes to density that we observe.

1.2 Measuring density with a suspended microchannel resonator

1.2.1 Principle of operation

The SMR, or suspended microchannel resonator, is a cantilever-based mass sensor with an embedded microfluidic flow channel. The principles of its operation have been described at length elsewhere, and will be summarized here (25–30). The SMR consists of a hollow resonating cantilever flanked by two bypass channels. A cell is introduced from a bypass channel via pressure-driven-flow, and flows across the cantilever, changing the cantilever mass. The resonance frequency of the cantilever is based on its mass, and the event of a cell passing through will lead to a change in resonance frequency that is

monitored via a feedback circuit. This change in frequency corresponds to the buoyant mass of the cell, or the mass of a cell in its surrounding fluid:

$$m_B = m_{cell}(1 - \frac{\rho_f}{\rho_{cell}}) \quad \textbf{1.2-1.}$$

where m_B corresponds to cell buoyant mass, m_{cell} corresponds to total cell mass, ρ_f corresponds to the density of the surrounding fluid, and ρ_{cell} corresponds to the cell density. This equation can be rewritten to describe buoyant mass in terms of cell volume, V_{cell}, as well:

$$m_B = V_{cell}(\rho_{cell} - \rho_f) \quad \textbf{1.2-2.}$$

The buoyant mass of a cell is related to the change in cantilever resonance frequency via calibration with polystyrene beads of known mass, calculated from the diameter reported by the manufacturer and the density of polystyrene (1.05 g/mL). Similarly, the density of the measurement fluid can be determined with a calibration of fluids of known densities, obtained here from solutions of NaCl in water. Thus, the total mass, volume and density of a cell can be determined by measuring the buoyant mass of a single cell in two fluids of two different densities (Figure **1.2-1**). This method is based on Archimedes' Principle, in which the eponymous philosopher determined the purity of a gold crown by weighing it once in air and once in water, and comparing the result to pure gold weighed in both fluids.

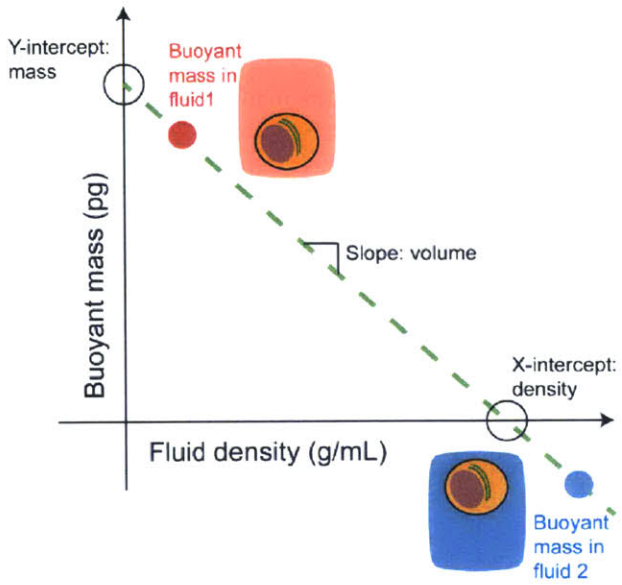

Figure 1.2-1. Calculating single-cell mass, volume, and density.
Cell buoyant mass is measured in two fluids of different densities (red and blue dots) to determine the linear relationship between buoyant mass and fluid density. The absolute mass (y-intercept), volume (slope), and density (x-intercept) of the cell can then be calculated.

1.2.1.1 Measuring aqueous and non-aqueous content

More recently, a method to determine additional information regarding cellular biochemical content using the SMR has been developed (30, 31). Cells are measured with the technique described in §1.2.1, though with PBS and D_2O-PBS (1x PBS in 90% D_2O) as the low and high-density fluids, respectively (Figure 1.2-2). The cell membrane is permeable to D_2O-PBS, and so when a cell is measured in D_2O-PBS, its aqueous content is replaced with D_2O-PBS. This produces a buoyant mass measurement representative of the buoyant mass of the non-aqueous material exclusively. Similarly, when the cell is measured in PBS, we can approximate that the composition of the intracellular aqueous content to be similar to PBS; thus, a buoyant mass measurement in PBS would also represent the buoyant mass of the dry material. The cell buoyant masses in PBS and PBS-D_2O can then be used to determine a mass, volume and density of cellular dry material.

This dry material includes lipids, proteins, nucleic acids, polysaccharides, and other small molecules. The interpretation of dry mass and volume is relatively straightforward—i.e. how much the biochemical content weighs and how much space it occupies. The dry density can be understood to represent the weighted average of the densities of the individual biochemical components. Thus, dry density can be considered a proxy for cellular biochemical composition.

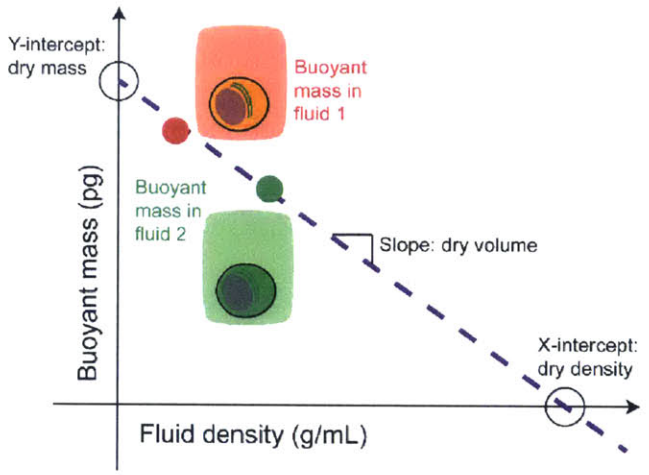

Figure 1.2-2. Calculating single-cell dry mass, volume, and density.
Cell buoyant mass is measured in two fluids of different densities, both permeable to the cell membrane (red and green dots), to determine the linear relationship between buoyant mass and fluid density. The dry mass (y-intercept), volume (slope), and density (x-intercept) of the cell can then be calculated.

Finally, by combining information from the dry density, mass and volume with that of the total (i.e. aqueous and dry) density, mass and volume, the aqueous content of a cell can be estimated. The procedure for determining this value has been described elsewhere, and is summarized below (30, 31).

We start by describing the total mass of the cell (m_{tot}) as composed of aqueous (m_{water}) and dry (m_{dry}) material:

$$m_{tot} = m_{water} + m_{dry}$$

1.2-3

We can rewrite this equation in terms of density and volume, based on the general relationship between mass (m), density (ρ) and volume (V):

$$m = \rho V$$

1.2-4

$$\rho_{tot} V_{tot} = \rho_{water} V_{water} + \rho_{dry} V_{dry}$$

1.2-5

where ρ_{tot}, ρ_{water} and ρ_{dry} refer to the density of the total cellular, aqueous, and dry material, respectively, and V_{tot}, V_{water} and V_{dry} refer to the volume of the total, aqueous, and dry material. We can also describe the volume of the cell in a manner similar to Equation 1.2-3:

$$V_{tot} = V_{water} + V_{dry}$$

1.2-6

By combining equations 1.2-5 and 1.2-6, and assuming a water density of 1 g/mL, we can obtain expressions for the amount of aqueous material, described in terms of volume:

$$V_{water} = V_{tot}\left(1 - \left(\frac{\rho_{tot} - 1}{\rho_{dry} - 1}\right)\right)$$

1.2-7

If we continue using the assumption that the density of water is approximately 1 g/mL, then the value provided by equation 1.2-7 also describes the total mass of water (m_{water}).

The dry density measurement is associated with a number of limitations. First, it is susceptible to relatively high levels of uncertainty due to measurement errors, as discussed further in §1.2.3.11.2.3. Additionally, the process of water/D_2O exchange is not entirely clear. Though the exchange occurs approximately instantaneously for mammalian cells, whether all water is exchanged or simply free water in the cytoplasm remains to be determined. This poses a challenge primarily when applying a direct, mechanistic

interpretation for changes to dry density, as the density of the individual components may not be immediately obvious. Nonetheless, dry density may be a useful indicator of changes to cellular composition, and may be more clearly interpreted when combined with an orthogonal measurement of chemical composition, such as interferometry or Raman spectroscopy.

1.2.2 Single and dual cantilever methods for measuring density

Determining cell density by measuring the mass of a single cell in two different fluids can be accomplished in a number of ways. The two which will be discussed here are a single-cantilever method (32) and a dual cantilever method (33). Both methods involve measuring a cell in a low-density fluid (Fluid 1), typically cell media, and a second fluid (Fluid 2), which is a mix of a small part of cell media and a high density fluid. In initial studies, Percoll, a suspension of silica nanoparticles, was chosen as the high density fluid, due to its biocompatibility and common use in density gradient centrifugation (34, 35). However, upon closer investigation, Percoll was found to be hyperosmolar, and therefore required adjustment using appropriate amounts of powdered cell media and water to ensure accurate measurements (33). Furthermore, the small silica nanoparticles were sufficiently large to produce a measurable signal on the SMR, leading to a noisy baseline, and had a propensity to aggregate and precipitate from the solution, resulting in clogs that interfered with proper device operation.

As an alternative to Percoll, we selected Optiprep, a commercially available solution of 60% iodixanol, used often as a contrast agent for X-ray imaging (36). Though iodixanol appears to change osmolarity in a non-linear fashion when used at a high concentration, we determined that a 30% solution of Optiprep in either cell media or PBS was isoosmolar

(Table 1.2-1) (37). The Optiprep-media solution proved to be much cleaner than Percoll, and its use solved many of the issues initially encountered with the density measurement.

Table 1.2-1. Expected and measured values of osmolarity of Optiprep solutions at a range of concentrations.

PBS:Optiprep:water	Expected osmolarity assuming an Optiprep osmolarity of 387 mOsm/L	Expected osmolarity assuming an Optiprep osmolarity of 206 mOsm/L	Measured osmolarity (mOsm/L)
0:1:0	387	206	206
1:0:0	300	300	309
0:1:9	38.7	20.6	87
1:1:8	338.7	320.6	331
1:2:7	377.4	341.2	365
1:3:6	416.1	361.8	392
1:4:5	454.8	382.4	425
0.7:1:8.3	248.7	230.6	247
0.5:1:8.5	188.7	170.6	203
0.25:1:8.75	113.7	95.6	143

1.2.2.1 Measuring density with a single cantilever

The single-cantilever density method was initially described by Grover et al, 2011 (32). The SMR is filled with Fluid 1 in the left-hand bypass channel and Fluid 2 in the right-hand bypass channel (Figure 1.2-3). A cell sample of 500 μL of approximately 2.5 x 10^5 cells/mL is loaded into the left-hand bypass channel. The pressure is adjusted such that a single cell is directed to pass from the left-hand bypass, through the cantilever, and towards the right-hand bypass channel, where it is immersed in Fluid 2. As the cell passes through the cantilever this first time, its buoyant mass in Fluid 1 is measured. The pressure is again adjusted to reverse the flow, thereby directing the cell from the right-hand bypass channel towards the cantilever entrance. The cell then passes through the SMR a second time, during which its buoyant mass in Fluid 2 is measured. Once the cell

re-enters the left-hand bypass channel, it is flushed towards a waste vial, and a new cell is subsequently loaded into the cantilever. A schematic of the single SMR fluidic arrangement in shown in Figure 1.2-4. Cell samples are typically measured for a period of 60-120 minutes. As a validation of measurement accuracy, the volume of a sample of cells measured on the SMR is compared to the population measured on a commercial Coulter counter. Additionally, each dataset is evaluated to ensure that no drifts in density or volume occur over the time course of a measurement (Figure 1.2-5). Drifts in volume are typically caused by larger cells settling in the tubing or in the sample vials. To avoid biasing the measurement, new sample is periodically introduced by flushing the bypasses at relatively high pressure to introduce new sample. Drifts in density are typically caused by a perturbation to cell state, for example due to cells not being in a temperature and humidity controlled environment. We have found that as long as we measure our samples for two hours or less, the cells do not display any measurable change in density. Experiments are controlled via a custom LabVIEW program, and data is processed using a custom MATLAB script.

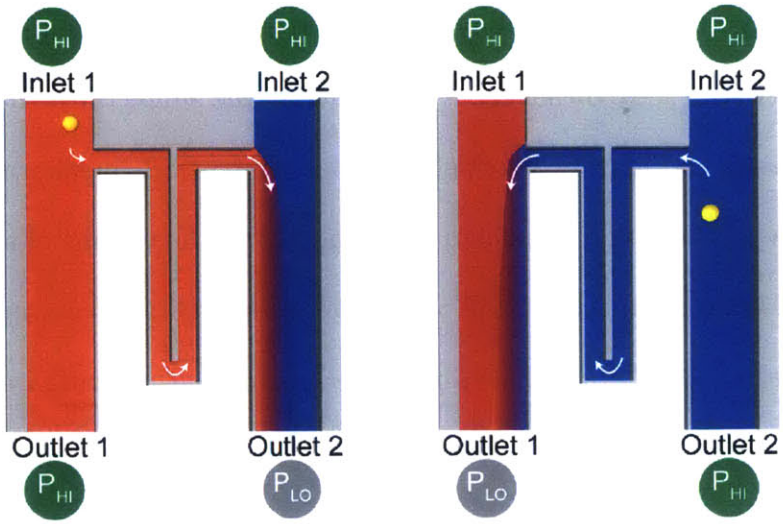

Figure 1.2-3. Schematic of the single SMR density measurement.
Applied pressure is indicated by green (high) and gray (low) circles. A cell (yellow sphere) is introduced from the left-hand bypass channel, which is filled with cell media (Fluid 1, red), and is directed into the embedded cantilever channel. The cell then flows through the cantilever, where its buoyant mass in Fluid 1 is measured. After a slight delay (~200 ms), which allows the cell to travel a short distance down the right-hand bypass channel, the pressure is then switched to reverse the direction of fluid flow. The cell, now immersed in Fluid 2 (blue) then travels in the opposite direction across the cantilever, and its buoyant mass in Fluid 2 is measured. Fluid 2 is typically a mixture of Optiprep and cell media.

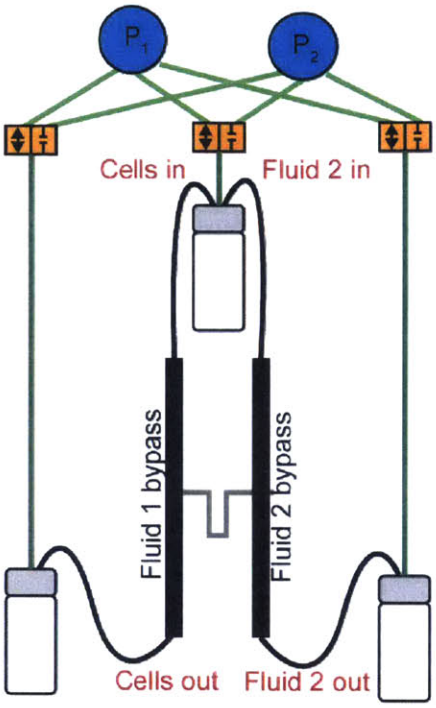

Figure 1.2-4. Diagram of the fluidic and pressure components in the single SMR. Solenoid valves (orange rectangles) set waste vial pressures to those of the pressure regulators (blue circles). Black lines indicate fluidic tubing, and green lines indicate pneumatic tubing.

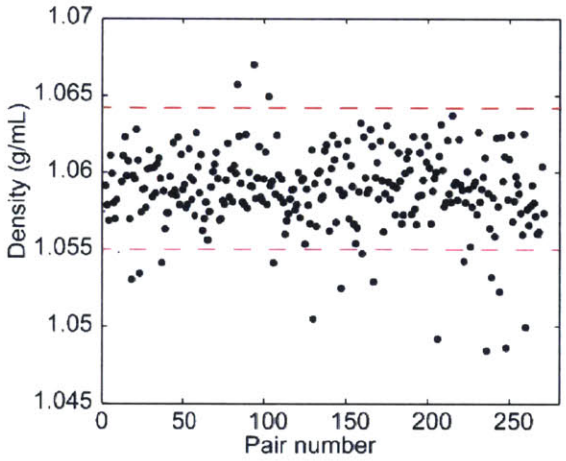

Figure 1.2-5. Changes in density values over the duration of a measurement. The mean density value does not change significantly over the duration of the measurement (approximately 2 h). Red lines indicate approximate bounds of distribution.

1.2.2.2 Measuring density with a dual cantilever

The dual cantilever method was initially described in Bryan, 2011, and in greater detail in Bryan et al, 2014 (33, 38) as an alternative to the single SMR that allows for

multiple density measurements to be made simultaneously. Placing two cantilevers in series eliminates the requirement for the waiting period to measure the buoyant mass of a cell in Fluid 2. To measure the buoyant mass of single cells in two different density fluids in a continuous flow format, devices with two fluidically connected and simultaneously operated SMRs were fabricated and tested (Figure 1.2-6). During operation of the dual SMR, a dilute cell population suspended in cell media (Fluid 1), is delivered to the sample bypass via pressure-driven flow (Figure 1.2-6 and Figure 1.2-7), and single cells flow into the first SMR (SMR_1) for the first buoyant mass measurement. The cells then travel through a microchannel to a cross-junction, where a high density fluid is introduced. After the cross-junction, cells continue through a long serpentine channel, which facilitates mixing of the two fluids. The cells next enter a second cantilever (SMR_2) for a buoyant mass measurement in the mixed fluid (Fluid 2). As cells flow through each cantilever, a change in resonance frequency is recorded, which is determined by each cell's buoyant mass in each cantilever's corresponding fluid.

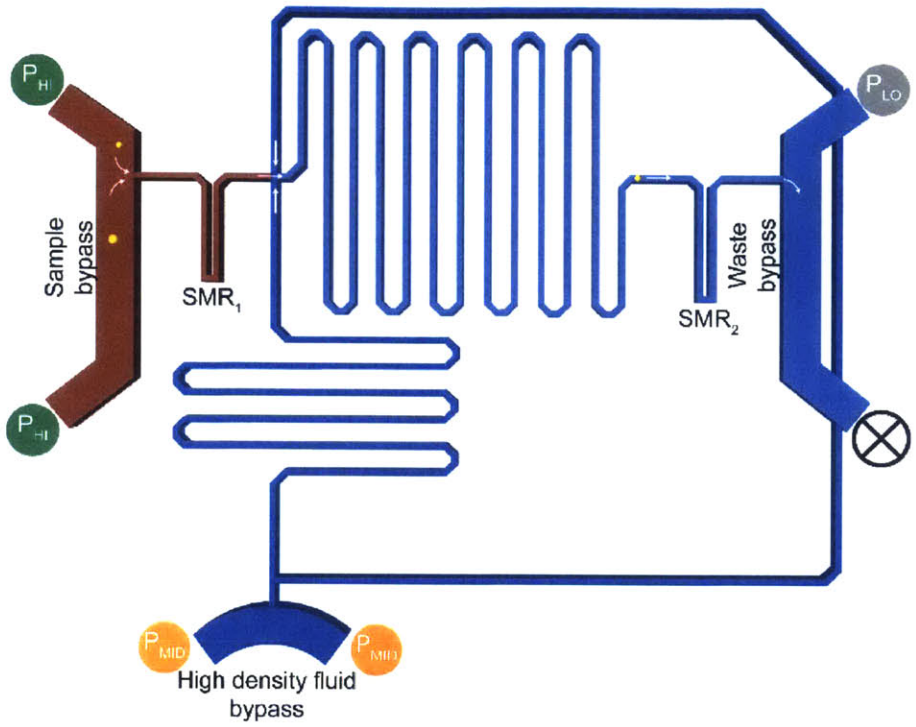

Figure 1.2-6. Schematic of the dual SMR measurement.
A single cell flows from the sample bypass channel into the first SMR (SMR_1) for a buoyant mass measurement in Fluid 1 (red), typically cell media. The cell then continues to a cross-junction where a high density fluid (blue) is introduced and mixes with Fluid 1 via diffusion in the serpentine channel. The second buoyant mass measurement is recorded as the particle flows through the second SMR (SMR_2) in this mixed fluid (Fluid 2, lavender). Relative values for applied pressure are indicated with green (high), orange (mid), and gray (low) circles, and the closed circle on the waste bypass denotes the location of a plug.

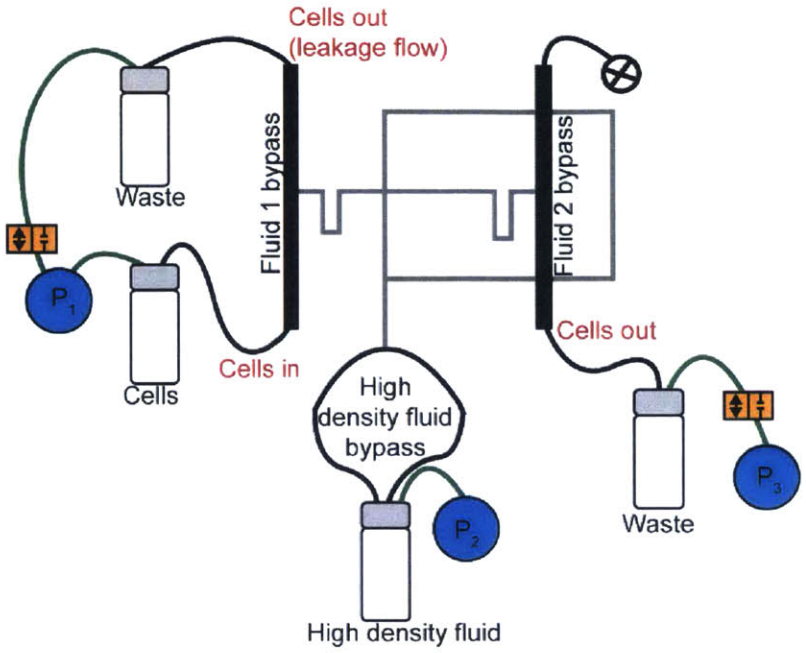

Figure 1.2-7. Diagram of fluidic and pressure components in the dual SMR. Solenoid valves (orange rectangles) set waste vial pressures to those of the pressure regulators (blue circles) or to atmosphere. A plug (circled black X) forces waste fluid into a single vial. Black lines indicate fluidic tubing, and green lines indicate pneumatic tubing.

Although the dual SMR design is amenable to increased throughput, several non-obvious challenges to precision measurements in a low Reynold's number (Re~0.8) environment were evident during testing of preliminary designs. Three critical design features address these challenges and facilitate the measurement: (1) differently-sized cantilevers to prevent signal cross-talk; (2) a microfluidic cross-junction to steadily introduce a second fluid; and (3) a narrow serpentine channel to facilitate mixing the two fluids.

The first design feature, differently-sized cantilevers, minimizes crosstalk of the signals measured from SMR_1 and SMR_2. Crosstalk results from mechanical coupling between the vibrations of similarly sized cantilevers with their out-of-phase neighbors. If the two cantilevers in the dual SMR have similar dimensions, their resonance frequencies are similar; thus, the mechanical vibrations of one will apply an auxiliary driving force on

its neighbor. Significantly altering the geometry of one cantilever (300 and 360μm length for SMR_1 and SMR_2, respectively) eliminates crosstalk by ensuring that the two resonance frequencies are different.

The dual SMR's second critical design feature is a microfluidic cross-junction that consistently introduces a second fluid of higher density. The addition of this high density fluid may occur by either a cross-junction or a T-junction (Figure 1.2-8). The time required for two fluids to mix across a channel is approximately four times smaller in a cross-junction design relative to a T-junction because mixing occurs at two interfaces rather than just one. What is not readily apparent is how differently the two configurations perform in the presence of cells. Variations in pressure occur as large-sized cells pass the microfluidic junctions and enter the high resistance serpentine channel. These pressure changes alter the relative amount of high density fluid introduced at the junction and create changes to fluid density along the serpentine channel, which adversely affect the SMR_2 baseline stability at the time of the large cell's measurement. However, baseline stability for cells already in the vicinity of SMR_2 is not adversely affected. The cross-junction design better dampens these effects due to its larger interface between the two fluid streams, as compared to the T-junction design (Figure 1.2-8). We selected the cross-junction design for all cell measurements. In this design, SMR_2 baseline changes in the vicinity of a cell measurement are typically ~1 x 10-5 g/mL, a value which corresponds to a <0.01% change in the ratio between the two fluids.

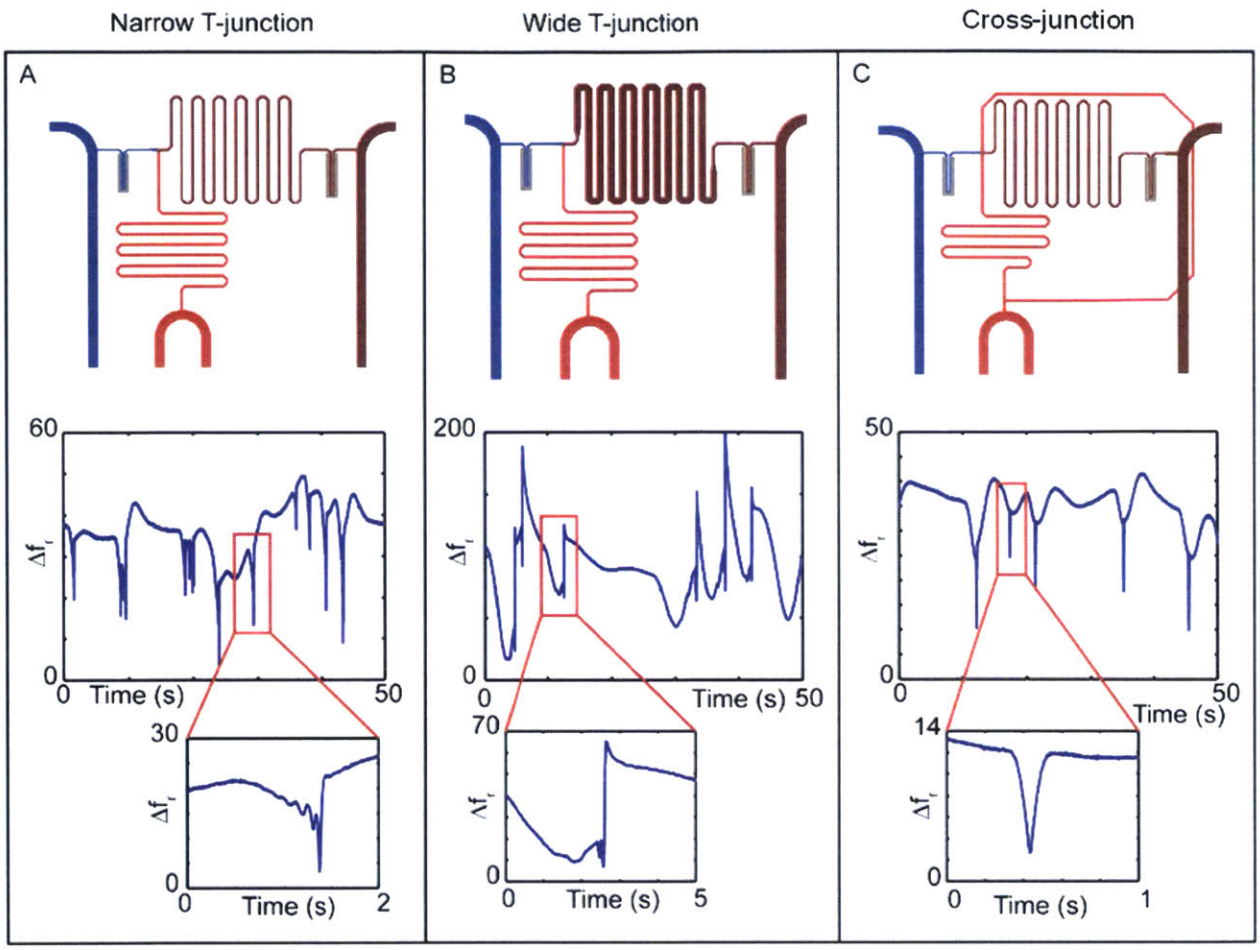

Figure 1.2-8. Comparison of different dual SMR channel designs.
The designs evaluated include the narrow T-junction (A), wide T-junction (B), and cross-junction (C). Schematics of the channel configurations are shown in the top row of the figure. Fifty seconds of acquired frequency data from SMR_2 are shown in the middle section. Insets are of peaks highlighted by red boxes in each frequency trace. The uniform peak shape and low baseline variation in the cross-junction design demonstrate its superiority over the narrow T-junction and wide T-junction.

To ensure that each cell is immersed in a near-homogeneous solution when measured in SMR_2, the dual SMR has a 5000 μm long serpentine channel, and flow rates are set such that the lag time for cells traveling from SMR_1 to SMR_2 is greater than ten seconds. In a 25 μm wide serpentine channel, the time required for the fluid mixture to reach 95% homogeneity is approximately six seconds, and in principle, the dual SMR enables cell mass, volume, and density measurements at a faster rate than the single SMR,

approximately two cells per second. Increased flow rate, higher data acquisition rate, a longer serpentine channel, and lower viscosity fluids would improve throughput without sacrifice to measurement resolution. Cell rupture and other negative effects on cell viability are not expected to occur at increased flow rate. In the same way that junction design affects baseline stability, serpentine channel geometry is also important; a wider serpentine channel introduces even greater baseline instability than a narrow channel. In the wide T-junction design (Figure 1.2-8), the baseline frequency instabilities are more than 10 times those observed in other designs. Thus, pressure damping features (Figure 1.2-8) at the point of fluid introduction and high downstream channel resistances are critical to achieving a stable system when particles are sized close to that of the channel. These features are included in the cross-junction design.

1.2.2.3 Comparison of the two methods

There are several challenges associated with operating the dual SMR, most of which relate to its sensitivity to changes in pressure and high channel resistances. The pressures at the start of an experiment must be carefully balanced to ensure proper direction and speed of fluid flow at all inlets and to maintain the desired composition of Fluid 2. During the course of the experiment, the fluid height in each of the vials gradually changes, and so the pressures must be monitored and adjusted periodically. Pressure adjustments are implemented by either changing the setting on an electronically controlled pressure regulator (resolution = 0.006 PSI) or by manually adjusting the vertical height of the fluid vials. These methods allow changes to fluid flow rates by ~0.02%. Large-sized cells introduce baseline instabilities, and bubbles and small pieces of debris also upset the pressure balance. Filtering all fluids and a lengthy flushing procedure (five to seven minutes) prior to the start of an experiment helps mitigate this problem, but debris still

occasionally disrupts the system. Because the channel volume of the dual SMR is so much greater than that of the single SMR, the likelihood of trapping debris or generating bubbles is much greater; similarly, isolating the source or location of each of these issues is more challenging in the dual SMR.

One practical consideration when operating the dual SMR relates to selecting a cell concentration that allows for a reasonably steady baseline. When a cell passes through the cross-junction into the serpentine channel, it causes a local fluctuation in the composition of Fluid 2. Thus, when many cells are measured in quick succession, the baseline becomes less steady, which increases the uncertainty in determining the fluid density. One approach to solving this problem is to increase the fraction of high density fluid delivered to the serpentine channel. This requires the high density fluid to be delivered with higher pressure, which makes pressure fluctuations from cells less significant. So as not to sacrifice measurement accuracy, the increased pressure also requires adjustments to slow the passage of cells, which slows fluid flow in the system overall and results in an overall steadier baseline. These adjustments, however, reduce the rate at which cells can be measured. Although in principle the dual SMR should be able to measure approximately two cells per second, the most reliable operation is achieved when cells enter SMR_1 at approximately one cell every ten seconds, which is comparable in throughput to the fluid-switching method for measuring density presented by Grover, et al (32). Thus, practical considerations associated with the existing design currently limit its overall performance.

The primary throughput limitation of the single cantilever, however, relates to its inability to measure cells serially. Thus, once a single cell enters the cantilever, no additional cell can be measured until the original cell is returned from the Fluid 2 bypass channel. During this process, a significant volume of cells is flushed by the Fluid 1 bypass

channel, resulting in some loss of sample, and limiting the usefulness of the technique in measuring rare cells. Nonetheless, refinements in the measurement technique have resulted in a throughput that exceeds that reported in Grover et al, 2011. Additionally, this method suffers far less from the baseline instabilities associated with the dual SMR, has fewer narrow channels and is thus less susceptible to clogging, and involves balancing the pressure among four, rather than six ports, ensuring a simpler and more reproducible measurement.

1.2.3 Approaches for minimizing measurement error

1.2.3.1 Effect of Fluid 2 density on density measurement error

Density variation measured in a cell population can result from natural biological heterogeneity and error in the measurement technique. One source of error in the measurement technique arises from the value of the density of Fluid 2 relative to the density of the measured cells. Though Fluid 1 is almost always cell media, the composition of Fluid 2 can be adjusted by adjusting the vial heights and peak wait times in the single cantilever method, or the pressure ratio between the channels meeting at the cross-junction in the dual cantilever method. The effect of the Fluid 2 density value on measurement error was estimated by applying multiplicative and additive errors to average L1210 cell buoyant masses in Fluid 1 and a range of Fluid 2 values, measured in the dual SMR.

Multiplicative error results from an uncertainty in determining the cell's exact lateral position in the tip of the cantilever channel (39). This error, estimated from the buoyant mass distribution of polystyrene beads (Figure 1.2-14), is inversely dependent on particle radius and directly proportional to buoyant mass. Thus, minimizing this error involves measuring either larger particles or adjusting the fluid density to reduce buoyant

mass. In the theoretical case of pure multiplicative error, uncertainty in determining the density of the cell will be at a minimum when the density of Fluid 2 matches that of the cell (Figure 1.2-9). Here the cell buoyant mass is zero, as is the associated error, and measuring Fluid 2 density is sufficient to determine the density of the cell. As the density of Fluid 2 deviates from that of the cell, the magnitude of the cell's buoyant mass in Fluid 2 will increase, as will the associated density measurement error. Interestingly, multiplicative error in the volume measurement continually decreases for higher Fluid 2 densities (Figure 1.2-9). This decrease is graphically indicated as a decreasing standard error in the slope (Figure 1.2-1) where the x-axis (fluid density) distance increases between the two buoyant mass measurements.

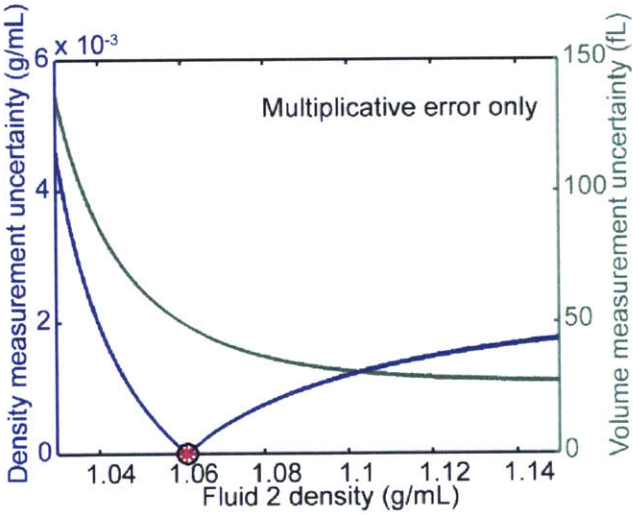

Figure 1.2-9. Measurement uncertainty as a function of Fluid 2 density in the case of purely multiplicative error.
The uncertainty of cell density is shown in blue, and the uncertainty of cell volume is shown in green. The actual cell density is indicated by a pink asterisk. The minimum uncertainty in the density measurement is indicated with a black circle. The uncertainty in volume decreases continuously with increasing Fluid 2 density.

A second form of error is a *additive error*, which results from a constant baseline noise and leads to uncertainty in determining peak height and thus cell buoyant mass (40). In the theoretical case of pure additive error, the minimum uncertainty in determining cell

density occurs when the density of Fluid 2 is greater than the density of the cell (Figure 1.2-10). Under the conditions of our simulation, the minimum value occurs when the fluid density is approximately 1.15 g/mL. Beyond this minimum, the uncertainty increases at a relatively slow rate. Similarly to the case of multiplicative error, uncertainty in the volume measurement due to additive error decreases as the difference between Fluid 1 and Fluid 2 increases (Figure 1.2-10).

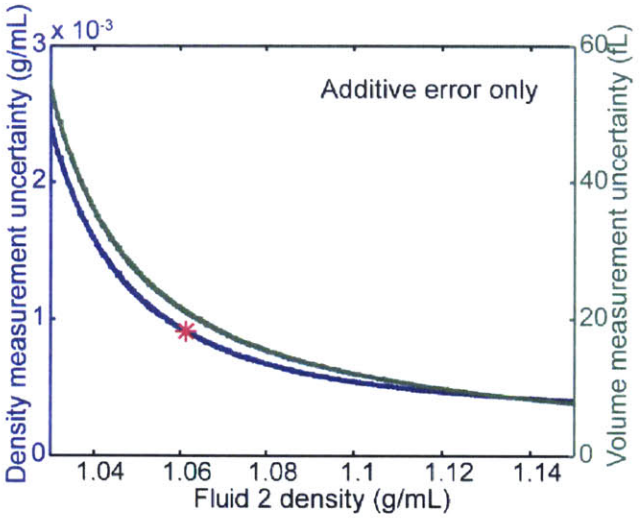

Figure 1.2-10. Measurement uncertainty of cell density or cell volume is a function of Fluid 2 density in the case of purely additive error.
The uncertainty of cell density is shown in blue, and the uncertainty of cell volume is shown in green. The actual cell density is indicated by a pink asterisk. The minimum uncertainty in the density measurement is not shown, and the uncertainty in volume decreases continuously with increasing Fluid 2 density.

When multiplicative and additive errors are both present, as is the case with the dual SMR, each dominates different measurement regimes. Multiplicative error dominates when buoyant mass is relatively large and additive error dominates when buoyant mass is relatively small. When both forms of error are present, the error in the cell density measurement is minimized where the Fluid 2 density is slightly greater than cell density (Figure 1.2-11). Here multiplicative error is small and additive error dominates, meaning density measurement error is mainly determined by noise in the instrument baseline.

When Fluid 2 density deviates from this minimum, multiplicative error dominates, and density measurement error increases. Volume measurement error decreases asymptotically as the difference between Fluid 1 and Fluid 2 increases. Thus, to optimize the measurement error for both density and volume, the Fluid 2 density should be somewhat greater than that of the cell.

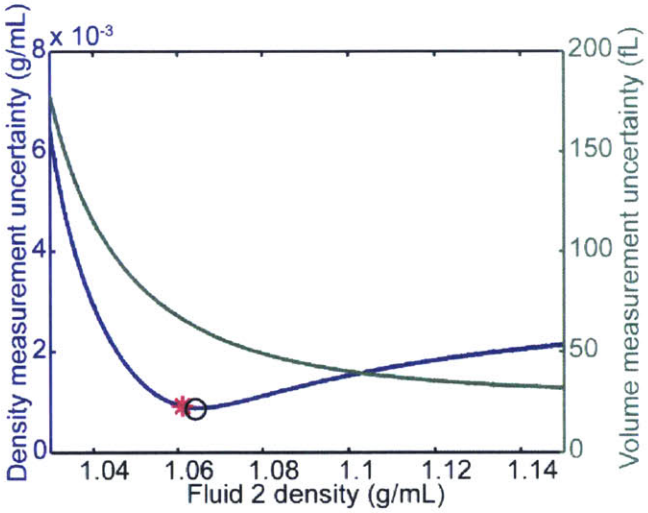

Figure 1.2-11. Measurement uncertainty of cell density and cell volume as a function of Fluid 2 density, assuming no uncertainty in measuring fluid density.
The uncertainty of cell density is shown in blue, and the uncertainty of cell volume is shown in green. The simulation is calculated using fixed values for buoyant mass in Fluid 1, L1210 cell density, and Fluid 1 density, along with a range of experimentally relevant values for Fluid 2 density, which correspond to a range of buoyant masses in Fluid 2. Multiplicative error is applied to the simulated measurements based on the variation in buoyant masses of polystyrene beads, and additive error is applied using the magnitude of the baseline noise in each cantilever. The Fluid 2 density of a typical experiment in the dual SMR is adjusted to approximately 1.07 g/mL^{-1}. The pink asterisk indicates the cell density, and the black circle corresponds to the point of minimum uncertainty in the density measurement. Uncertainty in volume decreases continuously with increasing Fluid 2 density.

The effect of the value for Fluid 2 density is especially pronounced when performing the dry density measurement discussed in §1.2.1.1. As discussed in the above section, minimizing measurement error requires that the Fluid 2 density be somewhat greater than that of the cell. However, the dry density of the cell is close to 1.4 g/mL, and the density of D_2O-PBS is approximately 1.1 g/mL. Thus, in this case, the Fluid 2 density is significantly

lower than that of the cell. To determine the effect of this difference on measurement error, a simulation was performed by calculating the cell density from a population of buoyant masses with a range of uncertainties comparable to the noise of the SMR used in conducting the measurements shown in this manuscript (0.05 – 1 Hz). The same level of uncertainty was added to both the buoyant mass in Fluid 1 and in Fluid 2. Only additive error was considered in this case. As shown in Figure 1.2-12, the effect of additive error on the density measurement (A, B) is much less pronounced than on the dry density measurement (C, D).

An important metric when considering this error is how the variance of the simulated population compares with that of an experimentally measured population. If the width of the simulated distribution is smaller than that of the experimental population, then the distribution of the population can be estimated to be dominated by biological variability rather than measurement error. To make this estimation, the experimental population was compared to the simulated distribution corresponding to 0.5 Hz measurement noise, as this was a value most closely representing the instrument noise during a typical experiment. As shown in Figure 1.2-12B, the width of the simulated population of the density measurement is much smaller than the experimental population; however, the width of the simulated dry density measurement distribution is fairly close to that of the experimental population (Figure 1.2-12D), suggesting that the true, biological variability in this parameter may be smaller than that obtained under the measurement conditions shown here. Because the maximum value for the Fluid 2 density is capped at the value for D_2O (~1.1 g/mL), other approaches to minimize error in the dry density measurement, likely involving improvements to the optical and electronic components of the system, must be utilized.

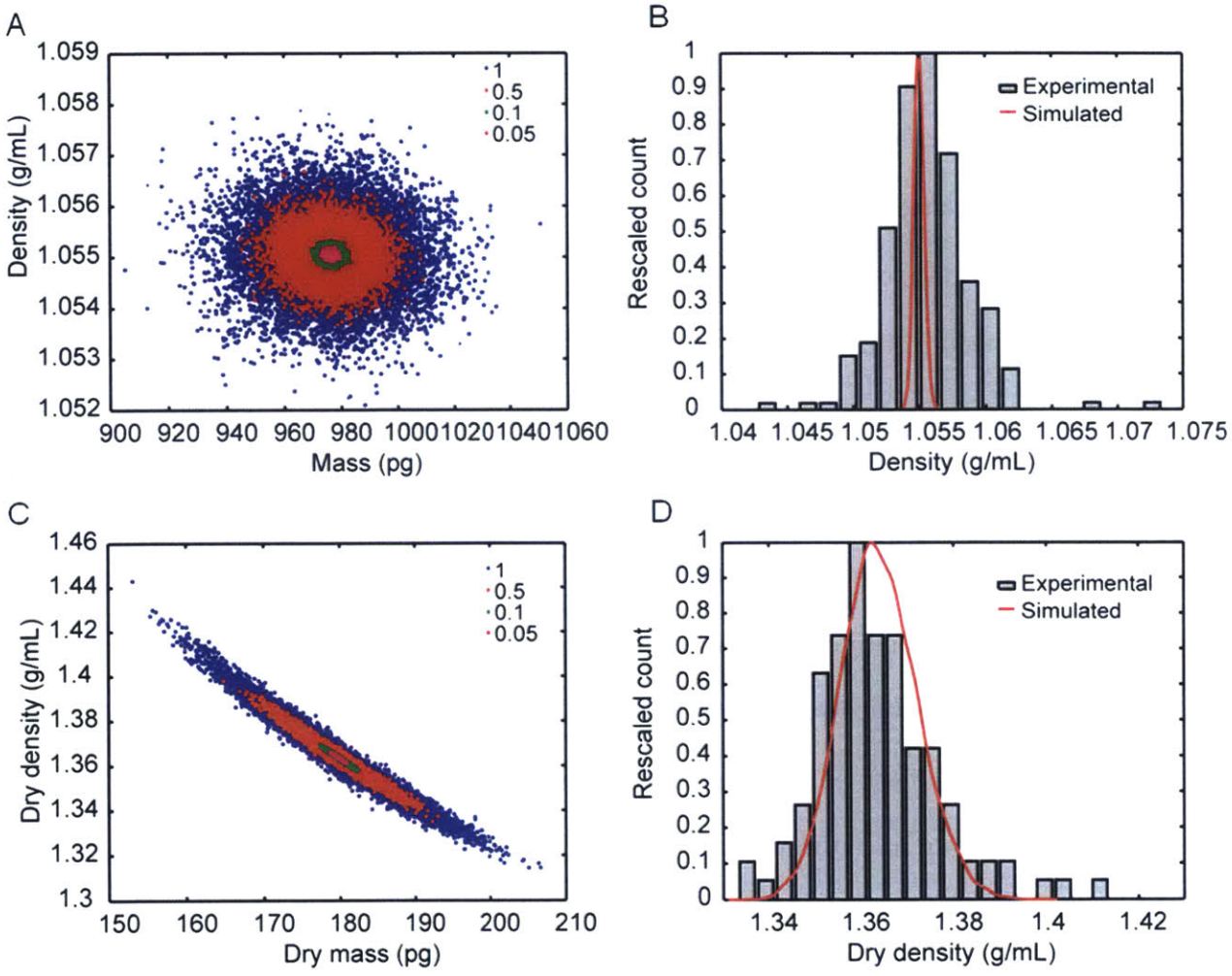

Figure 1.2-12. Comparing the effects of additive error when measuring total density and dry density.
Scatter plots (A and C) represent the effect of additive error applied to peak height measurements in Fluid 1 and Fluid 2 at values indicated in legend (0.05 – 1 Hz). Bar graphs (B and D) represent overlay of simulated density distribution with additive error of 0.5 Hz (red curve) over distribution of experimental data (gray bars).

1.2.3.2 Second mode actuation to reduce measurement error

Another means of reducing the error in the density measurement is to actuate the SMR in second mode (Figure 1.2-13) (28, 39). This type of actuation, typically requiring a higher amplitude driving force, is characterized by the introduction of a node midway along the cantilever, or a region that remains stationary while other regions in the cantilever are in motion. Thus, while a cantilever resonating in first mode has only one region of high

amplitude motion, and therefore high sensitivity, at the peak, a cantilever resonating in second mode has an additional region of high sensitivity at the antinode, situated between the fixed cantilever base and the node (Figure 1.2-13B, blue arrow). The multiplicative error discussed in §1.2.3.1 results from variation in the exact lateral position of a particle at the cantilever tip; a particle traveling on the outer wall of the fluidic channel of the cantilever will lead to a greater frequency shift than an identical particle traveling along the inner wall. However, frequency shifts measured at the antinodes are insensitive to the position of the particle in the fluidic channel, and are therefore free of multiplicative error (39). Thus, for data obtained with a second mode measurement, the antinode peaks are averaged to determine the buoyant mass, and the value of the middle peak is disregarded.

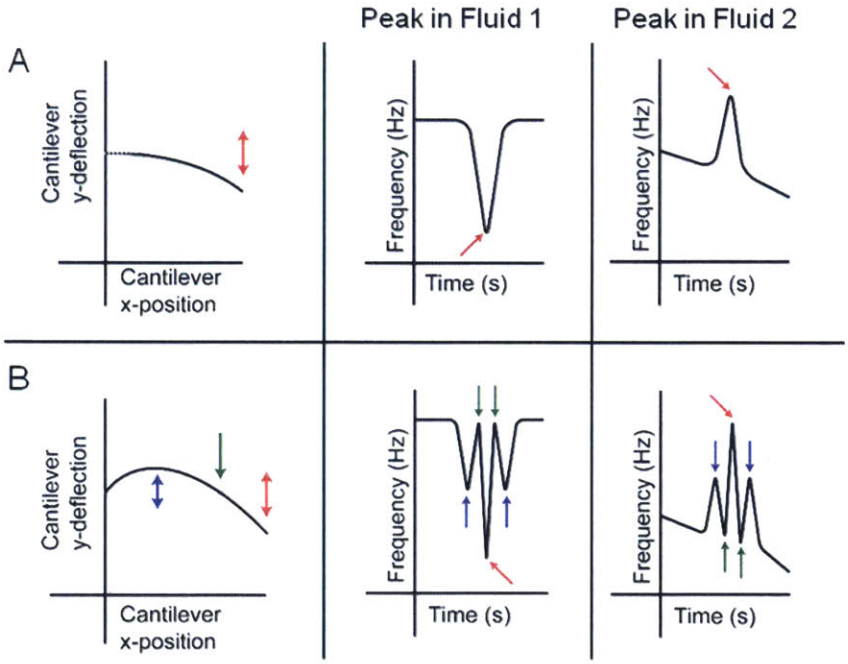

Figure 1.2-13. Cantilever mode shape and peak shape in first and second modes. First mode actuation is shown in the first row (A), and second mode actuation is shown in the second row (B). Double-headed arrows in the first column indicate the motion of the cantilever tip (red) or antinode (blue, bottom). The green arrow in the first column of (B) indicates the position of the node. Single-headed arrows in the middle and right-hand columns indicate peak locations corresponding to cantilever positions indicated by the arrows of matching color in the first column.

To illustrate the effect of position-dependent, or multiplicative, error, we can evaluate the measured variation of a population of polystyrene beads (Figure 1.2-14). The far left panel (orange) represents a histogram of 10 μm beads measured with first mode in SMR_1 of a dual SMR with a cross-section of 25 x 25 μm. The histogram displays a bimodal shape, likely representing an inner and outer path that the beads traveled through the cantilever. Indeed, the CV of this population is approximately 16%, more than ten times greater than that reported by the manufacturer. The same beads measured in SMR_2 of the same device demonstrate a narrower distribution (Figure 1.2-14, middle panel), with a CV of approximately 7%, in spite of the greater length of the cantilever leading to lower measurement sensitivity (§1.2.2.2). This is likely due to the cross-channel junction focusing the flow of the beads to a single streamline in the middle of the channel (Figure 1.2-6); flow focusing has been described previously as a means of reducing multiplicative measurement error (39). However, by minimizing the effect of multiplicative error, we can narrow the measured distribution even further. The histogram shown in the left-most panel in Figure 1.2-14 represents a distribution measured on a single SMR operating in second mode. The CV of this distribution is approximately 2%, or relatively close to that reported by the manufacturer.

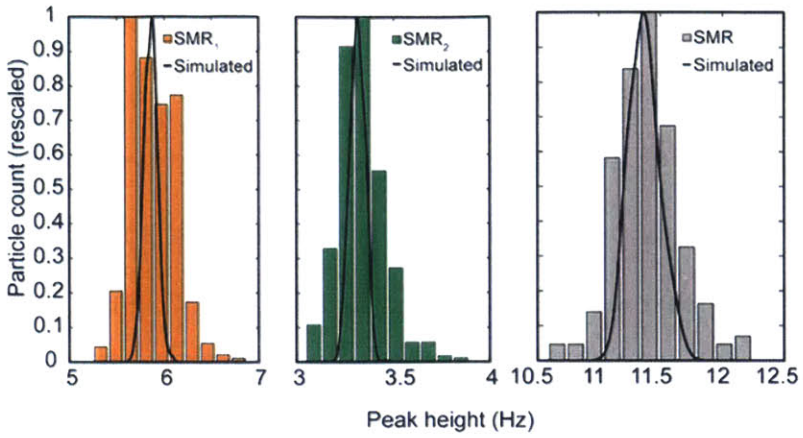

Figure 1.2-14. Comparison of distributions of 10 μm polystyrene beads measured in first mode with a dual SMR, and 8 μm polystyrene beads measured in second mode with a single SMR.
Measurements from the dual SMR are shown in the left-hand and middle panels, and measurements from the single SMR are shown in the right-hand panel. The histogram indicates the distribution as measured by the SMR, and the black line indicates the expected distribution based on manufacturer's reported value for CV of beads (1.2%).

1.3 Approximating the effects of changes to cellular composition on cell density

Because density is an aggregate parameter, we wished to develop a better intuition for the effects of changes to individual cellular components.[1] We therefore developed a model, using the equations described in §1.2.1.1, to calculate the effects of changing dry density, lipid content, or water content on total density. We made the following assumptions and approximations, based on previously reported values: (1) a dry density value of 1.4 g/mL (31); (2) lipid content of approximately 30% (41); and (3) a starting total density value of 1.057 g/mL (33).

[1] For clarity, in this section we will use the term "total" preceding mass, density and volume terms that refer to values that include both aqueous and non-aqueous material, and "dry" preceding mass, density and volume terms that describe non-aqueous material exclusively.

We first evaluated how changes to non-aqueous material could lead to a measurable change in total density, which we set at 0.005 g/mL, or approximately the range of a typical density measurement (§2.2 and §3.2). As shown in Figure 1.3-1A, a shift in dry density of approximately 0.05 g/mL, or equivalent to the typical range of dry density in mammalian cells, will lead to a measurable shift in total density (~0.0075 g/mL). We can anticipate this relationship based on a cellular water content of approximately 85%, calculated using the equations in §1.2.1.1. With all other parameters fixed, a change in dry density will lead to a change in total density which is nearly an order of magnitude smaller. Because our measurement of total density is approximately an order of magnitude more sensitive than our measurement of dry density (Figure 1.2-12), this outcome suggests that a change in total density could result exclusively from a change in biochemical composition.

However, what is not necessarily clear is how dry density, and therefore total density, will change when the absolute amount of an individual component changes. We therefore chose to next evaluate how a change in lipid content might affect density. Approximating the starting lipid mass to be approximately 30% of the total cell dry mass (41), we determined that a nearly 50% change in lipid mass would be needed to cause a measurable change in total density. Though this value depends on a substantial number of assumptions, we can nonetheless draw the general conclusion that our measurement of density may not be sufficiently sensitive to detect all changes in individual biochemical components.

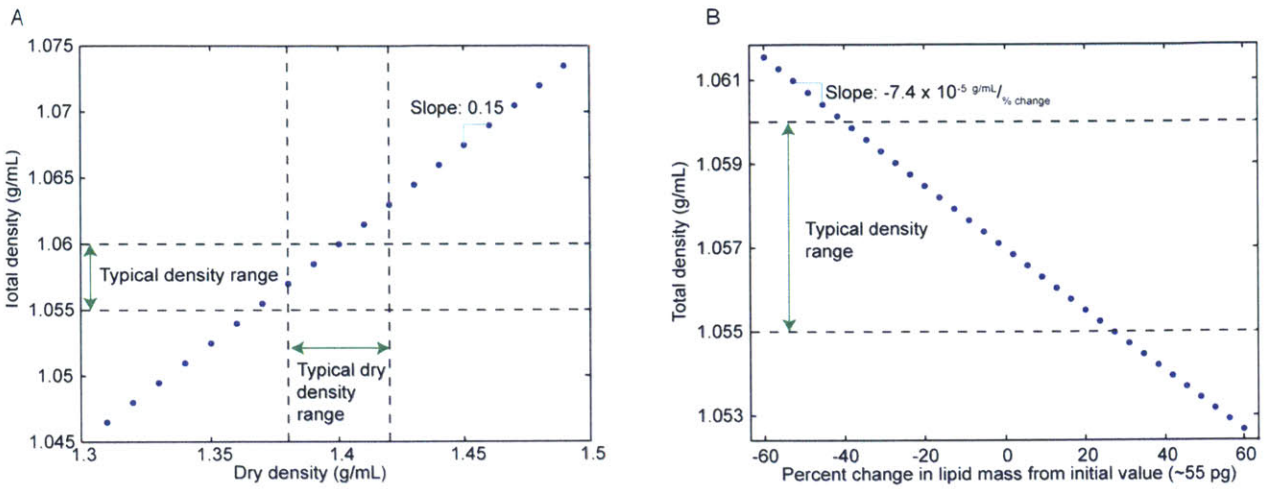

Figure 1.3-1. Relating changes to biochemical content to changes in density. Assuming constant water content (~85%), every 0.05 g/mL change in dry density leads to a 0.0075 g/mL change in total density (A). Assuming constant mass for all other components (~ 1100 pg), every 50% decrease in lipid content leads to a 0.0037 g/mL increase in total density (B). Values for water content in (A) and mass in (B) were determined by calculating the water content and total mass of a cell with a dry density of 1.4 g/mL and total density of 1.057 g/mL.

We next considered how changes to water content would affect total density. Because a cell is composed primarily of water, we expected the measurement of total density to be more sensitive to changes in water than to changes in lipid content. We evaluated both changes to the fractional water content of a cell (Figure 1.3-2A) and the absolute water content (Figure 1.3-2B). Our rationale for distinguishing between the two was that changes to fractional water content could be due to changes to either water content or dry content, whereas changes to total water content occur independently of changes to dry content. We determined that a relatively small change to the water fraction in the cell (~1%) could lead to a measurable change in total density, and a slightly larger (~2.5%), though still small, change to total water content would also lead to a measurable change in total density.

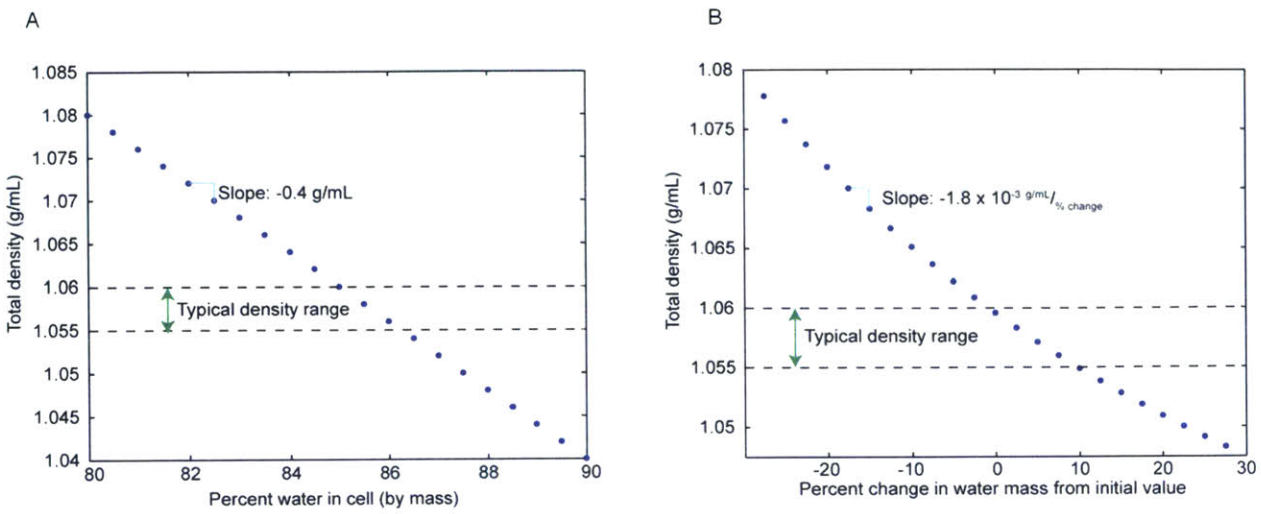

Figure 1.3-2. Relating changes in aqueous content to changes in total density. Assuming a constant dry density (~1.4 g/mL), every 1% increase in water content leads to a 0.004 g/mL decrease in total density (A). Assuming constant mass for all other components (~ 175 pg), every 2.5% decrease in water content leads to a 0.0045 g/mL increase in total density (B). Values for initial percent water content and water content by mass were calculated assuming a dry density of 1.4 g/mL and a total density of 1.057 g/mL.

This outcome also suggests that very small variance that we observe in the density measurement is due in part to tight regulation of the fraction of water in the cell—if the water fraction increases by approximately 0.5%, the density will change. Interestingly, this change would be undetectable when measuring mass or volume alone, as the variance in these parameters is approximately 50% (§2.2.1).

In the following sections, we will evaluate several case studies in which density serves as an indicator of specific physiological and environmental cues. We hope that the models described above will help provide some perspective regarding the possible sources for the changes to density that we observe.

Chapter 2

Characterizing cellular biophysical responses by relating density, deformability and size

2.1 Introduction

Cellular biophysical properties reflect aggregate effects of particular cellular activities, such as malignant transformation, differentiation, cell cycle progression, disease response, and apoptosis. Studying these properties can help provide insight into the underlying molecular mechanisms governing cellular behavior. For example, increased metastatic potential of cancer cells has been correlated with increased cell deformability (42–47). Studies on differentiation have also reported that the deformability decreases as stem cells become more differentiated (48, 49). Cell cycle stage is known to be associated with changes in cell shape and deformability (50, 51). Red blood cells (RBCs) affected by malaria show decreased deformability and density (32, 52). Finally, previous studies have reported that apoptosis is related to volume shrinkage and changes in cell deformability (10, 53).

Another common physiological source for changes to cellular biophysical properties is shifts in extracellular osmolarity. Certain tissues, such as the kidney, are regularly exposed to dramatic osmolarity shifts, and adjust their membrane surface area to allow for increases or decreases in cell volume to maintain a constant cortical tension (54). Articular cartilage in the synovial joints, such as the knee and hip, is subjected to both static and dynamic mechanical compression during articulation, resulting in changes in interstitial osmolarity of the cartilage tissue (55). This, in turn, can affect the biosynthesis rate, deformability, and volume of chondrocytes in the tissue (56–58). Moreover, the inability to respond to an osmotic challenge can result in impaired function, as is the case with T lymphocytes lacking the osmosensitive transcription factor NFAT5/TonEBP. Eliminating NFAT5/TonEBP expression prevents normal cell proliferation and development of adaptive immunity, likely due to an inability to adapt to the hyperosmolar conditions present in many lymphoid tissues (59).

Although most studies focus on the measurement of individual biophysical parameters, increasing evidence shows that combining information from measurements of multiple parameters can improve prediction of cell state. RBCs from patients with thalassemia, a genetic disorder which leads to a measurable but not significant decrease in RBC volume, can be distinguished from healthy RBCs based on a simultaneous comparison of both mass and density, but not from either parameter taken individually (32). The differentiation potential of stem cells can be accurately predicted by measuring the deformability of stem cells along with size, but not by measuring size alone (60, 61). Measuring deformability and diameter also enables prediction of four types of malignant diseases from a pleural effusion, whereas the identification based on a single parameter only provides an incomplete prediction (49). Measuring deformability and friction of cancer

cells reveals that reduced friction may play a role in further facilitating the passage of more deformable metastatic cancer cells through tight spaces (62).

Here we used a murine pro-B cell line as a model system and measured multiple biophysical parameters of individual cells with a suspended microchannel resonator (SMR). First, to fully understand how cells respond to osmotic stress, we measured volume, density, and passage time through a narrow constriction. Increasing the media osmolarity leads to increased density and decreased volume as expected. In contrast to density and volume, passage time is nearly independent of osmolarity even though deformability changes considerably, indicating that passage time should be measured together with cell volume. Finally, we compared relationships between deformability and density for cells treated with various pharmacological perturbations, including latrunculin B, staurosporine, cycloheximide, rapamycin, and Torin 1.

2.2 Results

2.2.1 Characterizing the density and volume of cells exposed to osmotic stress.

To characterize the biophysical effects of osmotic stress, we first measured the changes to density and volume of FL5.12 cells exposed to a range of osmolarities (Figure 2.2-1A). We varied the osmolarity of the cell media from 250 to 600 mOsm/L by diluting with dH_2O or concentrating with D-mannitol. Due to limitations described in Materials and methods (§2.4), we were not able to measure the density and volume at 600 mOsm/L, though we did obtain passage time measurements. Cell density increases following exposure to hyperosmotic media and decreases following exposure to hypoosmotic media

(Figure 2.2-1A and B); the effect of osmotic stress on cell volume follows an opposite trend (Figure 2.2-1C and D). We expect that the primary source of this trend is the change in cellular water content (63, 64). Water has a lower density than most non-aqueous cellular components, particularly proteins, nucleic acids, and certain lipid conjugates (65–67). Thus, when an osmotic challenge leads to a change in volume, the ratio of water to non-aqueous components will change as well. If the cellular water fraction increases, the density will decrease; this is the case with hypoosmotic swelling, in which the influx of water is associated with both a larger volume and a lower density. Similarly, the loss of water in the hyperosmotic case leads to both a decreased volume and an increased density. We estimated the change to water content using the method described in §1.2.1.1, and confirmed that hypoosmotic stress leads to an increase in water content, while hyperosmotic stress leads to a decrease in water content (Figure 2.2-1E).

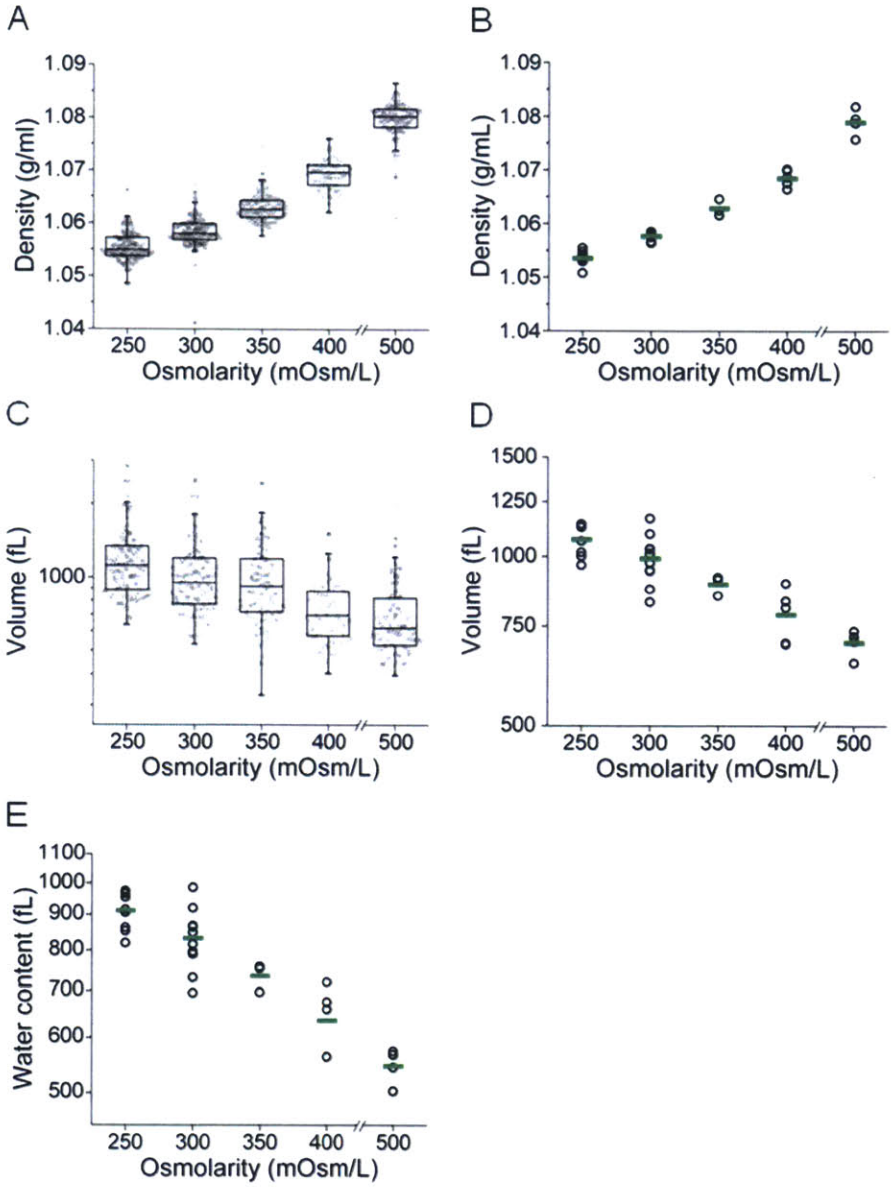

Figure 2.2-1. Effect of osmotic stress on density, volume, and water content.
FL5.12 cells are incubated in hypo- and hyperosmolar media for 30 min before and during the measurement. Box plots of density from a representative experiment (A). Each data point represents the density of an individual cell (n = 83-170). Density changes resulting from osmotic stress across multiple replicates (B). Box plots of volume from a representative experiment (C). Data shown was measured simultaneously with density in (A). Each data point represents the volume of an individual cell. Volume changes resulting from osmotic stress across multiple replicates (D). Changes in water content by volume resulting from osmotic stress across multiple replicates (E). In (B), (D), and (E), a single point represents the mean of one replicate and the green line indicates the mean from multiple replicates (3-8 times for each condition).

Interestingly, the variability in cell density appears to be much smaller than that of volume; we found this to be true both among a population of cells from single measurement (Figure 2.2-1A and C) and when comparing the means of multiple measurements (Figure 2.2-1B and D). For the 300 mOsm/L measurement shown in the box plots in Figure 2.2-1A and C, the interquartile range of density is approximately 0.005 g/mL, or approximately 0.5% of the mean, while the interquartile range of volume is approximately 500 fL, or approximately 25% of the mean. Similarly, the CV of density is approximately 0.3%, while that of volume is approximately 50%. We can attribute the wide volume range in part to differences in cell cycle stage in the population; the much narrower range of density could suggest that density remains relatively constant for a majority of the cell cycle.

The variability for multiple experiments is shown in Figure 2.2-1B and D, where each point represents the geometric mean of a single measurement, and the green bar represents the mean across multiple measurements. In this case, the CV of volume is approximately 10%, whereas that of density is 0.065%. This outcome further reinforces the notion of a biological mechanism to maintain a narrow density distribution. As a possible explanation, we can consider density to be a reflection of the crowding of intracellular macromolecular components; previous work has shown that the cytoplasm is extremely crowded, and that the level of crowding affects protein stability, adsorption to surfaces, and reaction rates (2, 4, 68). Thus, we can hypothesize that tight regulation of density results from a requirement to maintain a uniform level of crowding. An important consequence of the tight distribution of density relative to volume is that cells of similar densities will not always have the same volumes. Thus, simultaneous measurement of both density and volume is necessary to more accurately describe cell state.

2.2.2 Characterizing the passage time and deformability of cells exposed to osmotic stress.

Next, we determined how osmotic stress affects the passage of a cell through a narrow constriction by comparing the median passage times for osmotically-stressed cells to an isoosmotic control. In contrast to cell density and volume, the effect of an osmotic challenge on passage time is relatively small (Figure 2.2-2). Changes in passage time following osmotic challenges of 250, 350 and 400 mOsm/L are 0.68, 0.66, and 5.1%, respectively (Figure 2.2-2A and B). However, increasing the media osmolarity to 500 and 600 mOsm/L results in a ~ 30% increase in passage time. Similarly, following exposure to osmotic stress, cellular buoyant mass does not deviate significantly from its control (3.6, -0.79, and -3.6% changes, respectively, for 250, 350 and 400 mOsm/L, Figure 2.2-2C and D); exposure to 500 and 600 mOsm/L media results in a further decrease in buoyant mass (-9.2%, and -16% respectively), suggesting that buoyant mass decreases as osmolarity increases.

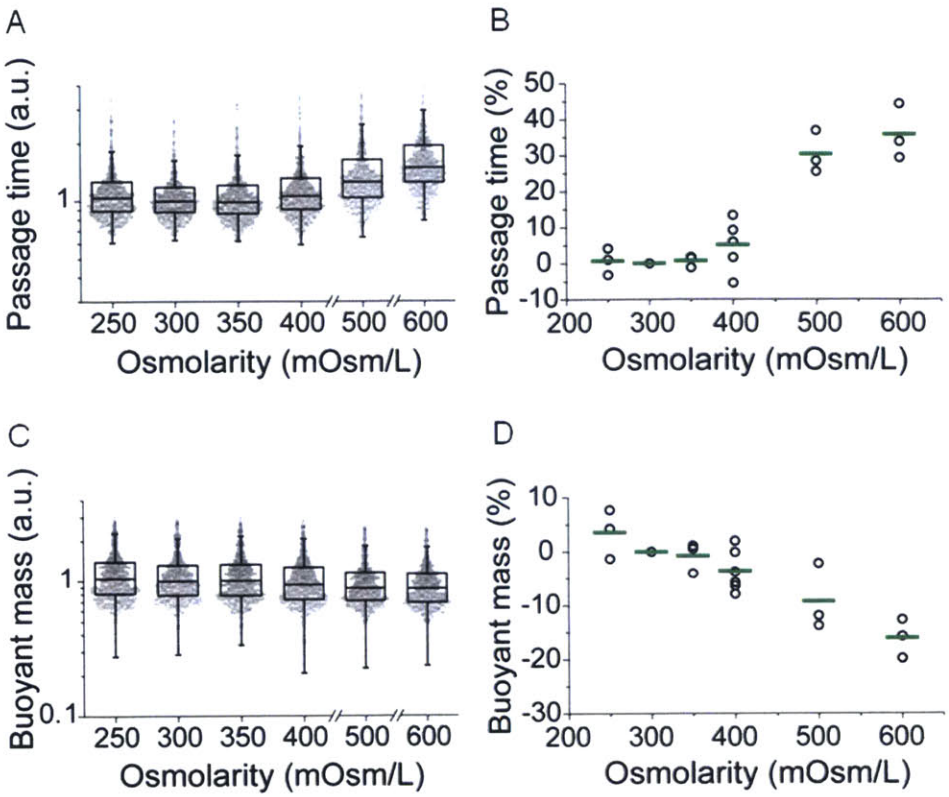

Figure 2.2-2. Effect of osmotic stress on passage time and buoyant mass.
FL5.12 cells are incubated in hypo- and hyperosmolar media for 30 min before and during the measurement. Passage time and buoyant mass are relatively unaffected by osmotic stress at 250, 350, and 400 mOsm/L. Box plots of passage time scaled by the median of the control (300 mOsm/L) (A). Each data point represents passage time of an individual cell (n = 972-1101). Percentage change in the median of passage time (B). The median passage time from each condition is normalized by the median of the control. A single point represents one repeat and the green line indicates the average from multiple repeats (3-6 times for each condition). Box plots of buoyant mass scaled by the median of the control (C). Data shown was measured simultaneously with passage time in A. Each data point represents the buoyant mass of an individual cell. Percentage change in the median buoyant mass (D). The median buoyant mass from each condition is normalized by the median of the control. A single point represents one repeat and the green line indicates the average from multiple repeats (3-6 times for each condition).

The relatively small changes to passage time and buoyant mass following osmotic stress between 250 and 400 mOsm/L can be attributed to simultaneous, compensatory changes in density and volume. For example, as a cell is compressed with an osmotic challenge, its density increases while its volume decreases. As a cell becomes denser by water loss, cell deformability decreases due to increased molecular crowding within

cytoplasm (64), which, in turn, increases the passage time (62). Therefore, though a denser cell should exhibit a longer passage time due to its decreased deformability, its smaller volume concurrently decreases the passage time (62, 69). As a result, the overall change in passage time caused by osmotic stress is relatively small. These results demonstrate that passage time reported independently of size may not always predict cell deformability, and that passage time must be compared for cells of similar size to decouple effects of varying size and deformability (62).

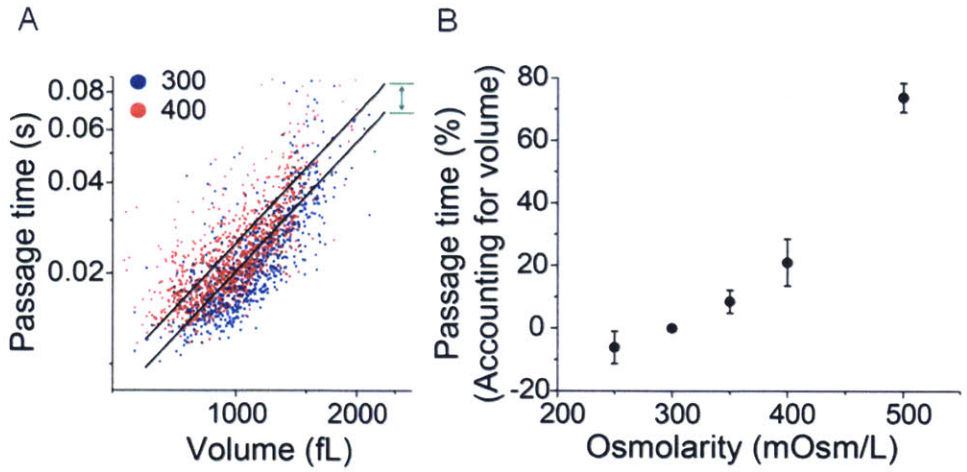

Figure 2.2-3. Determining deformability from passage time by accounting for cell volume. Volume is obtained by converting single cell buoyant mass data using the population average density. Passage time versus volume of the two datasets (from Fig. 3, isoosmotic and hyperosmotic conditions) in a log–log scale are fitted to the linear models (black lines) with a fixed slope and variable intercepts corresponding to the two conditions (A). The deformability is determined by the ratio of passage times given the same cell volume, which is acquired from the difference between the two intercepts (green arrow). Dependence of deformability (percentage change in passage time based on cell volume) on osmolarity of media (B). The data used is the same as shown in Figure 2.2-2.

Buoyant mass is a convenient size metric since it is simultaneously measured with passage time for individual cells (Figure 2.4-2, and §2.4.3). However, buoyant mass depends on cell volume and density, and, like passage time, is susceptible to compensatory changes in these parameters. Buoyant mass is defined as the product of the volume with the difference between the cell density and the density of the surrounding fluid; thus, the

increase in density following osmotic compression would lead to an increase in buoyant mass, while the decrease in volume would lead to a decrease in buoyant mass. Indeed, we find that the buoyant mass remains relatively unaffected by osmotic compression (350, 400 mOsm/L) (Figure 2.2-2C and D). Thus, we define deformability as the passage time of a cell accounting for its volume, thereby eliminating the dependence of passage time on size (Figure 2.2-3) (62). By using an average value for population density, which has a variance 100-fold smaller than that of both buoyant mass and volume, we can convert buoyant mass to volume with only minimal error contributions (Figure 2.2-1A and C, Figure 2.2-4) (32, 33). This is an improvement over previous methods, in which we performed the same conversion but starting instead with a volume distribution from a commercial Coulter counter (7, 62). A plot of each data set with a log-log scale is subsequently fit to lines with a fixed slope and variable intercepts (Figure 2.2-3A). The deformability is determined by the ratio of passage times given the same cell volume, which is acquired from the difference between the two intercepts (green arrow), and is then converted to a percentage (Figure 2.2-3B).

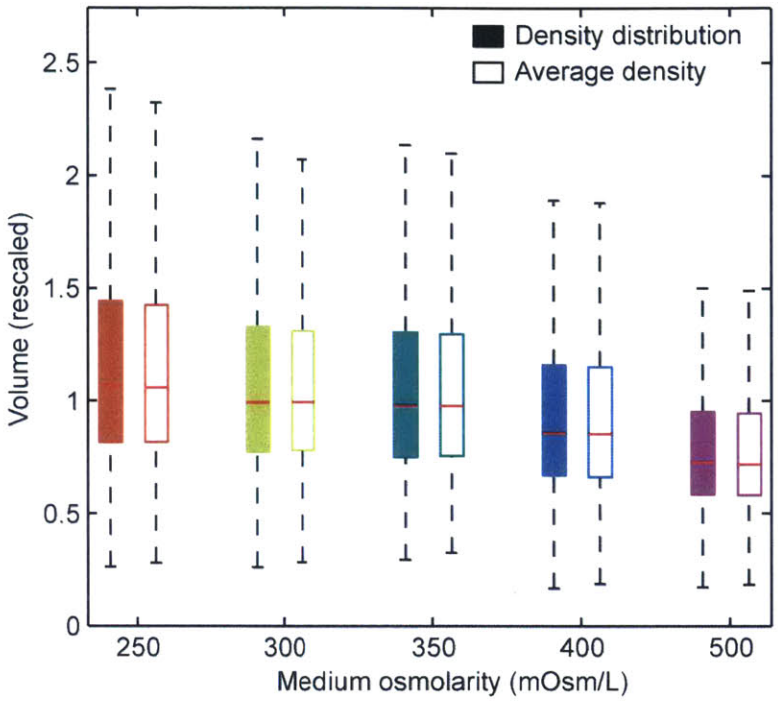

Figure 2.2-4. Estimating error associated with converting buoyant mass to volume using a density measurement.
Converting the buoyant mass from the constriction SMR to a volume using a density distribution (solid color) or average density (outline) value does not significantly increase the width of the subsequent volume distribution. A Monte Carlo simulation (n = 10000) was used to calculate a volume distribution (solid color) based on independent, random sampling of values from buoyant mass and density distributions. Red lines represent the median for each value, the top and bottom box boundaries represent the 75th and 25th percentile of the data, respectively, and the whiskers represent the most extreme data points not considered outliers. Representative data is from measurements at 250, 300, 350, 400, and 500 mOsm/L.

After accounting for volume, we can identify a significant difference between two cells of the same volume exposed to differing values of media osmolarity (-6.1, 8.5, and 21% changes, respectively, for 250, 350 and 400 mOsm/L, Figure 2.2-3B), which demonstrates that cells become stiffer by hyperosmotic compression and more deformable by hypoosmotic swelling. In other words, though the population of cells as a whole still exhibits a similar passage time to the isoosmotic control (Figure 2.2-2B), the viscoelasticity of an individual cell is changed by osmotic stress (Figure 2.2-3B). The observed decrease in deformability caused by hyperosmotic compression and determined by a longer passage time is consistent

with previous studies, one of which links the change to cytoplasmic crowding resulting from water loss (64, 70, 71). The increase in deformability by a hypoosmotic challenge has also been reported (58, 70, 72), but is not consistent among all studies (71), likely due to discrepancies in measurement techniques and cell lines. Our results indicate that volume should be taken into consideration when relating passage time through a constriction to cellular deformability.

2.2.3 Characterizing cell states by deformability, density, and volume

When cells are exposed to an osmotic challenge, changes in density or volume correlate with changes in deformability due to the dependence of all three parameters on the osmolarity of the surrounding fluid (Figure 2.2-1 and Figure 2.2-2). However, a general relationship between density, volume and deformability cannot be established *a priori*, since cellular activity or external stimuli can affect cellular composition and cytoskeletal proteins, which can affect density, volume and deformability independently of each other (32, 42). Similarly, a change in volume alone cannot predict density or deformability, except when cells change their volume only by water exchange. Thus, we next sought to investigate representative relationships of deformability versus density and volume (Figure 2.2-5), which would allow us to demonstrate how cell states can be characterized by multiple biophysical properties. In addition to an osmotic challenge, FL5.12 cells were also exposed to the following conditions: latrunculin B, staurosporine, cycloheximide (1 μg/ml, 10 μg/ml), rapamycin, and Torin 1. A summary of the effects of these drugs is provided in Table 2.2-1. Density, volume, and deformability were measured using the same methods as previously described. Passage time accounting for volume is then plotted versus density (Figure 2.2-5A) and volume (Figure 2.2-5B).

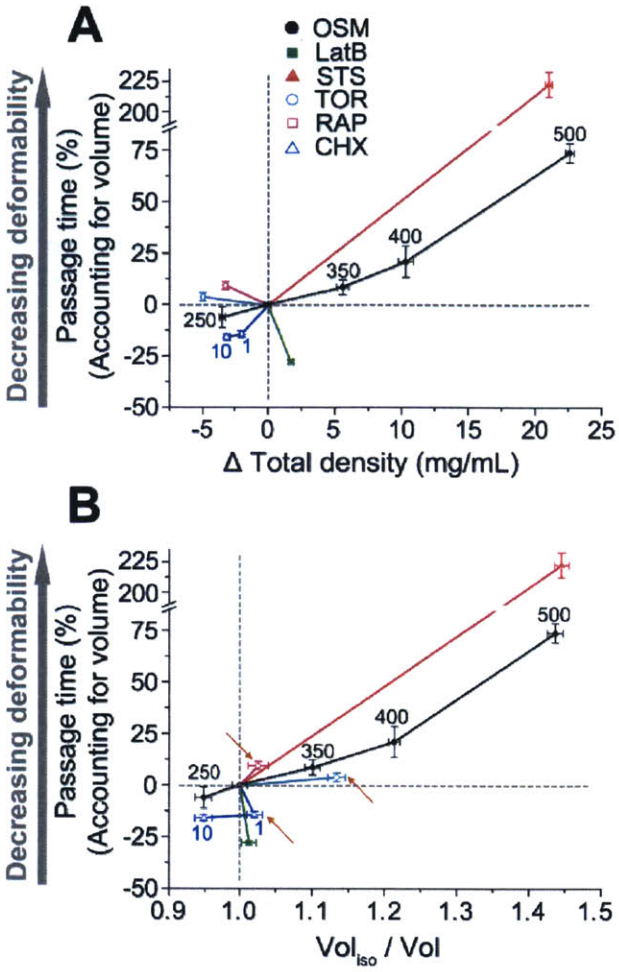

Figure 2.2-5. Deformability versus density and volume for various conditions. The conditions evaluated include: osmotic challenge (250, 350, 400, 500 mOsm/L), latrunculin B (LatB), staurosporine (STS), 1 μg/ml and 10 μg/ml cycloheximide (CHX), rapamycin (Rap), and Torin 1 (Tor). Changes in deformability, density, and volume after treatments are quantified based on the isoomotic control (untreated, 300 mOsm/L) in each experiment. Plots are divided into four quadrants, defined by two grey dotted lines. The percentage change in passage time accounting for volume is plotted versus the change in density. The correlation between changes in deformability and density depends on the mechanism associated with each treatment (A). The percentage change in passage time accounting for volume is plotted versus the change in volume. Rap, Tor, and CHX (1 μg/mL) are located in different quadrants compared to A (arrows) (B). Vertical error bars represent standard deviation of the mean. Horizontal error bars (density, volume) represent standard error of the mean. All treatments induce a significant change in the density ($p < 0.0001$, Wilcoxon rank sum). All treatments, except Torin 1 ($p = 0.0501$), induce a significant change in the passage time ($p < 0.0001$, linear model). The data used for the osmotic challenge is the same data as shown in Figure 2.2-1 and Figure 2.2-2. For the other conditions, we measured ~ 200 cells and ~ 1000 cells for density and deformability, respectively.

Table 2.2-1. Biological effects and mechanisms of drugs used in Figure 2.2-5.

Drug	Biological effects and mechanisms
Latrunculin B	*Inhibition of actin polymerization*: deformability decrease, apoptosis (73), cell cycle arrest (74), protein synthesis inhibition (75)
Staurosporine	*Inhibition of* protein *kinases*, apoptosis, deformability change (76), cell cycle arrest (77), protein synthesis inhibition (78)
Torin 1	*Inhibition of mTOR*: cell cycle arrest, modification of actin polymerization (79, 80), apoptosis (81) , protein synthesis inhibition (82)
Rapamycin	
Cycloheximide	*Inhibition of translocation*: protein synthesis inhibition, deformability change (83), apoptosis (84), cytoprotection (85), cell cycle arrest (86)

Increases in osmolarity lead to increases in density and decreases in volume and deformability, represented by the black solid lines in Figure 2.2-5A and B. Latrunculin B, however, leads to an increase in deformability accompanied by a slight increase in density and insignificant change in volume (green line, Figure 2.2-5A and B). A small increase in volume by latrunculin B has been previously reported (87). This outcome likely results from the relatively specific behavior of latrunculin B, which complexes with actin monomers to inhibit actin polymerization (88). These changes may result in a slight change in cellular water content, due to shifting hydration layers in the proteins; this shift may be sufficient to change density, but not volume (89).

Treating with staurosporine (red line) maintains the same relationship between density and deformability as we observe with osmotic stress but with a greater change in deformability. A cell undergoing apoptosis by staurosporine typically shows an apoptotic volume decrease and denser cytoplasm, which is consistent with our measurements of volume and density (90). Staurosporine can also lead to cell cycle arrest (77), inhibit protein

synthesis independently of caspase activation (91), and delocalize myosin II (92). Therefore, a decrease in deformability after treating with staurosporine may be related to impaired myosin activity, which may explain why staurosporine leads to a much greater change in deformability than does hyperosmotic compression.

Treating with 10 μg/ml cycloheximide decreases density similarly to what we observe under a hypoosmotic condition (250 mOsm/L), but with a greater increase in deformability. The increase in deformability caused by treating with cycloheximide, which inhibits protein synthesis, is consistent with a previous study (83). Interestingly, the biological effects of cycloheximide depend on the concentration and cell type. For example, while cycloheximide is cytotoxic at low concentrations to Jurkat cells, it has no effect on CEM C7 cells at low or high concentrations, even though both are human leukemic cell lines (84). Moreover, additional studies of different cell types exposed to low levels of cycloheximide have shown that it may have cytoprotective effects (85). This concentration dependence may explain the slight discrepancy between the changes to density and volume at 1 μg/mL and 10 μg/mL (Figure 2.2-5A and red arrows, B). Since cycloheximide can also induce the elongation or arrest of cell cycle, which may affect the protein content and cell volume (86, 93), the relationship between volume and density is difficult to predict. Thus, while density and volume are inversely correlated at the higher concentration, they are directly correlated at the lower concentration.

Similarly to the case with cycloheximide, we also notice that Torin 1 and rapamycin induce decreases in both density and volume, providing another example of how volume is not always inversely related to density (arrows in Figure 2.2-5 B). This outcome may be attributed to the biological effect of Torin 1 and rapamycin, which block mTOR, inducing cell cycle arrest at the G_1/S transition and inhibiting protein synthesis (94, 95). Previous

studies have shown that cell volume and deformability depend on the cell cycle (51). The slight decrease in population volume may thus be attributed to arrest in S phase. A decrease in density could be due to lower levels of both protein and DNA. In addition, Torin 1 and rapamycin are also known to affect actin polymerization and protein synthesis (79, 80, 82, 96). Although previous studies often demonstrated that Torin 1 and rapamycin can inhibit actin polymerization (80), rapamycin can also increase actin polymerization in RBL-2H3 cells (79), suggesting that the slight decrease in cell deformability by these mTOR inhibitors may be induced by the change in actin structure.

We would also like to note that the drugs used in our study typically cause a more significant change in deformability than does osmotic stress. For example, staurosporine induces more than a 200% change in passage time, and the deformability of FL5.12 cells is increased by cycloheximide regardless of changes in density or volume. This suggests that the integrity of cytoskeletal structure can play a more important role in deciding deformability than the changes driven by water exchange. However, Zhou *et al.* previously showed that latrunculin A-induced weakening of the cytoskeletal rigidity is overwhelmed by stiffening of the cytoplasm induced by very high osmotic stress (~ 1000 mOsm/L), suggesting that the change in cytoskeletal structure does not always dominate cell deformability (64).

2.3 Conclusions

We have shown the value of measuring multiple biophysical parameters. Although volume is the most commonly identifiable cell size metric, density can reveal additional information for understanding the mechanical properties of cells. Density may represent changes in structure or composition as well as the crowdedness in the cytoplasm which may

not be directly related to volume, but may still affect deformability. Grover *et al.* previously found that measuring density enables the identification of cell states which were not detectable by other cell size metrics, such as volume and mass (32). However, changes to deformability may not necessarily lead to changes in any size metric, particularly if the deformability change is associated with changes to structural proteins. Thus, by combining measurements of deformability and density, we can detect more specific biophysical characteristics that refine our representation of cell state.

2.4 Materials and methods

2.4.1 Cell culture and preparation

FL5.12 cells, a murine pro-B lymphoid cell line, were cultured as previously described (97). Briefly, cells were cultured in RPMI media (Invitrogen, Grand Island, NY) supplemented with 10% (v/v) FBS (Sigma-Aldrich, St. Louis, MO), 100 IU penicillin, 100 μg/mL streptomycin (Gemini, West Sacramento, CA) and 0.02 μg/mL IL-3 (R&D Systems, Minneapolis, MN) at 37°C. FL5.12 cells were exposed to an osmotic challenge or biochemical agent before each measurement. To maintain each condition during the experiment, the media used in the SMR were also supplemented with the same stimuli. For the osmotic challenge, cells were collected from the culture flask, centrifuged at 150 x g for 5 min, resuspended in hypertonic or hypotonic media, and incubated for 30 min before the measurements. D-mannitol (182.17 g/mol, Sigma-Aldrich) and deionized H_2O (dH_2O) were added to the media for the hyperosmotic and hypoosmotic conditions, respectively. For the isoosmotic control group (300 mOsm/L), cells were resuspended in the untreated culture medium. For chemical perturbations, cells were resuspended and incubated in the media

supplemented with 5 μg/mL latrunculin B for 30 min (Sigma-Aldrich), 2 μM staurosporine for 2 h (Enzo Life Sciences, Farmingdale, NY), 1 μg/ml or 10 μg/ml cycloheximide for 3 h (Sigma-Aldrich), 100 nM rapamycin (Santa Cruz Biotechnology, Dallas TX) for 24 h, or 250 nM Torin 1 for 24 h (generously provided by Prof. David M. Sabatini, Massachusetts Institute of Technology). Control groups for these conditions were cells resuspended in the culture media supplemented with DMSO as the vehicle. The SMR measurement data from the start of the measurement was compared to the data at the end of the measurement to ensure that the data showed no time dependence.

2.4.2 Experimental systems

SMRs were fabricated at Innovative Micro Technology (Santa Barbara, CA). Overall instrumentation for measurement and data acquisition have been previously reported in detail (25). Schematics of experimental approaches are shown in Figure 1.2-1, Figure 1.2-3, Figure 1.2-4, and Figure 2.4-2A. Density and volume were measured by a separate SMR system from that measuring passage time. The details of the density measurement are described in §1.2.1. An example of the results from a density measurement is shown in Figure 2.4-1.

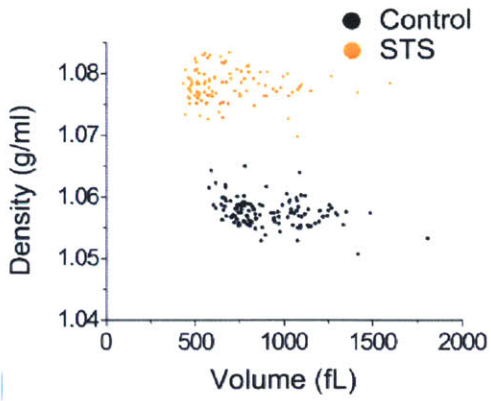

Figure 2.4-1. Cell density versus volume of FL5.12 cells treated with STS.
Treatment with STS leads to an increase in density and a slight decrease in volume.

To measure passage time, single cells were measured in an SMR with a constriction as previously described (62, 98) (Figure 2.4-2). Briefly, a cell is flowed into the embedded microfluidic channel of the SMR, and deformed as it flows into the constriction. The geometry of the constriction is a rectangular channel 6 μm wide, 15 μm deep, and 50 μm long. The cross-sectional area of the constriction is 90 μm^2 (6 μm wide × 15 μm deep) and the average diameter of FL5.12 cells is approximately 12 μm (untreated control), indicating a maximum cross-sectional area of approximately 113 μm^2. The narrow width of the constriction ensures the deformation of a cell as it squeezes into the constriction's entrance (entry) and then passes through the constriction channel (transit). The resonant frequency response of the SMR, which depends on cell's buoyant mass and position in the microfluidic channel, is tracked in real time as the cell passes through the channel. The passage time includes the total time required for the cell to slow down as it deforms to enter the constriction (entry time), and speed up as it travels through and exits the constriction (transit time). Here we measured the passage time as a metric for cell deformability, which is defined as the total time required for the cell to deform into and then transit through the constriction. The relative contribution of surface friction to the passage time can be

estimated by comparing the cell's velocities during the entry (entry velocity) and the transit (transit velocity). Typically, the passage time is dominated by the entry time since the transit velocity is significantly faster than the entry velocity (62). Dominance of the entry time in the passage time was consistently observed in our previous study, in which we measured seven adherent cell lines, including mouse embryonic fibroblasts, mouse lung cancer cell lines, human lung cancer cell lines, as well as a mouse lymphoblastic leukemia cell line that was grown in suspension (62). We have also measured cells in various conditions, such as treating cells with latrunculin B, and nocodazole, or coating the microchannel surface with positively charged poly-L-lysine. In all of these cell lines and treatments, the passage time was dominated by the entry time (62). Therefore, here we assume that the friction can affect but does not dominate the differences in passage times. The fluidic channel is coated with poly(ethylene glycol) [1 mg/mL; PLL(20)-g[3.5]-PEG(2); Surface Technology] to reduce non-specific adhesion of cells to the walls of the constriction. All measurements were acquired at room temperature under a constant applied pressure drop across the microchannel (0.15 psi) established by pressure regulators.

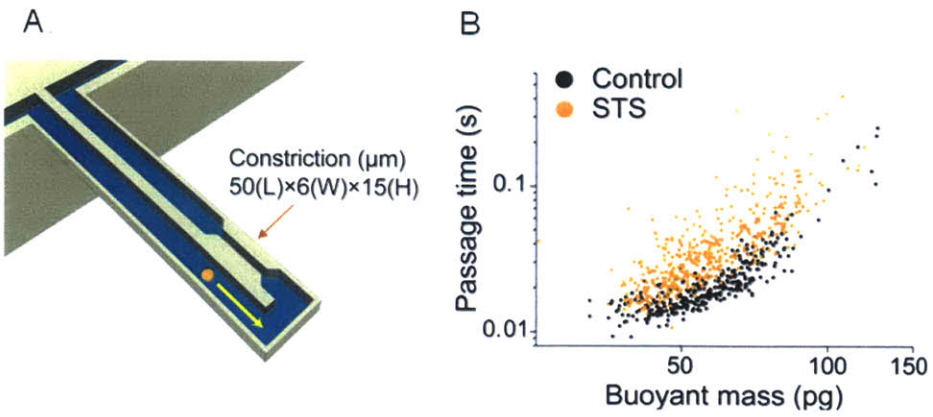

Figure 2.4-2. Schematic diagrams of the approaches that measure deformability and examples of the data extracted from the measurement.
An SMR with a constriction measures the passage time and buoyant mass as a cell flows into an embedded microfluidic channel and transits through the constriction (A). Passage time versus buoyant mass for the FL5.12 cell line shows the change in passage time induced by staurosporine (B) (STS).

2.4.3 Data analysis

SMR frequency data was converted to buoyant mass, passage time, volume and density using methods previously described (32, 62). In our manuscript, the term "volume" refers to the cell size represented by a volumetric unit. The "size" is a more general term which is used to refer to multiple parameters, including diameter or buoyant mass. Data plotted in Figure 2.2-1C and E, and Figure 2.2-2A and C represent volume, water content, passage time, and buoyant mass, respectively. These parameters are plotted with a logarithmic scale, which we considered to be the form that most accurately represents the data. Cell size follows a log-normal distribution, as has been previously reported (99). Passage time is expected to follow a log-normal distribution as well, since passage time has a strong power-law dependence on buoyant mass, as shown in Figure 2.4-2 (62, 69).

As previously presented, the SMR can be used to measure biophysical properties with high precision (25, 32, 62). The buoyant mass and the position of the center of mass of a particle passing through a constriction in the SMR can be measured with a precision near

1 pg and sub-micron, respectively (62). Additionally, the density and volume can be measured with a resolution of 0.001 g/ml and 3 fL, respectively (32). We can therefore attribute the variability observed in our measurement to inherent biological variations rather than experimental artifacts. For example, one source of biological variation in size is related to a distribution of cells across the cell cycle. Interestingly, in our measurements, cells of similar buoyant mass showed a significant variation in passage time (Figure 2.4-2), suggesting that, in addition to biological variation such as a cell cycle (51), the orientation of the cell upon entry into the constriction can cause a wide distribution (62, 100).

The buoyant mass obtained during passage time measurements was converted to volume using the following equation,

$$V = \frac{b_m}{\rho_{cell} - \rho_{fluid}} \qquad \textbf{2.4-1}$$

where V is the cell volume, b_m is the cell buoyant mass, ρ_{cell} is the average of the cell density obtained from a corresponding SMR density measurement, and ρ_{fluid} is the fluid density. The uncertainty contributed to the volume distribution resulting from converting the buoyant mass using an average cell density was determined to be not significant based on a Monte Carlo estimate (Figure 2.2-4).

Statistical significance between density measurements was determined using a non-parametric rank-sum analysis (Wilcoxon rank sum) implemented in MATLAB. Changes in passage time were estimated and the statistical significance of those changes were tested by fitting data sets to a linear model in R. For all statistical tests, a p-value less than or equal to 0.05 was considered significant. In particular, since most statistical tests showed very small p-values (10^{-50} - 10^{-5}), we indicated those small p-values by "$p < 0.0001$".

Chapter 3

Biophysical changes reduce energetic demand in growth factor deprived lymphocytes

3.1 Introduction

Cytokines and growth factors precisely control the dynamics of lymphocyte behavior during an immune response. Upon initial antigen exposure, pro-stimulatory cytokines, such as IL-2, mediate lymphocyte activation by promoting nutrient uptake and metabolism to support cell growth and proliferation (101–103). When an infection is cleared, levels of IL-2 and other growth factors decrease, leading to decreased nutrient uptake, cell cycle arrest, atrophy and apoptosis of most activated lymphocytes. A small surviving fraction of these cells differentiates into memory cells, also through a cytokine-mediated process (104, 105).

The absence of pro-inflammatory cytokine signaling limits nutrient uptake in memory cells (106, 107), though a number of mechanisms have been identified for maintaining viability under these conditions. First, memory cells undergo a significant metabolic shift; while activated cells consume large amounts of glucose to support

proliferation, memory cells limit metabolic expenditures almost exclusively to maintenance functions. Correspondingly, memory lymphocytes rely on oxidative phosphorylation to extract the maximum amount of energy from available nutrients (108, 109). Autophagy, or self-digestion of intracellular components, also plays an essential role in memory lymphocyte survival in the absence of IL-2 by providing an alternative source of metabolic precursors (110). Finally, the anti-apoptotic protein Bcl-2 is upregulated in memory lymphocytes relative to effector lymphocytes, helping to promote memory cell differentiation and survival (111–113). Bcl-2 also aids in the bioenergetic adaptation to decreased nutrient uptake, and remains elevated in memory cells for an extended period of time after an infection has been cleared (112, 113).

Memory differentiation of effector lymphocytes also involves a decrease in cell size, a response previously attributed to autophagy (114–116). Biophysical properties, such as cell mass, volume, and density, represent aggregate changes in cellular composition, and measuring changes in these properties can reveal adaptations that may be obscured when investigating individual molecular events or pathways in isolation (22, 23, 31, 32, 62). Here, we analyze cell size, described in terms of volume, as well as cell density, or mass per volume, of single lymphocytes, to better understand the effects of pro-growth factor withdrawal. While cell volume and mass are measures of combined cell water and biochemical content, density represents the contribution of each to overall cellular composition. Cell density is very tightly regulated, and can therefore reveal changes to cell state beyond those suggested by changes in cell volume alone (22, 23, 32, 33).

To study the response of lymphocytes to growth factor withdrawal, we examined FL5.12 cells, murine pro-B lymphocytes that depend on IL-3 for nutrient uptake and growth. In the absence of IL-3, these cells lose the ability to take up nutrients and consequently undergo atrophy and apoptosis. However, when the pro-survival Bcl-2 related

protein, Bcl-x_L, is expressed, or pro-apoptotic proteins are lost, apoptosis is inhibited and cells rely on autophagy for long term survival (114, 117, 118). Here, we show that changes to cell volume and density occur as an acute response to growth factor depletion, and that this response aids adaptation to decreased nutrient uptake prior to autophagy induction in both FL5.12 cells and primary monoclonal CD8+ cells.

3.2 Results

3.2.1 IL-3 depletion results in both atrophy and density changes in FL5.12 cells

We used a Suspended Microchannel Resonator (SMR) to measure changes to the volume and density of FL5.12 cells following depletion of IL-3 for up to 120 h. The SMR is a microfluidic cantilever-based mass sensor used to determine the mass of a single cell in a fluid—the buoyant mass—based on changes in resonance frequency (25). By measuring the buoyant mass of the same cell in two fluids of two different densities, we can calculate the total volume and density of that cell (§1.2.1) (32). Following IL-3 depletion, we found that cell volume decreases continuously for the entire measurement period, though most dramatically over the first 24 h (Figure 3.2-1A). Similar findings are observed when cell volume is assessed using a Coulter counter (Figure 3.2-1B), and are in agreement with previous studies (114, 119).

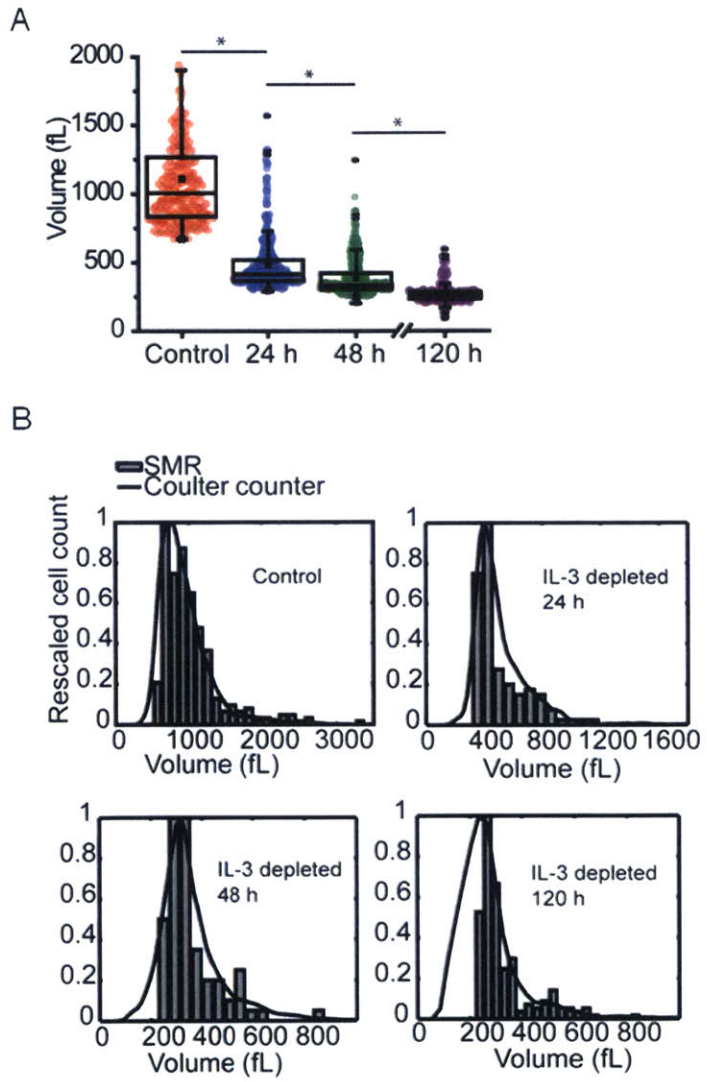

Figure 3.2-1. IL-3 depletion leads to a decrease in volume in FL5.12 cells over a 120 h period.
SMR measurements are shown in (A), and confirmed with a Coulter counter (B). Asterisks in (A) represent $p < 2 \times 10^{-26}$.

The density of growth factor-depleted cells increases continuously over the same time period (Figure 3.2-2). Cell density is the ratio of cell mass to volume, and also represents a weighted average of the densities of all cellular components. Thus, an increase in cell density is likely characterized by an increase in the amount of high density material, such as nucleic acids and proteins, relative to low density material, such as water; nonetheless, the decrease in cell volume indicates the potential for loss of both aqueous and

non-aqueous material. To determine the degree of loss of non-aqueous material, we used an SMR to measure the dry mass (31, 120) of FL5.12 cells depleted of IL-3 for up to 120 h. We observed a decrease in cell dry mass that occurs simultaneously with the changes to volume and density, suggesting that cells also lose macromolecular material (Figure 3.2-2B). These findings indicate that not all cellular material is lost in equal amounts, and suggests that the initial response to growth factor withdrawal is a large decrease in cell size with selective conservation of high density material.

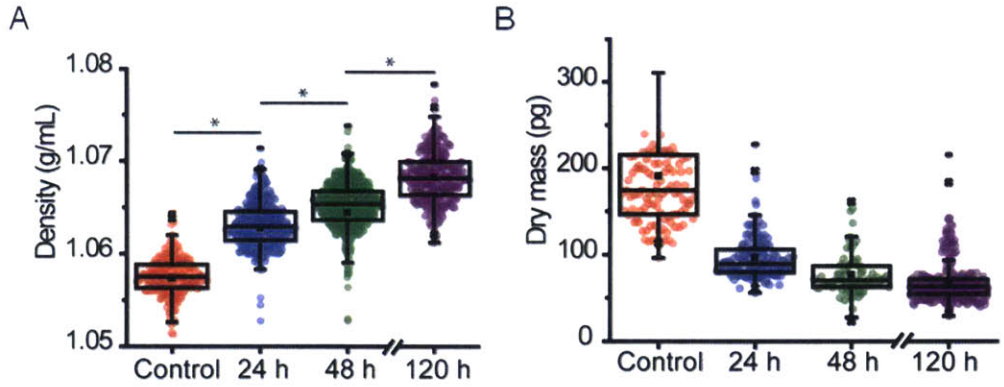

Figure 3.2-2. IL-3 depletion leads to a decrease in density and dry mass in FL5.12 cells over a 120 h period.
Density is shown in (A), and dry mass is shown in (B). Single asterisks in (A) indicate $p < 2 \times 10^{-26}$. Single asterisk in (B) represents $p < 8.9 \times 10^{-5}$, double asterisk represents $p < 7.1 \times 10^{-10}$, and triple asterisk represents $p < 3.6 \times 10^{-36}$.

To further analyze the intracellular content of the IL-3 depleted FL5.12 cells, we used high throughput cell phenotying (htCP), a single-cell resolution microscopy-based assay to quantitatively determine morphometric parameters of immuno-stained cells and fluorescence intensity of antibody-specific intracellular components (121). F-actin, mitochondria, and nuclei were stained and analyzed using htCP before and after IL-3 depletion. As shown in Figure 3.2-3, though both nuclear area and cellular area decrease five days following IL-3 depletion, the nuclear to cytoplasmic ratio increases, indicating a greater relative loss of cytoplasmic volume. Moreover, mitochondrial content only

decreases slightly, further suggesting that material contained in the nucleus and mitochondria is preferentially retained.

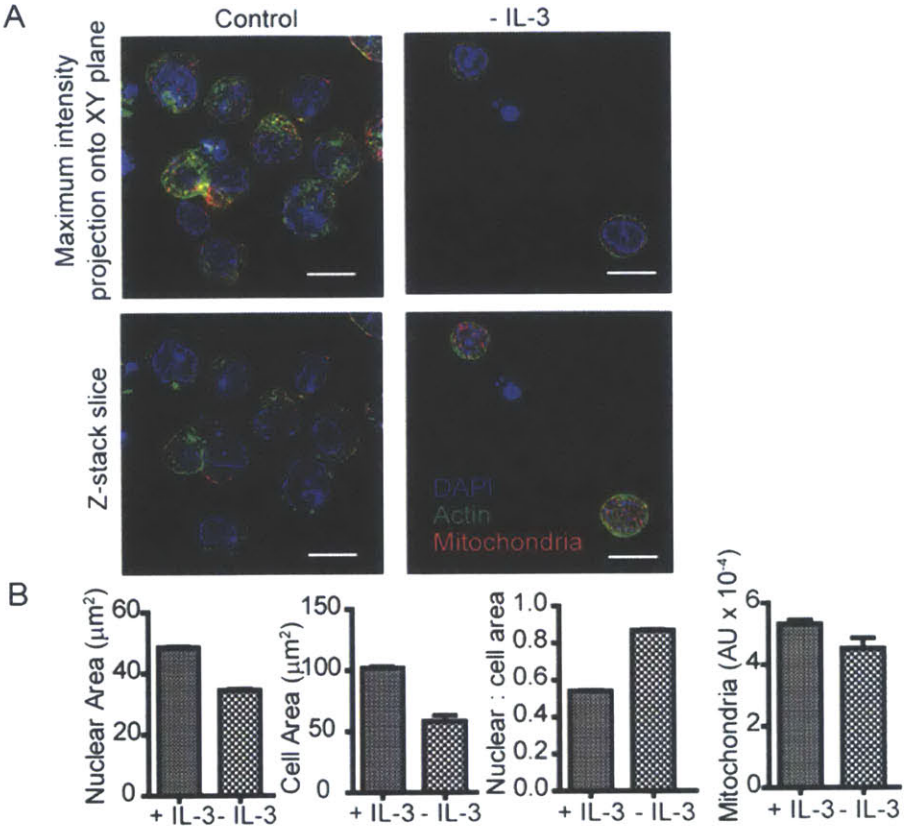

Figure 3.2-3. High throughput cell phenotyping (htCP) performed on control cells and 120 h following IL-3 depletion.
Representative images are shown in (scale bar: 10 μm) (A), and aggregate data are shown in (B).

To determine whether the increase in cell density was reversible, we added IL-3 back to a population of cells depleted of IL-3 for 120 h and measured changes in cell density, volume, and proliferation rate over a period of 96 h, which was the amount of time required for cells to return to previous rates of proliferation (Table 3.2-1). We found that prior to resuming proliferation, cells first decreased their density to approximately the value observed in proliferating cells (Figure 3.2-4B). The increase in cell density was followed by increases in both cell volume and proliferation rates (Figure 3.2-4A and Table

3.2-1), suggesting that a limited range of cell densities is compatible with cell proliferation. These data also suggest the increase in density following IL-3 depletion may be an adaptive response to conditions that are not conducive to proliferation.

Table 3.2-1. Doubling time of FL5.12 cells following IL-3 depletion and repletion.

Condition	Time elapsed (h)	Doubling time (h)
- IL3	0	11
	24	17
	48	> 24
	72	> 24
	96	> 24
	120	> 24
+ IL3	24	> 24
	48	> 24
	72	> 24
	96	11

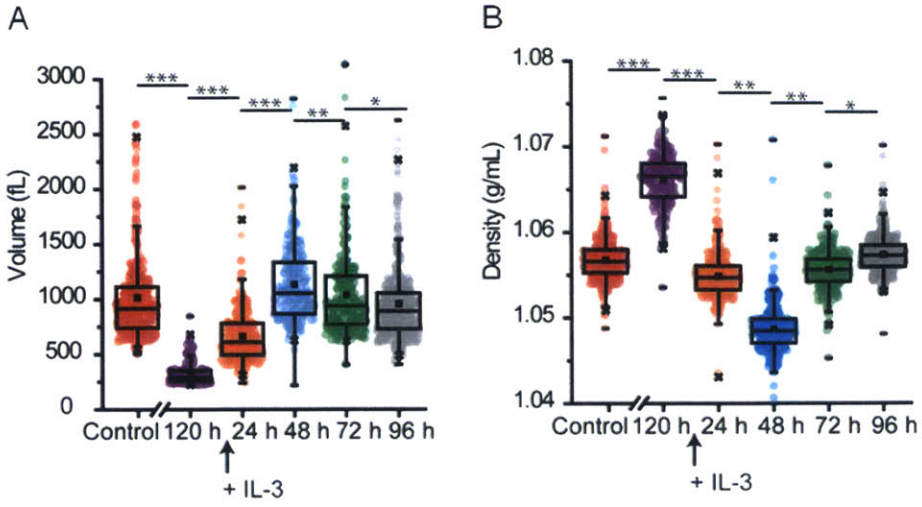

Figure 3.2-4. Biophysical changes to FL5.12 cells upon IL-3 repletion (black arrow) following 120 h of IL-3 depletion.
FL5.12 cell volume is shown in (A) and density is shown in (B). In (A), single asterisk indicates $p < 2 \times 10^{-3}$, double asterisk indicates $p < 1 \times 10^{-4}$, and triple asterisk indicates $p < 7 \times 10^{-53}$. In (B), single asterisk indicates $p < 1.1 \times 10^{-19}$, double asterisk indicates $p < 5.5 \times 10^{-62}$, and triple asterisk indicates $p < 8.2 \times 10^{-73}$.

3.2.2 Autophagy and IL-3 depletion lead to different biophysical changes

Induction of autophagy is a response that allows Bcl-x_L-expressing FL5.12 cells to maintain ATP synthesis, and therefore viability, in the absence of IL-3 (105, 118, 122, 123). To determine whether activation of autophagy might drive the biophysical changes we observed following IL-3 depletion, we used Torin 1, an ATP-competitive inhibitor of mammalian target of rapamycin (mTOR) (82, 119), to induce autophagy in FL5.12 cells cultured in the presence of IL-3. mTOR signaling suppresses autophagy, and has been shown to be a downstream effector of IL-3 (124–126). As shown in Figure 3.2-5, cells treated with Torin 1 undergo a slight decrease in both volume and density (82). This phenotype contrasts with the larger decrease in volume and increase in density observed following IL-3 depletion (Figure 3.2-1 and Figure 3.2-2). One possible reason for the

discrepancy could be the timing of autophagy initiation. Density and volume begin to shift within hours of IL-3 depletion (Figure 3.2-1, Figure 3.2-2, and Figure 3.2-6), though the earliest time when increased autophagy can be measured has been previously reported as approximately 48 h after IL-3 withdrawal (127). To determine if the biophysical changes that we observe following IL-3 depletion occur independently of autophagy, we measured the appearance of LC3-II, a marker of autophagy (128), over time in either Torin 1-treated or IL-3-depleted FL5.12 cells. While Torin 1 induces a near maximal increase in LC3-II within 6 h, LC3-II begins to increase 18 h after IL-3 withdrawal with maximum levels not reached until 36 h of growth factor deprivation (Figure 3.2-5). In contrast to Torin 1 treatment, which induces autophagy and a very slight decrease in volume with no increase in density, IL-3 withdrawal results in autophagy initiation that occurs after cell density and volume begin changing. Thus, these data support our hypothesis that the biophysical changes resulting from IL-3 withdrawal occur prior to the initiation of autophagy.

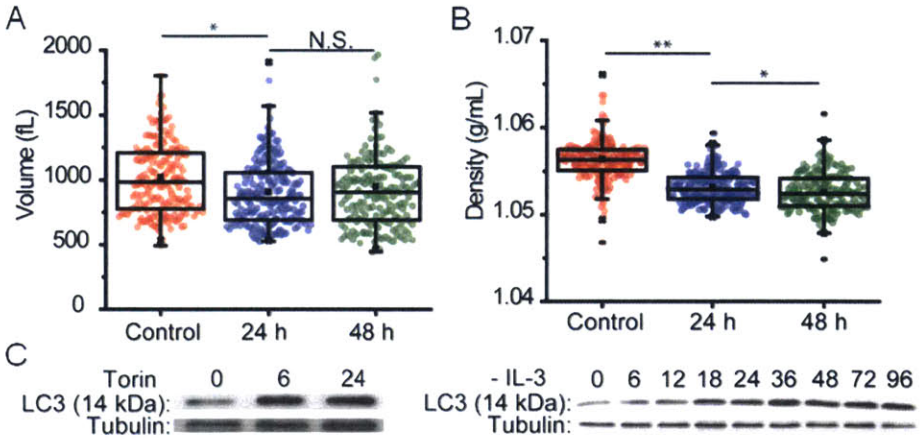

Figure 3.2-5. The biophysical response of FL5.12 cells to autophagy induction. Volume (A) and density (B) measurements of Torin-treated FL5.12 cells show a slight decrease in volume and a larger decrease in density. Single asterisk indicates $p < 9 \times 10^{-3}$, double asterisk indicates $p < 5 \times 10^{-32}$, and N.S. indicates no significance. Western blots (C) of LC3-II in FL5.12 cells treated with Torin (left) or withdrawn from IL-3 (right).

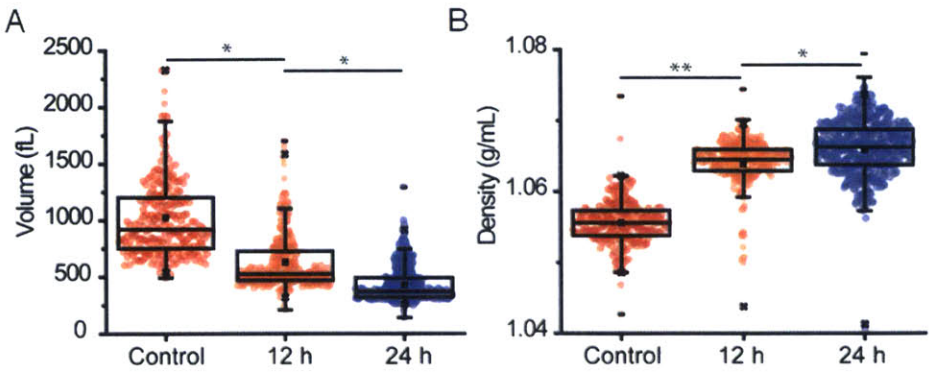

Figure 3.2-6. Short term changes to FL5.12 volume and density following IL-3 depletion. Changes to volume over the first 24 h following IL-3 depletion are shown in (A), and to density in (B). In (A),a single asterisk indicates $p < 3.1 \times 10^{-39}$. In (B), a single asterisk indicates $p < 1.8 \times 10^{-12}$, and a double asterisk indicates $p < 1.1 \times 10^{-62}$.

3.2.3 Biophysical changes allow adaptation to decreased nutrient uptake

We hypothesized that the acute biophysical changes following growth factor withdrawal could represent a metabolic adaptation to decreased nutrient uptake. In the absence of IL-3, Bcl-x_L overexpressing FL5.12s stop proliferating (129) (Table 3.2-1) and greatly reduce nutrient uptake (129, 130); however, homeostatic processes such as preserving cell membrane integrity and ion gradients continue to require ATP. Importantly, these processes consume relatively more ATP than do cell biosynthesis and growth (131), and meeting these fixed demands for ATP is critical for cell survival. Thus, we considered the possibility that the decrease in cell size and increase in density might partially compensate for decreased ATP production (117) by decreasing the amount of ATP required to perform maintenance processes.

To confirm that the capacity for ATP production is reduced following IL-3 depletion, we measured nutrient and oxygen consumption in FL5.12 cells in the presence and absence

of IL-3. In agreement with previous studies, both glucose and glutamine consumption are significantly suppressed in IL-3 depleted cells (Figure 3.2-7A and B) (119, 132). One source of ATP is fermentation of glucose to lactate. Consistent with decreased glucose consumption, lactate production is also abolished in IL-3 depleted cells (Figure 3.2-7C). The other major source of ATP production in cells is mitochondrial oxidative phosphorylation, which is fueled by oxidation of TCA cycle intermediates. As shown in Figure Figure 3.2-7D, oxygen consumption is decreased by approximately two-thirds in IL-3 withdrawn cells. This finding is consistent with decreased glutamine uptake, as glutamine is a major source of TCA cycle carbon in IL-3-dependent cells (130, 133). Because these cells remain viable and therefore must maintain an ATP to ADP ratio compatible with cell survival (117), decreased ATP consumption must compensate for the decreased ATP production.

While autophagy can provide substrates for ATP production following decreased nutrient uptake, the catabolism of these substrates to make ATP still requires either oxygen consumption or lactate production, and both were decreased in these cells. Thus, the cells must rely on additional adaptations to support survival despite decreased ATP production. We therefore considered how decreased ATP consumption could be linked to decreased cell size. Past studies have shown a similar percent increase in oxygen consumption in Bcl-x_L FL5.12 cells treated with gramicidin D in both IL-3 depleted and control cases (117). Gramicidin D uncouples the cytosolic Na^+/K^+-ATPase used to maintain the cell membrane potential, and thereby increases ATP consumption. The increase in ATP consumption requires an increase in ATP production, and gramicidin D has been classically used to drive increased mitochondrial ATP production in cells. The observation that IL-3 replete and depleted cells have a similar fractional increase in ATP production following

gramicidin D treatment, and that IL-3 depleted cells have lower ATP production relative to IL-3 replete cells suggests that IL-3 depleted cells require less ATP production to maintain the plasma membrane potential. Since the energetic cost of maintaining the plasma membrane potential is proportional to the cell surface area, this argues that a reduction in cell size contributes to energy savings. To test this idea, we determined if decreased ATP consumption in smaller, denser cells could be beneficial for cells in low nutrient conditions. Incubation of IL-3 treated FL5.12 cells with media lacking glucose causes a robust loss of viability after 48 h (Figure 3.2-7E). However, withdrawal of IL-3 for 24 h prior to, and during, a 48 h incubation in glucose-free media shows a relative protection from glucose withdrawal (Figure 3.2-7E). These data demonstrate that withdrawal of IL-3, and the decreased ATP requirements to maintain viability at a smaller size, can promote improved survival in nutrient depleted conditions.

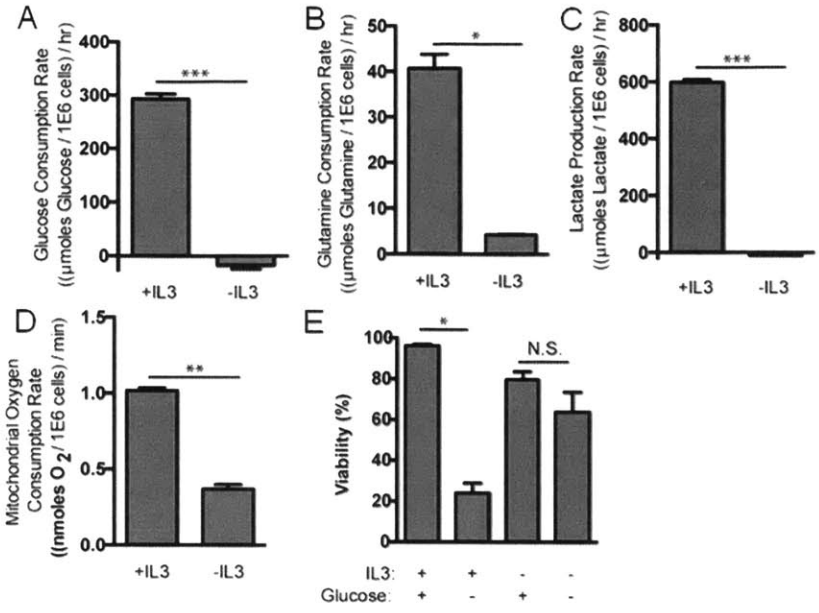

Figure 3.2-7. Changes in FL5.12 metabolism following IL-3 depletion.
IL-3 depletion causes decreases in glucose consumption rate (A), glutamine consumption rate (B), lactate production rate (C), and mitochondrial oxygen consumption rate (D). Glucose depletion leads to a decrease in viability in FL5.12 cells still exposed to IL-3, though not to cells depleted of IL-3 (E). Single asterisk indicates $p < 7.2 \times 10^{-3}$, double asterisk indicates $p < 2 \times 10^{-4}$, triple asterisk indicates $p < 1 \times 10^{-4}$, and N.S. indicates no significance.

3.2.4 IL-2 depletion in primary T cells leads to changes in density and volume

Previous studies have demonstrated a significant degree of overlap between the molecular events occurring after IL-3 depletion in Bcl-x_L FL5.12 cells and in the differentiation of activated lymphocytes to memory cells; in particular, both circumstances involve decreases in nutrient uptake, shifts in metabolism from glycolysis to oxidative phosphorylation, and upregulation of autophagy and anti-apoptotic protein expression (108, 109). To determine whether similar biophysical changes accompany growth factor withdrawal in primary lymphocytes, we investigated monoclonal CD8+ T cells taken from OT-1 transgenic mice and activated with a SIINFEKL peptide in the presence of IL-2.

Within 48 h following activation, naïve CD8+ cells are all proliferating (134) and undergo a significant increase in volume and decrease in density (Figure 3.2-8). This response is similar to that observed when IL-3 depleted cells are re-stimulated with IL-3 (Figure 3.2-4). Following the clearance of an infection, levels of IL-2 fall and cellular nutrient uptake is reduced(116, 135). Thus, we next measured the volume and density of a population of activated CD8+ cells following IL-2 withdrawal by removing exogenous IL-2 and adding an anti-IL-2 antibody to prevent stimulation from IL-2 produced by the activated cells (135). Depletion of IL-2 leads to a decrease in cell volume and increase in cell density that closely resembles what we observe following IL-3 depletion in FL5.12 cells (Figure 3.2-9). A population of control cells cultured continuously in the presence of IL-2 following activation for a similar time interval showed only a slight decrease in volume, but no noticeable change in density (Figure 3.2-8).

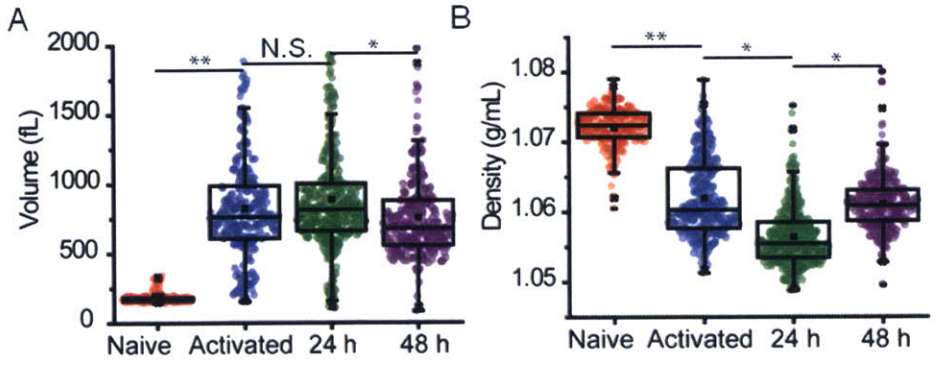

Figure 3.2-8. Biophysical responses of CD8+ OT-1 cells 72 h after activation with continued exposure to IL-2.
Changes to volume are shown in (A), and to density (B). In (A), a single asterisk indicates $p < 2.2 \times 10^{-7}$, a double asterisk indicates $p < 3 \times 10^{-67}$, and N.S. indicates no significant difference. In (B), a single asterisk indicates $p < 2.9 \times 10^{-36}$, and a double asterisk indicates $p < 2.3 \times 10^{-53}$.

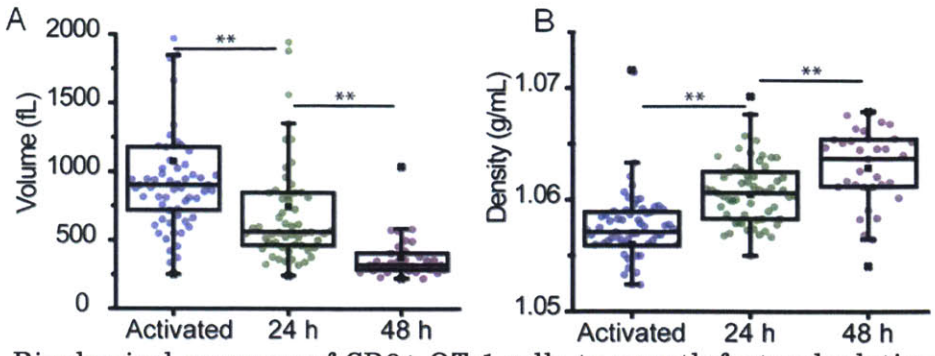

Figure 3.2-9. Biophysical response of CD8+ OT-1 cells to growth factor depletion. IL-2 depletion leads to a decrease in volume (A) and increase in density (B) in activated CD8+ cells. Double asterisk indicates $p < 8 \times 10^{-4}$.

To more closely model the process of differentiation towards memory cells, we resuspended activated CD8+ cells in media depleted of IL-2 and supplemented with IL-15, a homeostatic cytokine that promotes memory differentiation (116). Similarly to the case with Bcl-x_L-overexpressing FL5.12 cells, autophagy has also been identified as critical for memory cell differentiation; however, previous studies have shown that autophagy is initiated at a late time point (136). CD8+ cells depleted of IL-2 and supplemented with IL-15 demonstrate a similar decrease in volume and increase in density to those depleted of IL-2 exclusively (Figure 3.2-10). Interestingly, the ultimate volume and density of cells exposed to IL-15 is quite similar to that of naïve cells prior to activation (Figure 3.2-8). This similarity possibly reflects shared metabolic and physiological roles of both cell types, and further suggests a connection between biophysical properties and cellular metabolism and physiological role.

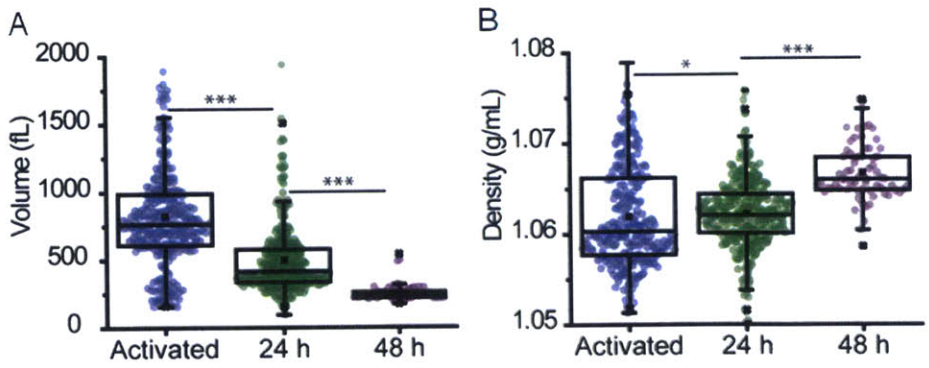

Figure 3.2-10. Biophysical to FL5.12 cells following exposure to IL-15.
Exposure to IL-15 also leads to a decrease in volume (A) and increase in density (B) in activated CD8+ cells. A single asterisk indicates $p < 0.01$, and a triple asterisk indicates $p < 5 \times 10^{-18}$.

3.3 Discussion

We have demonstrated that growth factor depletion in lymphocytes results in a conserved biophysical response that helps promote cell survival in nutrient-poor conditions. We have found that Bcl-x_L overexpressing FL5.12 cells decrease in volume and increase in density following IL-3 depletion, and that this change is also observed in primary activated CD8+ cells during memory differentiation. We demonstrate that this change occurs prior to the initiation of autophagy, and propose that these biophysical changes comprise an acute adaptation to a nutrient-deprived state.

While the molecular implications of growth factor presence or absence have been widely studied, the biophysical changes that occur have not. We propose that these changes result from a broader process of maximizing metabolic efficiency and optimizing resource allocation in lymphocytes. The tremendous breadth of the immune repertoire of a typical organism requires that most lymphocytes remain quiescent for a majority of their lifetimes, though in a state that is primed for rapid activation. Here, we propose that a

high-density, low-volume state assists in the metabolic adaptation to decreased nutrient uptake. Whereas a lower volume reduces the energy required for cellular maintenance processes, a higher density in this low-volume state allows retention of cell material such as nucleic acids and proteins that are energetically expensive to synthesize and could be accessed by autophagy as metabolic substrates. Retaining these materials also decreases the resources required to re-grow to a size needed for proliferation if the cells are re-activated.

Interestingly, we find that the changes in cell density and volume occur prior to autophagy initiation, known to be critical for survival of growth factor depleted lymphocytes (108, 115, 127). Autophagy plays several roles in memory lymphocytes, including clearing damaged organelles and macromolecules, and providing energy under conditions of limited nutrient uptake due to the absence of stimulatory growth factor. In certain cases, it has been described as the primary source of metabolic precursors following growth factor depletion; however, its initiation has been identified as occurring at relatively late time points, in agreement with our findings (108, 127, 136). Because ATP turnover in cells occurs on a much faster time scale, adaptations to decreased nutrient uptake are required to maintain ATP production for maintenance functions during the time interval requisite for autophagy initiation. Moreover, we find the biophysical outcomes of pharmacologic induction of autophagy to be different from those of growth factor depletion, causing a slight decrease in cell size with kinetics that are slower than the acute decrease in size observed immediately following growth factor withdrawal. Thus, we propose that prior to activation of autophagy to support cellular bioenergetics, the cell acutely reduces ATP requirements by decreasing in volume and increasing in density.

Biophysical parameters, such as density and volume, represent the aggregate outcome of multiple complex molecular events triggered by loss of growth factor signaling. Similarly, changes to density or volume likely affect many downstream pathways. For example, the issue of molecular crowding resulting from an increase in density has been identified as disruptive to protein folding equilibria and responsible for longer diffusion times (2, 4). These issues could potentially occur in the non-proliferating, high density cells that we study here; proliferating cells may be better served with a lower density, which is presumably associated with a larger cytoplasm and more space available for protein synthesis, signaling, and other essential cellular processes. This might explain why both naïve cells and IL-3 depleted cells increase volume and decrease density prior to dividing when stimulated with IL-2 or IL-3, respectively. Our results also argue that the acute change in volume following growth factor withdrawal is not only due to exit from the cell cycle, as the cell volume decreases to less than half of the mean volume of the cycling population. Whether this biophysical response allows adaptation of cells to energy stress in other contexts remains to be determined; these data nonetheless establish a link between cell biophysical properties and cell survival in a nutrient-deprived state.

3.4 Materials and methods

3.4.1 Cell culture

FL5.12 cells were grown at 37°C in RPMI 1640 media (Life Technologies) supplemented with 10% (v/v) FBS (Sigma Aldrich, St. Louis, MO), 10 mL Antibiotic-Antimycotic (Life Technologies, Grand Island, NY), and 0.01 mg/mL IL-3 (R&D Scientific, Minneapolis, MN). For IL-3 depletion, a confluent (10^6/mL) culture was washed three times

in RPMI without IL-3, and resuspended in RPMI without IL-3 at a concentration of $4x10^5$/mL. Approximately 0.25 mL of the culture was removed every day for measurement in the SMR. For glucose depletion, a confluent (10^6/mL) culture was washed three times in RPMI lacking glucose and supplemented with 10% v/v dFBS (Sigma Aldrich), and resuspended at a concentration of $4x10^5$/mL in RPMI supplemented with 10% v/v dFBS and 0.01 mg/mL IL-3. For Torin treatment, a culture at a concentration of $4x10^5$/mL was supplemented with 250 nM Torin 1 (gift of David Sabatini). OT-I splenocytes were activated *in vitro* with 1 µg/ml $OVA_{257-264}$ peptide (SIINFEKL, Sigma) in RPMI 1640 with 10% (v/v) FBS and 55µM 2-mercaptoethanol (Life Technologies). For the IL-2 experiments, blasting, viable, CD8+ T cells were FACS sorted after 24h of activation and seeded at a concentration of $2x10^5$ cells/mL in media with either 100 U/mL IL-2 (PeproTech, Rocky Hill, NJ) or 1 µg/ml anti-IL2 (JES6-1A12 clone, eBioscience, San Diego, CA) for the +IL2 and –IL2 conditions respectively. For the IL-15 experiments, cells were FACS sorted after 48h of activation and seeded at a concentration of $2x10^5$ cells/mL in media with either 100 U/mL IL-2 or 10 ng/mL IL-15 (PeproTech). In both cases t_0 refers to the time at which the cells were exposed to varying cytokine conditions.

3.4.2 Confocal microscopy and high-throughput cell phenotyping

Cells were fixed with 4% paraformaldehyde (Sigma) for 10 min at room temperature and permeabilized with 0.1% Triton-X (Life Technologies) for 10 min. To block non-specific binding, cells were incubated with PBS (Life Technologies) supplemented with 10% FBS (ATCC, Manassas, Virginia) for 30 min. For immuno-staining, cells were incubated with anti-Bcl-x_L antibody (Abcam, Cambridge, UK) and anti-mitochondria antibody (Abcam) for 1 h. Nuclear DNA and actin filaments were marked with Hoechst 33342 (Sigma Aldrich)

and Alexa-Fluor phalloidin 488 (Life Technologies), respectively. Imaging of immuno-stained cells was performed with a Nikon A1 confocal laser microscope equipped with a 60x oil immersion objective (Nikon, Tokyo, Japan). Immunofluorescence confocal images collected every 1μm in the z-direction were projected onto the xy-plane (137) (Figure 3.2-3 top panels). For high-throughput cell phenotyping, fluorescence images of immuno-stained cells were collected with Nikon TE300 fluorescence microscope equipped with a DS-QiMc camera (Nikon). Nuclear area, cell area, and mitochondria intensity were assessed with a customized MATLAB code (121). More than 5000 cells were assessed per condition (Figure 3.2-3).

3.4.3 Immunoblotting

Protein was extracted from 3 x 10^6 FL5.12 cells in RIPA buffer containing protease inhibitors (Roche, Basel, Switzerland) and measured by western blot using standard methods. The primary antibodies used were anti-LC3 antibody (M152-3, MBL International) and anti-α-tubulin (ab176560, Abcam).

3.4.4 Viability

Cell viability was determined by propidium iodide (PI) exclusion using standard methods. FL5.12 cells were suspended in media with or without IL-3 for 24 h prior to, and subsequently during a 48 h incubation in glucose-free or replete media. Cells were then resupended in 1 μg/ml PI, and PI incorporation was measured by flow cytometry (BD FACS Canto II) and quantified (FACS Diva Software).

3.4.5 Mitochondrial oxygen consumption

Oxygen consumption rate was measured from 10^7 IL-3 treated or withdrawn FL5.12 cells/mL using an Oxytherm instrument (Hansatech, Norfolk, UK). The slope of the linear range of oxygen depletion was used to measure basal oxygen consumption rate. Non-mitochondrial oxygen consumption rate was measured following treatment with 2 µM antimycin and 2 µM rotenone. The difference between basal and non-mitochondrial oxygen consumption was calculated to determine mitochondrial oxygen consumption rate.

3.4.6 Metabolic measurements

Metabolic excretion and consumption measurements from the media of FL5.12 cells were determined with an YSI 7100MBS (YSI Life Sciences, Yellow Springs, Ohio) according to manufacturer's protocols. FL5.12 cells treated with IL-3 or withdrawn from IL-3 for 24 h were resuspended at 3 x 10^6/ml in fresh RPMI for 3 h and metabolite levels in the media were quantified. The measurements were then normalized to cell number subtracted from metabolite levels measured in media without cells to determine consumption and production rates in each condition.

3.4.7 Statistical analysis

Box plots in Figure 3.2-1, Figure 3.2-2, Figure 3.2-4, Figure 3.2-5, Figure 3.2-6, Figure 3.2-8, Figure 3.2-9, and Figure 3.2-10 represent the interquartile range of the experimental data, and whiskers represent the 5^{th} and 95^{th} percentile of the data. Statistical significance was determined using a Wilcoxon rank-sum analysis. Error bars in Figure 3.2-3 and Figure 3.2-7 represent standard deviation. Statistical significance in Figure 3.2-7 was determined using an unpaired, parametric t test with Welch's correction.

Chapter 4

A microfluidic approach for characterizing lymphocyte avidity interactions

4.1 Introduction

The process of eliminating infection, mediated by cells in the adaptive immune system, depends almost entirely on high-fidelity recognition of antigen. This recognition is characterized by the interactions of antigen-presenting cells (APCs), which process and display the antigen, with lymphocytes that interact with the APCs and recognize the antigen. The ability of lymphocytes to distinguish among different antigens results from the diversity of the immune repertoire, and the specificity of the receptors of only one or a few cells for a particular antigen. A recognition event is characterized by a high affinity interaction between a lymphocyte receptor and a peptide presented on a major histocompatability complex (MHC) of an APC, followed by the engagement of accessory receptors to form an avidity interaction. This recognition event is associated with a cascade of inflammatory consequences, ideally resulting in successfully eliminating the pathogen.

Understanding, predicting, and engineering avidity interactions is critical for a wide variety of clinical objectives. In general, affinity between T cell and pMHC is considered to be one of the primary indicators of T cell activity (138, 139). Vaccines against many common viruses often depend on selecting or designing a viral epitope with the maximum affinity for a T cell receptor or MHC molecule (140). Recent work into the pathogenesis of HIV has identified the ability of host cells to recognize viral particles via an avidity interaction as critical for identifying and controlling the virus (141, 142). However, in certain cases, a high avidity between a T cell and its target poses a disadvantage. For example, studies regarding cancer T cell vaccines have indicated the possibility than an adjuvant with intermediate-affinity is most effective at generating tumor-targeting cytotoxic T cell clones (143). Moreover, in adoptive T cell therapy, modulating the affinity of the engineered TCRs is crucial for ensuring targeting of the tumor while minimizing autoimmunity (144).

Current methods for analyzing affinity or avidity can be loosely divided into three-dimensional and two-dimensional techniques. Three-dimensional methods involve three degrees of freedom of motion of the pMHC, TCR, or both; this usually requires at least one component floating freely in solution. By analogy, two-dimensional methods involve two degrees of freedom of motion, and both pMHC and TCR being confined to a surface (145). Three-dimensional methods, which have typically higher throughput and are more widely adopted, include tetramer staining and surface plasmon resonance (SPR). In tetramer staining, recombinantly synthesized biotinylated pMHC monomers are bound together by a streptavidin complex conjugated to a fluorescent molecule (146). Cells are incubated with the tetramer, rinsed, and sorted using flow cytometry to identify cells expressing TCRs specific to the pMHC. A tetramer, rather than a monomer, increases the stability of the

TCR-pMHC interaction, but reduces the resolution of the technique. Thus, some amount of degeneracy in TCR binding can lead to multiple TCR clonotypes binding a single pMHC; individual clonotypes must then be identified through an alternative method.

SPR can serve as an alternative to tetramer staining. A metallic surface is functionalized with a recombinantly synthesized TCR, and individual pMHC molecules, also recombinantly synthesized, are flowed over the surface. To ensure that immobilizing the TCR does not cause a conformational change that might affect binding kinetics, a binding site or linker must be carefully selected. During an experiment, the functionalized metallic surface is illuminated at a range of angles close to the angle of total internal reflection. At the angle of total internal reflection, electrons on the surface will absorb the light energy and begin to resonate; the remainder of the light illuminating the surface will be reflected to a detector placed at a known angle from the surface. Protein binding, as occurs with TCR association with pMHC, will change the angle of total internal reflection, which is monitored by the detector. Monitoring the dynamics of how this angle changes provides information about the kinetic parameters governing the interaction (147).

Despite the widespread adoption of three-dimensional methods, significant arguments can be made in favor of two-dimensional methods more closely reflecting true biology (145, 148). For example, the confinement of both pMHC and TCR to a membrane limits their motion, resulting in a more stable interaction when the two come into contact; furthermore, confining both components to membranes helps partially reproduce the contribution of mechanical deformability to initiation of an interaction. One such two-dimensional measurement technique involves Förster resonance energy transfer (FRET) between a pMHC immbolized to a lipid bilayer and a TCR in a cell membrane, each fused to a fluorophore (149). A measureable FRET signal is generated when the TCR comes in close

proximity to the pMHC, and decreases as the interaction breaks and the two drift apart from each other. Thus, kinetic parameters can be extracted from the system by monitoring the FRET signal.

Another two-dimensional approach involves measuring an adhesion frequency between a T cell and a red blood cell (RBC) decorated with a low density of pMHC on its membrane using micropipette aspiration (150). In this method, a T cell and RBC are each immobilized onto a micropipette, and placed in opposition to each other. The micropipettes are then brought into close proximity and separated at a predetermined frequency using an automated stage. This assay provides information about likelihood of attachment, based on the number of adhesion events that occur over the total number of collisions, and duration of adhesion, based on the deformability of each of the cells. Furthermore, the interaction can potentially be described as the combined outcome of a series of individual, rapid interactions which occur as the TCR samples the surface of an APC (145).

Both the two- and three-dimensional methods are associated with significant limitations. Interestingly, the kinetic parameters obtained from each method are not always in agreement (145). Moreover, three-dimensional methods provide interaction strengths that do not always predict functional outcomes, namely ability of lymphocytes to recognize antigens and eliminate an infection *in situ* (141). However, the throughput on the two-dimensional methods is very low, while the expertise required to perform them is very high (149, 150).

Importantly, both categories of measurement require prior knowledge of the structure of the pMHC, the TCR, or both. This limits their utility in analyzing clinical samples, which do not necessarily originate from patients with well characterized TCRs or

pMHCs. Finally, the interactions measured using these methods are typically affinity interactions, or between a single receptor and ligand; even in cases in which multiple ligands and receptors are engaged, as with tetramer staining, the interaction is between a set of homogeneous ligands and receptors. An immunological synapse, resulting from TCR-pMHC recognition, engages a suite of accessory receptors proximal to the TCR and pMHC which serve to stabilize the interaction and initiate downstream responses (151).

Thus, a method for measuring the avidity between a TCR and pMHC in a context which more closely reflects the biology of the interaction has the potential to provide substantial insight into basic science questions and clinical outcomes. We have developed a microfluidic approach to accomplish this goal. In our system, APCs are loaded with antigen and hydrodynamically trapped in a channel. T cells are then flowed by the trapped cells, and the interactions between the T cells and trapped APCs are recorded optically with a microscope camera. Parameters such as velocity, attachment rate, or pressure needed to detach cells that are paired, are extracted with an image processing algorithm. This approach allows us to monitor true biological interactions in real-time, including activation via a fluorescent marker for calcium staining, and has the potential to be interfaced with sorters or collectors for downstream processing.

4.2 Device design

4.2.1 Eight port configuration

As a first approach, we designed a microfluidic device with a single, narrow channel with two bypasses, and flanked above and below by two wide channels that serve as

pressure reservoirs (Figure 4.2-1). We fabricated the design in silicon, to help promote uniformity among devices. The narrow channel, or the main flow channel, contains hydrodynamic trapping structures to capture the APCs (Figure 4.2-1B). T cells are flowed through this main flow channel, where they interact with the trapped APCs (Figure 4.2-1B). The pressure reservoir channels on either side of the main flow channel facilitate flushing and sample introduction. These channels are held at a lower pressure than the main flow channel, and this pressure difference holds the trapped cells in place (Figure 4.2-1B). A more detailed diagram of the pressure and fluidic arrangement is shown in Figure 4.2-2.

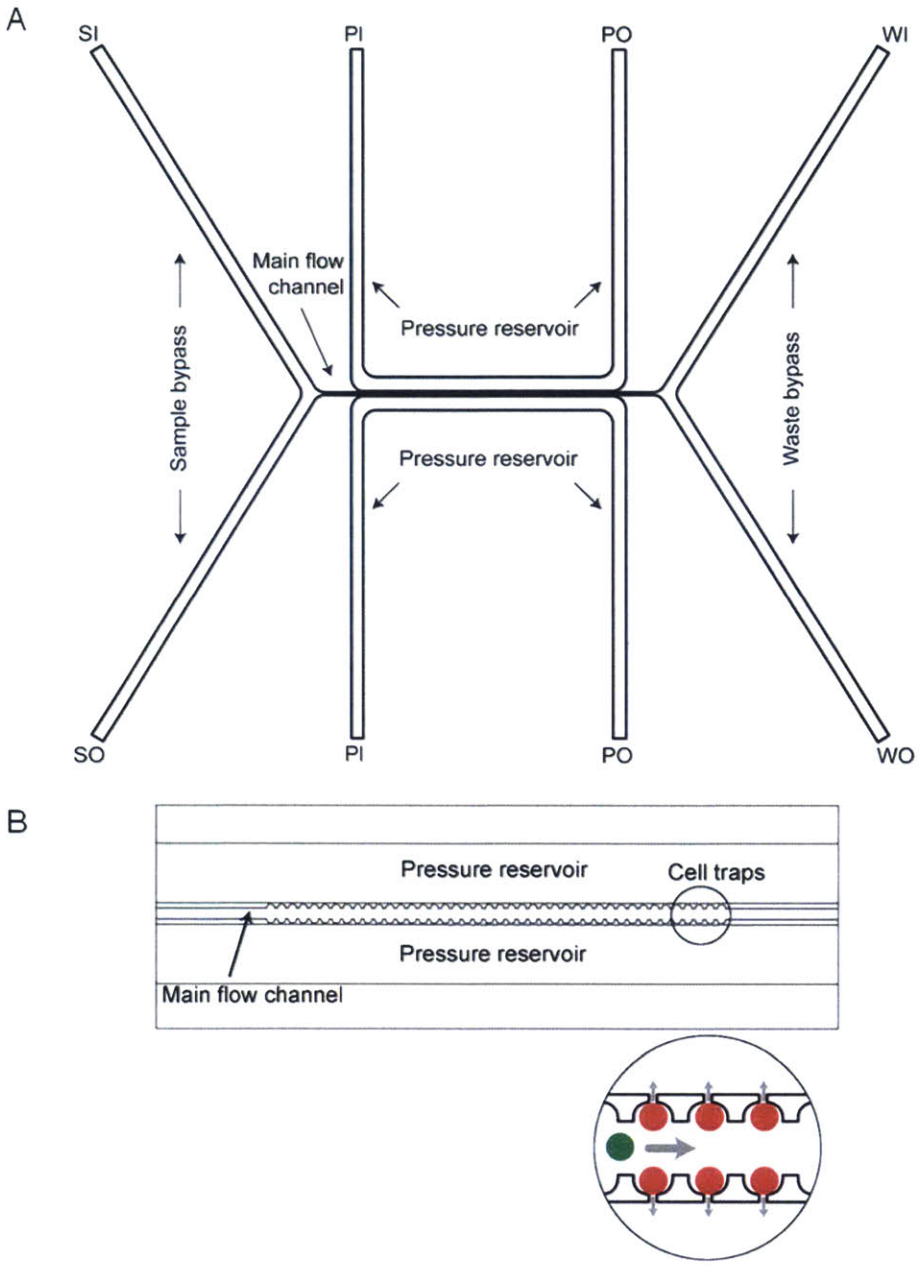

Figure 4.2-1. Schematic of eight port design for measuring cell-cell avidity. Overall chip design shown in (A). Higher magnification of region of main flow channel shown in (B). Region shown in inset in lower right hand corner demonstrates the trapping mechanism in greater detail. Flow through the traps maintains APCs (red) captured, while a T cell (green) passes though the main flow channel. A pressure drop down the main flow channel (wide gray arrow) drives fluid flow, and a smaller pressure drop between the main flow channel and the pressure reservoirs keeps the APCs trapped.

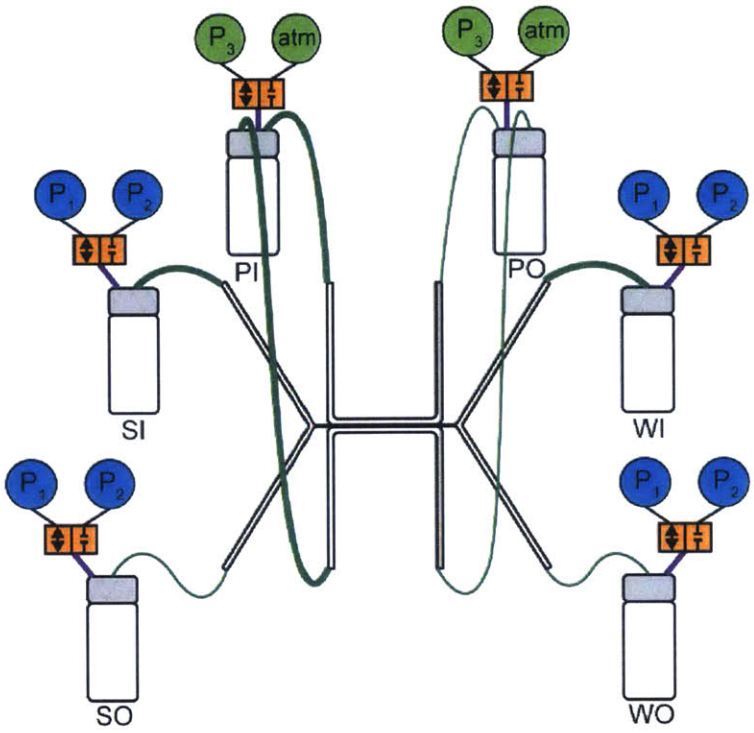

Figure 4.2-2. Diagram of fluidic and pressure components in eight port configuration. Solenoid valves (orange rectangles) set waste vial pressures to those of the pressure regulators (blue or green circles). Wider green lines connect the channels on the device to the vials indicate thicker tubing. The solenoid valves upstream of SI, WI, SO and WO are connected to two pressure regulators shared among the four vials (P_1 and P_2, blue circles). The valves upstream of PI and PO are connected to a third pressure regulator and atmosphere (P_3 and atm, green circles).

Prior to the start of an experiment, the device is rinsed with PBS to ensure that the channels are free of debris, and then the surface of the device is passivated with polylysine grafted polyethyleneglycol (PLL-PEG) (Figure 4.2-3A). A typical experiment involves the following steps: (1) flushing the right-hand bypass with media or PBS containing APCs; (2) balancing the pressure between WI and WO on the right-hand bypass channel to pinch the flow and direct APCs to the main flow channel, where they are captured in the hydrodynamic traps; (3) replacing the vial with APCs with a vial containing blank media or PBS, and flushing both bypass channels with media to remove any uncaptured APCs; (4) replacing a vial on the lefthand bypass channel with a vial containing T cells; (5) flushing the lefthand bypass channel with media or PBS containing T cells; (6) balancing the

pressure on the lefthand bypass channel to pinch the flow and direct T cells into the main flow channel, where they should interact with the captured APCs (Figure 4.2-3). At the end of an experiment, the device is rinsed extensively with PBS and bleach to remove any residual material.

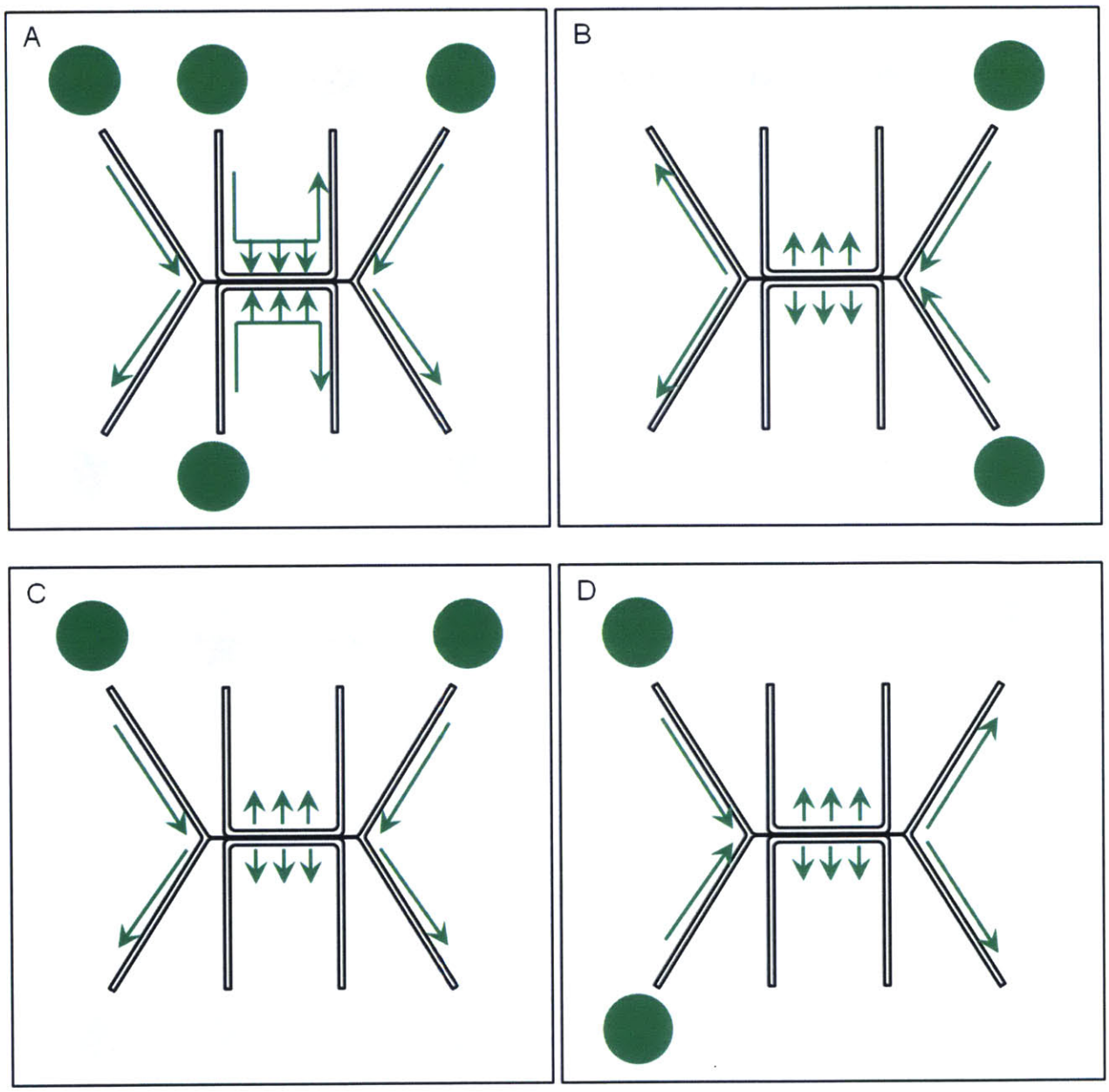

Figure 4.2-3. Experimental workflow for eight port design.
Green circles indicate ports with high applied pressure, and gray circles indicate ports with low applied pressure. Green arrows indicate approximate direction of flow. Prior to beginning an experiment, the chip is rinsed with buffer and the surface is passivated with PLL-PEG (A). Though most of the fluid flow is along the bypasses, a small amount is present across the traps as well, as indicated by the small green arrows perpendicular to the main flow channel. Next, APCs are loaded into the traps (B). Small green arrows perpendicular to the main flow channel indicate flow through traps. Excess beads are rinsed out, and beads that have been trapped remain trapped (C). Finally, cells are flowed into the main flow channel from the opposite bypass channel (D). Cells travel across the main flow channel and interact with trapped beads.

After preliminary experiments, we determined that different steps in our experimental workflow worked best with particular flow conditions. For example, rinsing the system before or after an experiment is most effective with minimal flow through the main flow channel. This way, debris in the bypasses will be directed towards the bypass outlets, rather than towards the traps in the main flow channel. When loading APCs, a narrow range of pressure drops across the traps is required to keep the APCs in place while not allowing them to squeeze through the traps to the pressure reservoir channels. Furthermore, this pressure drop must be maintained when rinsing the bypasses prior to introducing the T cells, including the points when the APC vial is switched for a plain media vial, and when the plain media vial at the sample inlet is switched for a vial containing T cells. When the T cells are introduced, the velocity across the main flow channel must be slow enough to allow time for interactions between the T cells and the trapped APCs. This objective is made more challenging by the fact that the flow rate is constant throughout the chip, and that fluid velocity is inversely proportional to channel diameter. Thus, an appropriate flow rate must be identified to ensure sufficiently slow flow velocity in the main flow channel, but sufficiently rapid flow velocity in the bypass channels to prevent cells from settling. In addition to being relatively slow, the velocity must also be relatively uniform; because we wish to see changes in velocity caused by cell-cell interactions, we wish to ensure that velocity changes related to channel geometry be reduced to a minimum.

To better understand and predict fluid flow through the chip, we used finite element analysis software (COMSOL) to model the fluid flow through the chip. We focused on understanding the flow patterns during the rinsing step (Figure 4.2-3 A), which occurs both prior to the start of an experiment and at the end of an experiment. Sources of debris

include both cellular material from previous experiments and incomplete clearance of byproducts of the fabrication process. We wished to understand whether we could identify a configuration under which we could rinse the bypass channels with high pressure and maintain little to no flow across the main flow channel. In other words, we wanted to determine whether the flow across the main flow channel could be decoupled from the flow across the bypass channels and the pressure reservoir channels. The ability to decouple the flow in this manner can greatly facilitate clearing debris from the bypass channels, as it ensures that debris not stick in the traps in the main flow channel (Figure 4.2-1).

We thus conducted a parametric sweep of combinations of possible pressure values at the SI, PI, and WI ports (Figure 4.2-4A). We considered both the effect of changing the ratio of applied pressure at the different ports, and the absolute value applied at a given ratio. As shown in Figure 4.2-4B, when the pressure applied at the SI port is equal to 6 psi, a pressure ratio for SI:PI:WI of approximately 1:1.24:1 provides the minimal flow rate through the main flow channel. However, when the pressure is increased or decreased, this optimal ratio no longer holds, as shown in Figure 4.2-4C; either raising or lowering the pressure results in an increased amount of flow through the main flow channel. The practical implication of this outcome is that avoiding trapping debris in the main flow channel is very challenging. While the model can provide a reasonable estimate for a range of appropriate pressures, because precisely determining the resistances across the channels and tubing is difficult, the optimal values predicted by the model may not necessarily hold true experimentally. Next, even if optimal ratios could be determined for all possible pressure values, the pressures at SI, WI and PI could not be changed independently of each other, at the risk of catching debris in the main flow channel. Additionally, there appears to be an increase in flow through the main flow channel at all ratios when the pressure is

increased (not shown). When rinsing, high pressures are often required to dislodge stubborn debris and to ensure that the channels are truly clear. Thus, the requirement of avoiding high pressures also impairs the process of rinsing.

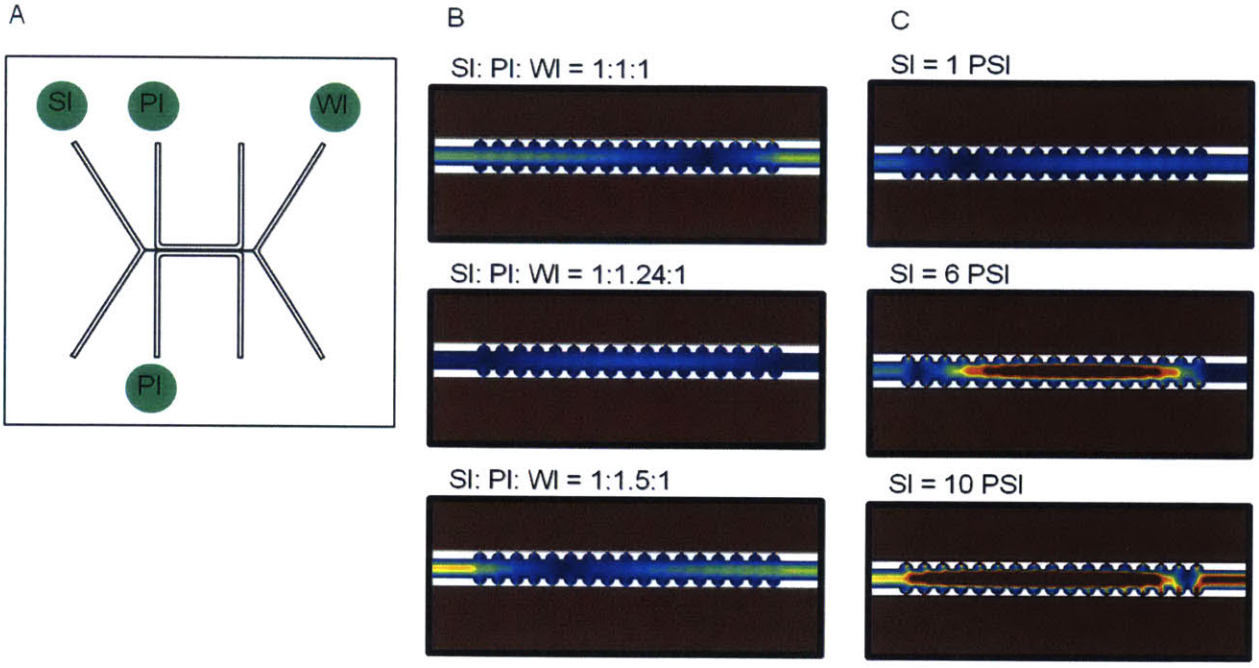

Figure 4.2-4. COMSOL modeling of fluid flows through the main flow channel. Schematic of chip design indicating pressure configuration (A). Green circles indicate high applied pressure, gray circles indicate low applied pressure (0 PSI). Changing the SI:PI:WI pressure ratio changes the flow profile across the trap region (B). Values immediately above image indicate the ratio of SI to PI and WI. SI was set to 6 psi. Changing the value of applied pressure with a constant SI:PI:WI ratio (1:1.25:1) also changes the flow profile across the trap region (C). Heat map values for (B) and (C) range from high flow (dark red) to no flow (dark blue).

Additionally, when flowing T cells over already loaded APCs, the flow across the main flow channel is not uniform along the length of the channel, an outcome we observed empirically. Consequently, cells will flow very quickly into the channel entrance, and slow down at some midpoint along the channel. Thus, if we wished to measure changes to cell velocity as a marker of interaction between T cells and APCs, we would first need to conduct a rigorous series of controls to correct for variations in velocity inherent to the chip.

Most of the challenges that we encountered with this design can be attributed to our inability to decouple flow across the bypass channels and the pressure reservoir channels from that across the main flow channel, as shown in both Figure 4.2-3 and Figure 4.2-4. This coupling occurs due to the asymmetric fluidic connections between the main flow channel and each of the other channels. Furthermore, predicting flow profiles in real-time, particularly during an experiment, poses a challenge due to the complexity of the design. As a result, identifying and troubleshooting problems associated with fluidics becomes very challenging as well. Thus, we determined that the eight port design lacked the robustness necessary for the precise nature of the cell measurements we wished to conduct in the future.

4.2.2 Four port configuration

Based on the challenges associated with operating an eight-port design, we considered approaches for reducing the design complexity. Previous work identified one such design, shown in Figure 4.2-5, which involves a serpentine channel configuration with traps between channel turns (152, 153). The length of the channel in a single turn of the serpentine is sufficiently long such that its resistance is greater than that across the hydrodynamic trap (Figure 4.2-5). The outcome is that a cell that flows through the channel will be captured in an empty trap. Cells that pass by will travel along the serpentine to the next available empty trap. To increase the throughput of this design, we arranged a series of three traps for each turn of the serpentine (Figure 4.2-5C). We confirmed with COMSOL that this channel configuration would still maintain the appropriate resistances to capture cells in the traps (Figure 4.2-6). This configuration eliminates the need for the separate pressure reservoir channel used in the eight-port

design. The four-port design provides an advantage from a throughput perspective as well, because we can fit twice the number of devices on each silicon chip during fabrication; thus, even if the top half of the chip is no longer useable, the chip can be reversed and the bottom half used (Figure 4.2-5A).

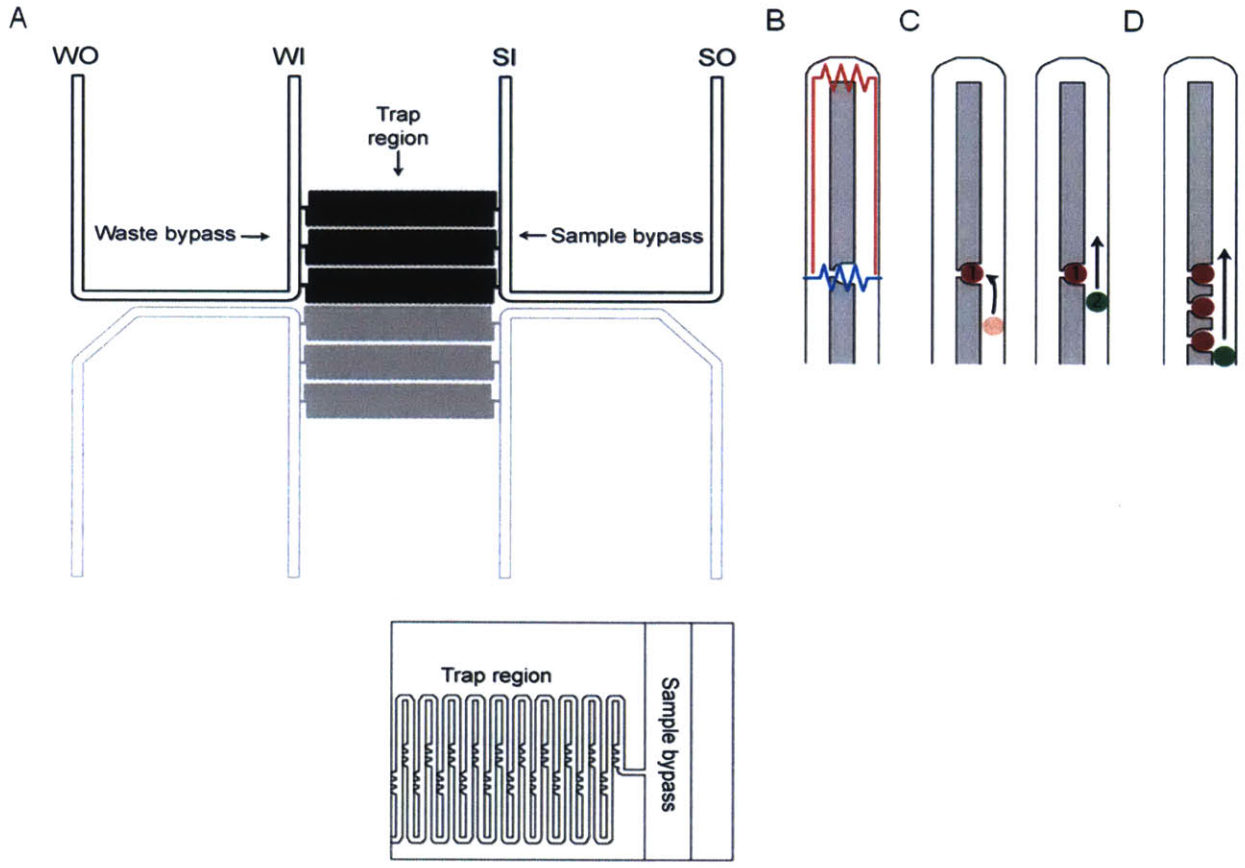

Figure 4.2-5. Schematic of four port design for measuring cell-cell avidity.
The channel configuration, as seen on an individual chip (A). Bottom half, shown in gray, represents an independent device. Higher magnification of connection between sample bypass channel and trapping structures is shown in the inset. When unoccupied, the resistance across a single cell trap (blue line) is lower than that across the turn of the channel (red line) (B). Thus, a cell traveling down the channel will flow into an unoccupied trap (C, red circle). When another cell (C, green circle) travels down a channel with an occupied trap, it will pass by the cell and continue along the turn of the channel. To increase throughput, numerous traps can be placed in series along a single channel (D).

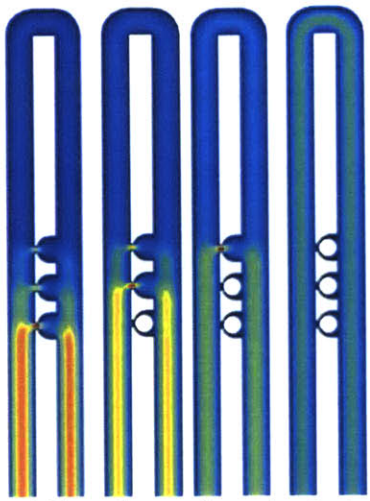

Figure 4.2-6. COMSOL modeling of flow through a single turn in the serpentine channel of the four-port design.
The flow through the channel ensures that traps are occupied sequentially (white circles). Heatmap colors range from red, indicating regions of highest flow, to dark blue, indicating regions of lowest flow.

We wished to use a similar experimental workflow as described in §4.2.1, with the slight modification that both APCs and T cells be loaded in the same bypass channel rather than opposite bypass channels (Figure 4.2-3). Using COMSOL, we identified appropriate pressure configurations that would allow us to operate under our desired flow regime. As shown in Figure 4.2-7, the symmetry of the design allows us to uncouple the flow across the traps from the flow down the bypass. Thus, when pressure is applied to both upstream ports (SI and WI), the bypasses can be flushed at high pressure without introducing any flow across the traps. However, small amounts of flow can be introduced through hydrostatic pressure applied by adjusting the heights of the vials. Thus, unlike in the eight-port design, the velocity across the traps can be slow while the velocity in the bypass channels can be rapid. This improvement facilitates flushing excess APCs from the bypass channel after the traps are loaded, introducing T cells after APCs are loaded, and maintaining a consistent supply of T cells throughout the experiment. Furthermore, the velocity along the length of the serpentine channel is relatively constant. These conditions substantially simplify the workflow, and improve robustness and reproducibility. Based on

this analysis and preliminary experiments, we determined that this design would be appropriate for an initial study into the feasibility of using a microfluidic approach for measuring interactions between T cells and APCs.

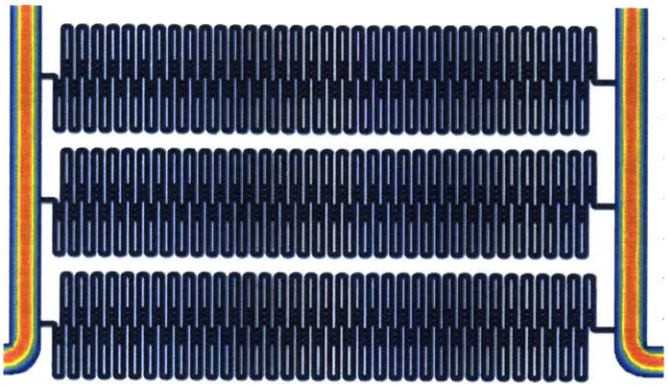

Figure 4.2-7. COMSOL modeling of fluid flow across channels in four-port design. Pressure is applied to upstream ports of bypass channels. Heatmap colors range from red, indicating regions of highest velocity, to dark blue, indicating regions of lowest velocity.

4.2.3 Modeling APCs with functionalized beads

Though our goal is to measure T cell-APC interactions, we chose to first evaluate the interactions between functionalized beads and Jurkat cells, a T cell line. We hoped that this model would allow us to characterize our experimental system and gain an understanding of the dynamic range of our measurement without having to waste precious primary cell samples. The beads we chose were functionalized with αCD3 and αCD28, often used in primary T cell activation and known to interact with the surface of Jurkat cells (154).

However, this approach is associated with certain drawbacks, relating to both biological relevance and engineering challenges. From a biological standpoint, the interaction between the beads and the Jurkat cells is not that of an immunological synapse, but rather that of an antibody with a receptor. Thus, even if we can distinguish a specific

interaction between beads and cells, we may not necessarily be able to distinguish an interaction between two cells. Furthermore, the lack of deformability of the beads may also affect the way in which they interact with the cells, as deformation of the APC membrane has been shown to play a crucial role in T cell activation (149).

This lack of deformability also affects the engineering challenges associated with this approach. Though the bead stiffness may facilitate loading into the traps without concern for squeezing or shearing, it also results in a greater frequency of clogging the narrow channels (Figure 4.2-1 and Figure 4.2-5). Additionally, because the bead diameter (15 μm) is slightly smaller than the channel height (19 μm), a slight pressure drop across the traps remains even when they are occupied. This pressure drop can lead to non-specific interactions between beads and cells that are pulled into the occupied traps. Nonetheless, we found that beads provided a useful proof-of-concept for operating the device.

4.3 Results

4.3.1 Experimental workflow

Each experiment begins by loading beads into the traps. As shown in Figure 4.3-1, single beads can be loaded relatively easily into each trap in the trap region in the serpentine channel. Because the beads do not deform, this step can be performed with a high pressure drop across the traps (SI = 15 psi, all other ports at atmospheric pressure, Figure 4.2-5). After beads are loaded, the sample bypass and tubing are rinsed with PBS to remove excess beads. This step is performed at approximately 6 psi applied to both WI and SI, to reduce the flow across the serpentine channel and avoid trapping any additional beads or debris. By applying a small amount of hydrostatic pressure at the SI port, the

beads remain trapped in spite of the symmetric pressure applied at the regulators (Figure 4.2-7).

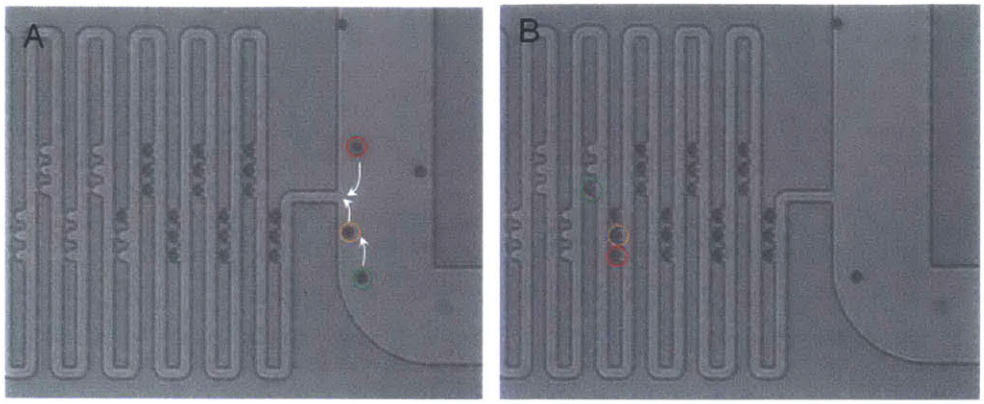

Figure 4.3-1. Loading beads into traps.
Beads (inside red, orange and green circles, A) flow from the bypass channel into the trap channel (white arrows). Pressure across the traps causes the beads to be captured, while the ratio of the bead diameter (15 μm) to the trap diameter (20 μm) ensures that only a single bead is captured in each trap.

After excess beads are rinsed, cells are introduced in the sample bypass channel. During this step, approximately 6 psi of pressure is applied at both SI and WI to ensure minimal flow across the serpentine trap channel. This step is critical to ensure sufficient flow for carrying the cells from the sample vial to the bypass channel, while preventing the cells from shearing through the traps due to a high pressure drop; even though the beads occupy most of the trap volume, the cells are sufficiently deformable to pass above, below, or around the sides of the bead and through the trap. When cells are observed in the right hand bypass channel, the pressure is reduced to approximately 0.15 psi, and flow is pinched through the serpentine by applying pressure at SO as well as SI and WI. Every five minutes, the sample bypass is flushed to introduce a new plug of cells. Data is recorded via image acquisition software associated with the microscope camera (uEye Cockpit, Imaging Development Systems GmbH, Obersulm, Germany). To achieve the maximum possible frame rate, the image is cropped at the top and the bottom (Figure 4.3-2). Each experiment

is run for between 0.5 and 1 h. At the end of an experiment, the channels are rinsed with PBS and then bleach to remove residual cellular debris.

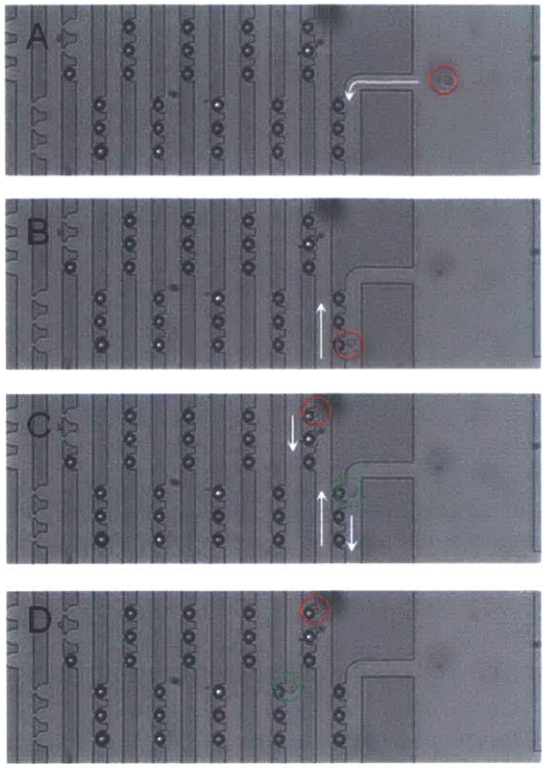

Figure 4.3-2. Observing cell passage through channels loaded with beads.
A cell (red circle) enters the serpentine channel (white arrow) from the sample bypass (A). The cell travels along the serpentine, passing by and contacting the beads (B). While the first cell is flowing through the channels, a second cell (green circle) is introduced (C). The first cell remains trapped on one of the beads, but the second cell continues flowing through the channel (D).

4.3.2 Data analysis

Images obtained from movies recorded during experiments are processed using a custom MATLAB script to determine the velocities of cells passing through the serpentine trap region. First, the trap region is divided into lanes. Each lane consists of a series of three traps and the length of channel either above or below that contains no traps (Figure 4.3-3). The trap region is determined based on manual user selection of the specific regions of the channel. In future versions of the code, replacing this step with an automated

method to distinguish between a trap region and a non-trap region may improve the accuracy and speed of the processing. Next, particles—i.e. potential cells—are identified in each frame of the video using a built-in MATLAB circle-finding algorithm. Particles that are immobile for a defined number of frames are eliminated from further processing steps; because the beads remain trapped for the duration of the experiment, they do not interfere with subsequent steps in which cells are identified. A tracking algorithm is then used to identify circular particles that appear in consecutive or nearly consecutive frames. If a circle appears for a sufficiently large number of consecutive frames, it is identified as a cell with a velocity equal to the total number of pixels traveled between two consecutive frames.

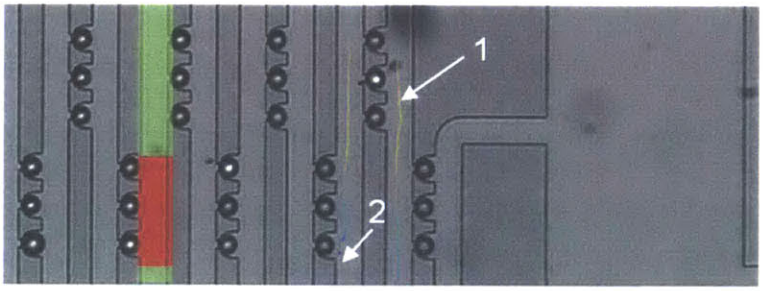

Figure 4.3-3. Data processing method for measuring cell velocity across the serpentine trap channel.
Cell velocities, indicated by the colored lines (1 and 2) along each lane of the serpentine are evaluated independently of all other lanes. Bluer hues indicate a slower velocity, and yellower hues indicate a faster velocity. If a cell is trapped with a bead, its velocity trace will terminate in the vicinity of one of the traps (2). The velocity of a cell across the trap region (red box) is scaled by the velocity of that cell across the region without traps in the same lane (green boxes).

A cell will be tracked in a lane until either it reaches a zero velocity, indicating that it has been trapped, or until it reaches the bounds of the field of view. If a cell is trapped in a region of the channel not designated as a trap region, its velocity trace is discarded. Additionally, the cell velocities in each lane are considered independently of those in the adjacent lanes. The data must be processed in this way as a consequence of the edges of the image being cropped, which removes the portion of the image that includes the turns of the

serpentine channel that connect adjacent lanes. The reason for reducing the field of view of the camera is to increase the frame rate, which is inversely proportional to the height of the image; increasing the frame rate is necessary for the tracking algorithm to be implemented successfully. With a sufficiently low concentration of cells, we would be able to assume that a cell that disappears from view at the end of one lane would appear some amount of time later in the next lane. However, because there are often multiple cells in a lane at a time, and that there are occasionally clumps of cells or other obstructions in regions of lanes outside the field of view of the camera, we cannot reliably implement this assumption. Thus, each data point represents the trajectory of a single cell along a single lane of traps. For example, for the experiment represented by the image shown in Figure 4.3-3, the maximum number of data points for a single cell would be nine, since nine lanes have traps fully occupied with beads. However, this maximum is often not reached because individual cells will stick to trapped beads, and therefore not travel the entire length of the serpentine.

Though the pressure applied by pressure regulators is maintained at the same value between experiments, slight differences in vial heights or the presence of debris can lead to differences in applied pressure, which subsequently can be a cause for changes to cell velocity. To ensure that this variation in applied pressure does not affect our conclusions regarding cell-bead interactions, the velocity across the cell trap region is scaled by the velocity across a region without traps in the same lane (Figure 4.3-3). Thus, the metric provided by the algorithm is a velocity ratio, or the ratio between the velocity across the trap region to the velocity across the region without traps. In spite of this adjustment, we still aim to maintain as consistent an absolute velocity as possible between experiments, because we cannot be sure if a threshold velocity exists above which no interactions will be

observed. In the future, this is a value worth estimating both mathematically, based on the bond strengths between a TCR and its binding partners, and confirming experimentally.

4.3.3 Preliminary results

To evaluate the feasibility of using the velocity ratio to monitor the interactions between Jurkat cells and antibody-coated beads, we compared the velocity ratio from a measurement of Jurkat cells flowing past αCD28/αCD3 coated beads with a measurement of Jurkat cells flowing past unfunctionalized beads. As shown in Figure 4.3-4, we did not observe a significant difference between the velocity ratio measured in each of the two measurements.

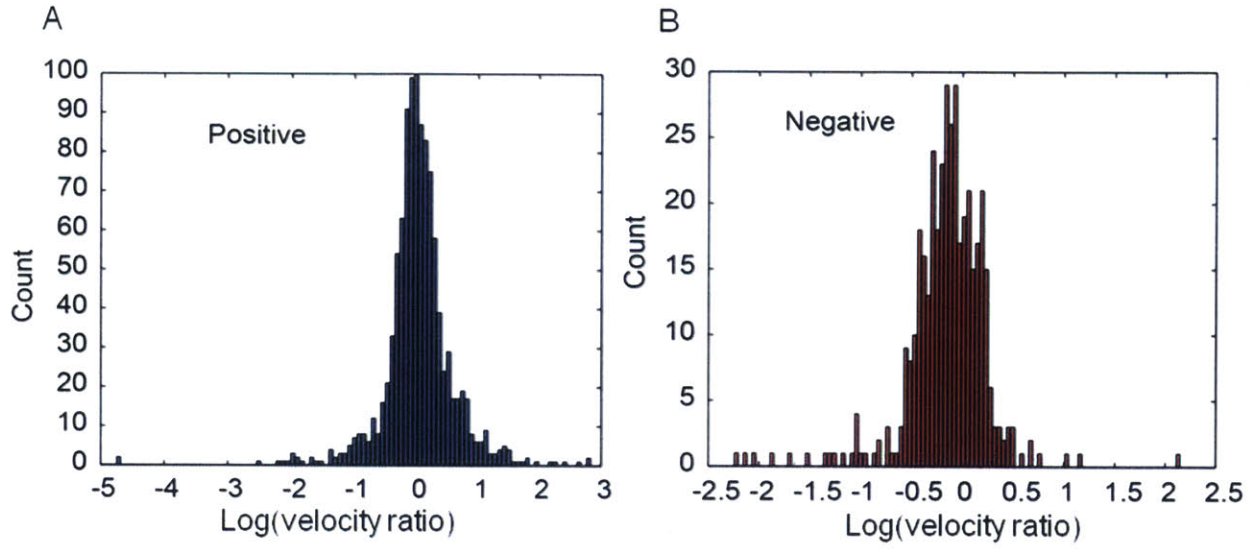

Figure 4.3-4. Histograms of cell velocity ratios.
Experiments shown are either with anti-CD28/anti-CD3 coated beads (Positive, A) or uncoated (Negative, B) beads. No significant difference can be observed between the two data sets. The number of events recorded in (A) is >1000, and the number of events recorded in (B) is >400.

To better understand possible reasons for the fact that we did not observe a difference between the two datasets, we first inspected the velocity ratios for each lane individually in each experiments (Figure 4.3-5). First, we wished to determine whether

there was a drift in ratios over the span of the lanes due to a gradient in applied pressures from the right to the left sides of the device. Based on the information shown in Figure 4.3-5, we could find no significant observable trend in velocity ratio across the different lanes of the device, suggesting that the pressure configuration that we use for running experiments does not introduce significant measurement artifacts of this nature.

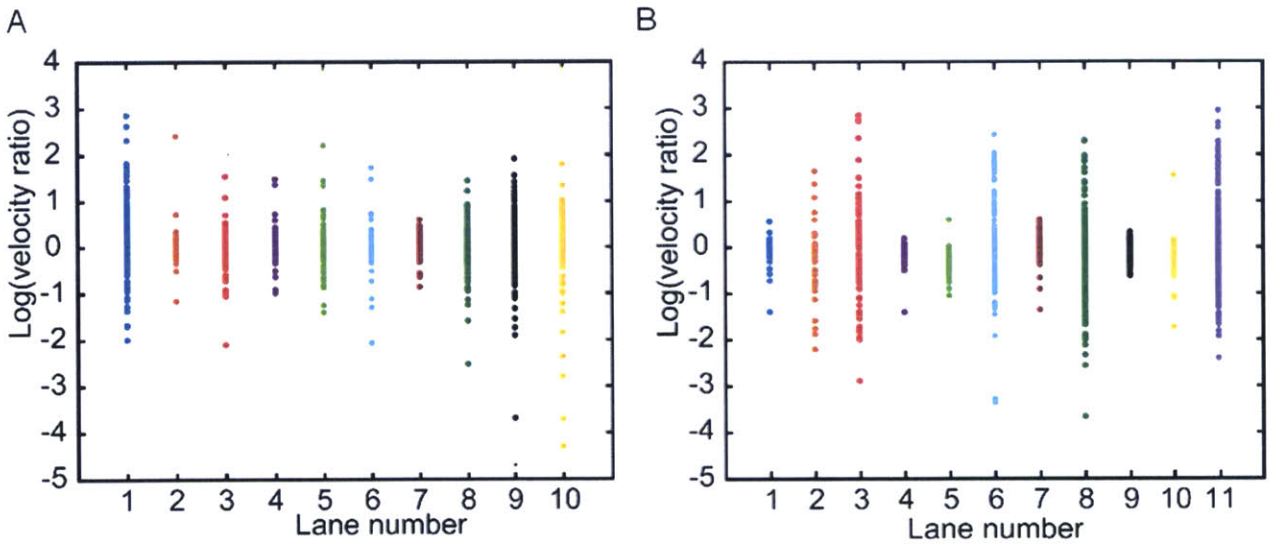

Figure 4.3-5. Velocity ratios per lane over the course of an experiment.
Data for αCD3/αCD28 beads is shown in (A) and for uncoated beads in (B). Lanes are numbered in ascending order based on proximity to the right-hand bypass channel (Figure 4.3-3).

We did observe, however, that the range of velocity ratios among the different lanes can vary significantly. We suspected that this could be partially due to cells being trapped on the beads and subsequently constricting the width of the serpentine channel (Figure 4.3-3). In a narrower channel, smaller cells will travel more quickly, due to a constant volumetric flow rate throughout the device, and the fact that this flow rate is the product of velocity and cross-sectional channel area. Thus, when trapped cells reduce the cross-sectional area of the channel, the fluid velocity will increase, which will consequently increase cell velocity as well. However, when a larger cell encounters the decreased cross-

sectional area, it may be forced to deform to enter, and will encounter significant resistance as it passes through. This will cause larger cells to travel more slowly through the trap region, and display an increased velocity ratio through a channel constricted by captured cells. This outcome suggests that the wider variation in some of the channels is due to the formation of a cluster of trapped cells on a particular bead or set of beads.

We next evaluated the absolute velocity of the cells over the course of the experiment in individual lanes. Shown in Figure 4.3-6 are sample lanes from the αCD3/αCD28 experiment. We compared lane 1 (Figure 4.3-6A, C and E), which appeared to have a wide range of velocity ratios (Figure 4.3-5A) with lane 7 (B and D), which appeared to have a much narrower range of velocity ratios. As expected, the absolute velocities mirrored this pattern. While the majority of the velocities for lane 7 are within a relatively narrow range, the velocities in lane 1 are highly dispersed. Furthermore, the velocity over time of cells traveling through a channel that is not obstructed appears to follow a relatively reproducible pattern, as shown in panels C and D. Thus, a cell will first enter a channel, speed up slightly as it approaches the set of three traps, slow down as it passes the traps, then return to its original velocity. When the channel is obstructed, this pattern is not at all present, and the velocity traces of individual cells resemble noise (E). We found this observation to be consistent when we compared the velocity traces from the other channels shown in Figure 4.3-5, both for the coated and uncoated beads (data not shown).

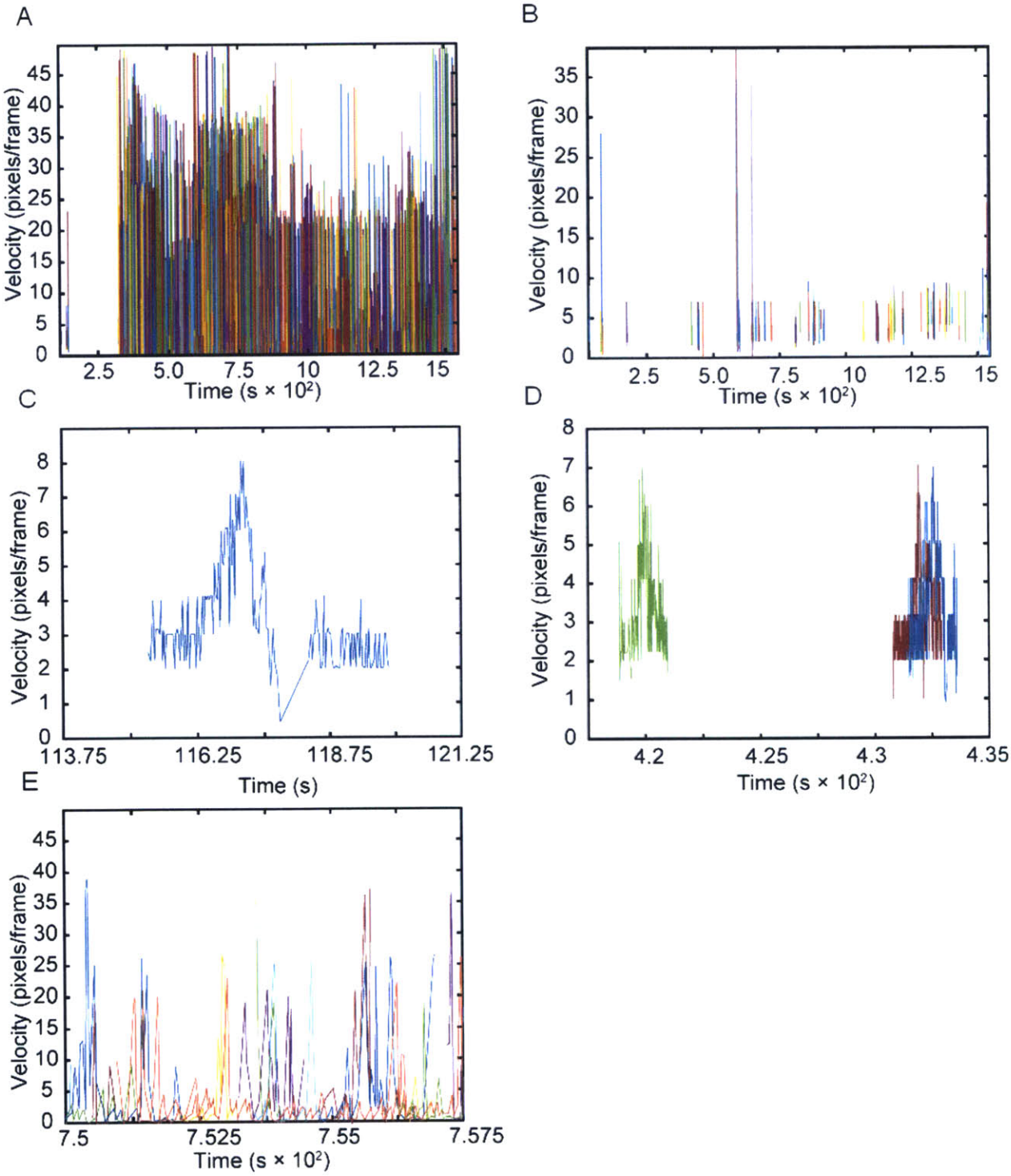

Figure 4.3-6. Absolute velocity over time in individual lanes.
Absolute velocity over time for lane 1 (A, C and E) and lane 7 (B and D), corresponding to the experiment depicted in Figure 4.3-4A and Figure 4.3-5A. Velocities over the course of the entire experiment vary significantly between lane 1 (A) and lane 7 (B). Each color represents the velocity of a single cell over time. Cells are tracked from when they first

enter the lane until they exit. The substantial overlap of colors in (A) suggests that many cells are trapped in the lane at the same time. Snapshots from the beginning of the experiment in lane 1 (C), middle of the experiment in lane 7 (D), and middle of the experiment in lane 1 (E) indicate how velocity patterns differ when cells travel through a lane that is generally clear and one that is partially blocked by trapped cells. Overlapping blue and red trajectories in (D) demonstrate the presence of two cells in lane 7 at the same time, though at different positions. The persistence of a low velocity trace in (E) further suggests that cells are immobilized in the channel.

4.4 Conclusions and future work

Based on our promising preliminary results, we plan to continue developing and refining this microfluidic method for measuring avidity interactions between T cells and APCs. First, we aim to repeat the experiments comparing the functionalized and non-functionalized beads to determine whether a significant difference can be observed in any aspect of the velocity ratio parameter. Though we have demonstrated that a single experiment can be conducted with relatively high throughput (Figure 4.3-4), we cannot yet determine whether these experiments provide us with meaningful data. In particular, we are concerned about nonspecific interactions that occur due to the charge on the surface of non-functionalized beads; this can be addressed by coating the beads with certain passivating agents such as bovine serum albumin or polylysine-polyethylene glycol. Additionally, certain design parameters can be adjusted, such as the pitch of the corners of the capture structures or the width of the gap serving to establish the pressure drop in the capture structure, to prevent mechanical trapping of cells in a non-specific manner.

One approach for controlling for non-specific interactions could be to combine our measurement with a functional readout, such as fluorescence staining to monitor calcium release that follows T cell activation. Previous studies have shown that this occurs in Jurkat cells that are stimulated with αCD3 (155). By correlating a functional output with our measurement, we may be able to better determine such parameters as the total amount

of contact time required between a cell and a bead to initiate an activation event, and whether multiple short collisions can lead to activation. We also expect that a functional output will help in validating our method. We have demonstrated the feasibility of measuring fluorescence in our system, including the fluorescence from a Ca^{2+} reporter (Fluo-4). We have also demonstrated with flow cytometry that exposure to αCD3/αCD28 beads is sufficient to elicit a change in fluorescence in Jurkat cells stained with Fluo-4.

However, certain of the challenges associated with optimizing an experiment which involves using beads as APCs will not be reproduced in experiments using the APCs themselves. With this in mind, we will also begin exploring our options regarding the best experimental systems to use for optimizing parameters for monitoring cell-cell interactions. We expect that the first option will be evaluating the interactions between activated T cells and B cells from an OT-1 mouse. We consider this model to be an appropriate next step for our purposes due to its biological relevance and relatively easy logistical accessibility. OT-1 lymphocytes are relatively well characterized, and we have the option of testing our system with a panel of commercially available peptides with varying affinities for the OT-1 TCR. We hope that this approach will also improve our ability to compare our method with the current state of the art techniques for measuring affinity and avidity; this may prove challenging because our method may provide information that is not directly analogous to that obtained from SPR or tetramer staining. Finally, though the issue of logistics may seem relatively easily solved, we have found that accessing interesting clinical samples is not always straightforward; with OT-1 cells, we will have the opportunity to further test the device with relative autonomy, and without consuming precious clinical samples.

Once we have rigorously characterized the system, we will proceed to investigate its applications for addressing questions in both basic science and in a clinical setting. As

mentioned briefly in the previous paragraph, we are not yet certain whether our method will provide information that is directly comparable to that obtained from SPR, tetramer staining, or any of the newer 2D methods (§4.1). For example, in order to determine a k_{on} or K_d, we may need to measure fewer cells but with significantly higher imaging resolution per cell or incorporating the capability to track clustering of fluorescently labeled receptors. Because these methods are inherently challenging and low-throughput, we may find that a more worthwhile approach is to focus on extracting less complex information, but from a larger cohort of cells. We expect that this approach will be most readily comparable to tetramer staining, though we expect our results to have higher resolution and fidelity to biological outcomes, albeit with significantly lower throughput. Thus, just as tetramer staining can be used to identify a subpopulation of cells interacting with a specific pMHC of interest, we may choose to attempt to identify subpopulations of cells interacting with APCs presenting antigens of interest. We aim to have the ability to sort these subpopulations for additional downstream analysis, including clonal expansion and single-cell sequencing.

4.5 Materials and methods

4.5.1 Cell culture

Jurkat cells were cultured as previously described (156). Briefly, cells were grown at 37°C in RPMI 1640 media (Life Technologies) supplemented with 10% (v/v) FBS (Sigma Aldrich, St. Louis, MO), 10 mL Antibiotic-Antimycotic (Life Technologies, Grand Island, NY), and 0.01 mg/mL IL-3 (R&D Scientific, Minneapolis, MN). Cells were passaged every 2-3 days, or when the culture reached confluency (~10^6/mL).

4.5.2 Bead synthesis

15 μm carboxylated polystyrene beads were obtained from Bangs Laboratories (Fisher, IN). Beads were functionalized with αCD3 and αCD28 antibody (Biolegend, San Diego, CA) using a protein coupling kit (Polysciences, Inc., Warrington, PA) and according to manufacturer's instructions. First, a concentrated antibody solution, with a total mass of protein between 200 and 500 μg, was prepared by centrifuging 500 μL of a 1 mg/mL antibody solution in a 150 kDa microcentrifuge filter tube at 14000 x g for 15 minutes. Beads were rinsed 2x by centrifuging 125 μL of beads in solution (~12.5 mg total beads) in a 0.1 μm microcentrifuge filter tube at 14000 x g for 2 minutes, then resuspending in coupling buffer provided by Polysciences, Inc. Following the second rinse, beads were resuspended in 170 μL coupling buffer. To activate the beads, 20 μL of a 200 mg/mL solution of 1-Ethyl-3-(3-dimethylaminopropyl)carbodiimide (EDAC) (SigmaAldrich, St Louis, MO) in coupling buffer was added, and the beads were incubated in an inverting rotator for 15 minutes. The concentrated antibody solution was then added to the activated beads, and incubated for at least 60 minutes. Functionalized beads were then rinsed twice with washing/storage buffer provided by Polysciences, Inc., and stored at 4 °C.

4.5.3 Cell staining

To measure Ca^{2+} release, cells were stained with Fluo-4 (Life Technologies), according to manufacturer's instructions. A 5 mM stock solution of Fluo-4 in DMSO was first prepared, and stored at -20 °C. Immediately prior to use, 1 μL of stock solution was diluted to 1 mL in PBS supplemented with 0.02% Pluronic F-127. The dye solution was added to a cell pellet consisting of between 2 and 10 x 10^6 cells. Cells were incubated with

stain at room temperature in the dark for 20 minutes. Cells were then washed 1x with PBS, and 2x with HBSS. Staining efficacy was evaluated using flow cytometry.

Appendix A

Additional observations regarding cell density

A.1 A pre-apoptotic signature

An interesting phenomenon that we observed incidental to other measurements was a pronounced decrease in density prior to apoptosis in cells subjected to a variety of environmental stresses (Figure A.1). We observed this in both suspension cells (Figure A.1A, B and D), and an adherent cell line (PC3, Figure A.1C). Interestingly, while the BaF3 and FL5.12 cells are exposed to known apoptotic inducers, in the case of the PC3 cell line, this outcome is observed when cells are exposed to Kolliphor buffer, which is used fairly regularly for fluorescent staining. To the best of our knowledge, Kolliphor is considered non-toxic, but the outcome from the density measurement has the potential to suggest otherwise.

We do not fully understand this phenomenon, but are able to rule out several possibilities. First, we are fairly certain that it is not due to cell membrane permeabilization, as this would cause the cells to become filled with Fluid 2, and therefore sink in Fluid 2 rather than float; in other words, their buoyant mass in Fluid 2 would be positive instead of negative. This switches the direction of the peak (§1.2.1.1 and Figure

1.2-2), and leads us to discard the measurement. What we observe here appears to be the opposite—the cells become less dense, which would indicate that their buoyant mass in Fluid 2 becomes more negative (Figure 1.2-1).

An additional effect that we can rule out is the so-called Apoptotic Volume Decrease (AVD). AVD is a process during which cell volume decreases in the early stages of apoptosis due to cell water loss (10, 157, 158). Interestingly, the inverse has also been observed—i.e. that significant cell water loss is sufficient to induce apoptosis (159). However, this change would cause cell density to increase rather than decrease, particularly if it were due primarily to water loss and not associated with any loss of mass. In fact, there is a possibility that the change in density that we observe when we expose FL5.12 cells to STS (§2.2.3) is due to this effect.

In order to more fully interpret this observation, additional studies are necessary. For example, cells can be stained with Annexin V, or another fluorescent marker of early apoptosis, and imaged simultaneously with the SMR measurement. Additionally, cells with a low density can be sorted from cells with a high density, and analyzed further to identify their phenotypic status. Unfortunately, these experiments are beyond the scope of this document, and will be left as future work. Nonetheless, this observation can be considered an additional useful indicator for cell status and health under certain conditions.

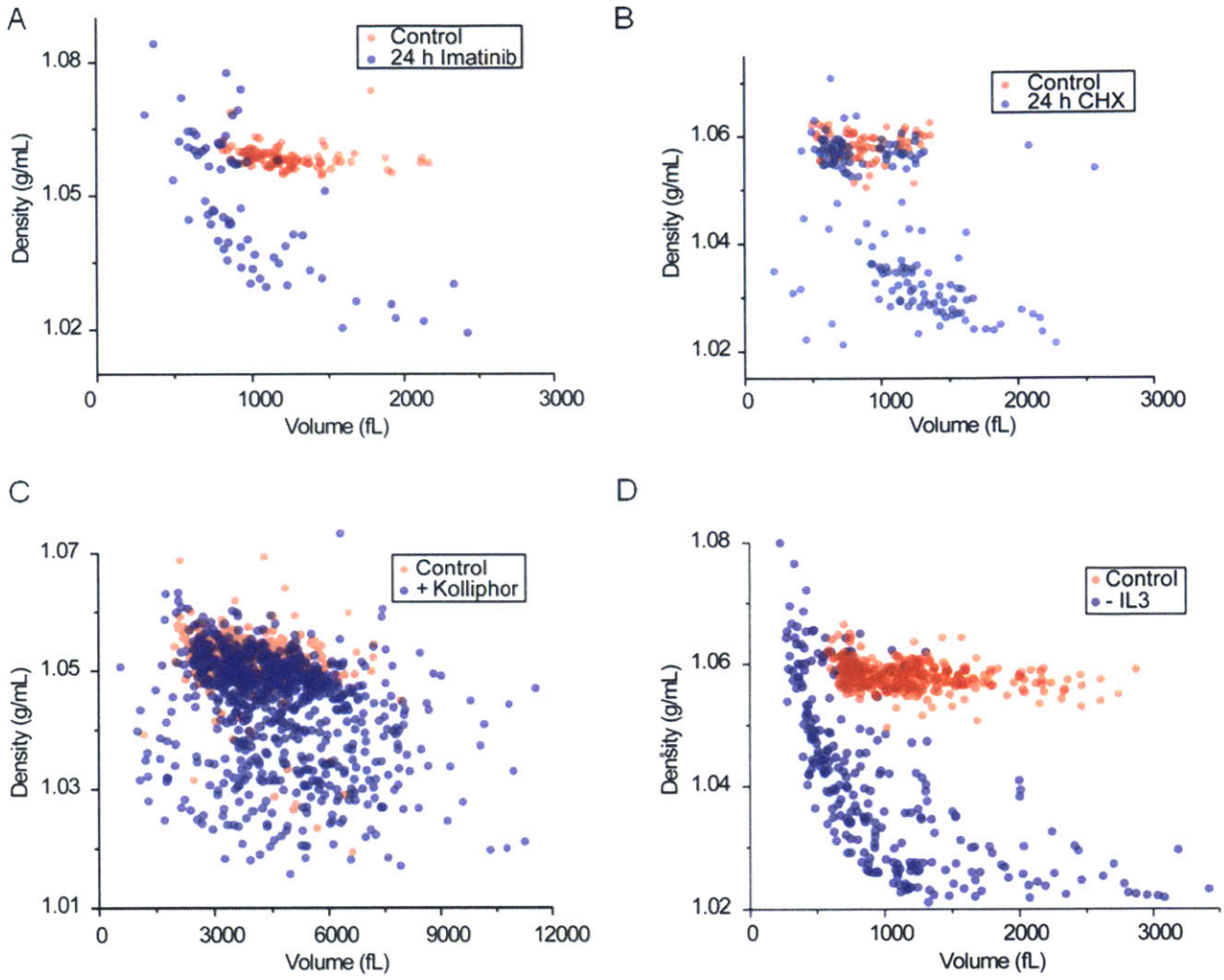

Figure A.1-1. A pre-apoptotic signature observed in multiple cell types under a variety of conditions.
BaF3 cells treated with Imatinib (A), FL5.12 cells treated with cycloheximide (B), PC3 cells exposed to Kolliphor buffer (C), and FL5.12 cells depleted of IL-3.

A.2 A brief mathematical elaboration on the narrowness of the density distribution

The relatively small changes to density that we observe are an outcome of both mathematics and biology. Because the density of most intracellular components is relatively close to one, the bounds for the maximum and minimum density values for a cell

are also relatively close to one; moreover, even cell types with very different volumes can have relatively similar densities. The biological significance of the narrow density distribution has been discussed at length elsewhere in this manuscript (§2.23.2, and 3.3), so here we will continue to discuss its mathematical significance.

We will begin by further describing why the changes that we observe in density are so small. We can consider a test cell, which decrease in volume by losing some fraction of water such that the ratio of its initial volume (V_1) to its final volume (V_2) is α:

$$\alpha = \frac{V_1}{V_2}$$

A.2-1

Using the definition of density as the ratio between mass and volume, we can define a ratio between the initial density (ρ_1) and mass (m_1) and final density (ρ_2) and mass (m_2):

$$\frac{\rho_1}{\rho_2} = \frac{m_1/V_1}{m_2/V_2}$$

A.2-2

Simplifying, and combining equations 1 and 2 gives:

$$\frac{\rho_1}{\rho_2} = \frac{1}{\alpha} * \frac{m_1}{m_2}$$

A.2-3

Cell mass and cell volume are close in value, as indicated by the value of density typically being close to one. Thus, the ratio between m_1 and m_2 is fairly close to the value for the ratio between V_1 and V_2, and therefore almost equal to α. This leads to the ratio between the initial and final densities to be very close to one. For example, we can consider the values of volume and density of the control (300 mosm) cell mentioned above. If the volume decreases by 10% due to water loss, from 1000 fL to 900 fL, then α = 1.11. If the

density is 1.057 g/mL, then the mass will decrease from 1057 pg to 957 pg; because the density of water is approximately 1 g/mL, a loss of 100 fL of water will equal a loss of 100 pg of mass. Using equation 3, we can calculate the ratio of ρ_1 to ρ_2, and it comes out to be 0.99. Thus, a 10% decrease in volume leads to slightly less than a 10% decrease in mass, and a 1% increase in density. This outcome reflects the experimental results that we observe following osmotic challenge, as shown in Figure 2.2-1.

Perhaps the most striking feature of density is its low degree of variance relative to volume or mass. However, the possibility still exists that the reason for the narrow distribution of density values is related to how density is defined. As shown in Figure 2.2-1, the variability in cell density among multiple measurements appears to be much smaller than that of volume. Thus, while the range of density values for control measurements (300 mosm) spans from 1.055 to 1.058 g/mL, or approximately 0.2% of the mean, the volume range spans from approximately 800 to 1200 fL, or nearly 20% of the mean. This outcome suggests that cell density is more tightly regulated than cell volume. We can also consider the standard deviation, which we can calculate assuming that the volume follows a lognormal distribution (99). In this case, the geometric mean and standard deviation are approximately 1000 fL and 1.3, which gives a range of approximately 750 to 1300 fL for a single standard deviation of the mean. However, the geometric standard deviation of the density distribution is 1.0023, which is again substantially lower than that of volume. This narrow distribution can also be observed when comparing the means from multiple experiments, as shown in Figure 2.2-1. Whereas the volume range is approximately 500 fL, the density range is 0.005 g/mL, which is similar to the distribution of an individual measurement. If we consider the coefficient of variation, or the standard deviation divided by the mean, then we have further evidence of the relative tightness of the density

distribution; whereas the CV of the 300 mosm volume measurement is approximately 0.83, that of the density measurement is 0.067.

We can take this analysis one step further, and consider what the variability might be if take into account that the bounds on cell density are the density of water (1 g/mL), and the density of RNA, which is the densest biochemical material (approximately 1.9 g/mL) (160). In other words, if the cell were 100% water, then its density would be 1 g/mL, and if the cell were 100% RNA, then its density would be 1.9 g/mL. Doing this will help address the issue of whether volume and mass have a greater CV simply due to the mass and volume range being so much larger than the density range. Using this new scale, a density of 1.058 g/mL would be 6.4% of the distance from the minimum to the maximum value.

We can now apply the standard deviation for volume to this narrower density range. If we apply (i.e. multiply and divide, since we are using parameters for a log-normal distribution) the volume standard deviation of 1.3 to the value 6.4%, we obtain a range of 4.9% to 8.3%. This translates to a density range of 1.044 to 1.074, which is still wider than the actual density range of 1.056 to 1.061.

Based on this analysis, we can therefore conclude that density is in fact a more tightly regulated property than volume, and not simply due to a narrower possible range of parameters. Rather, this suggests that density is regulated more tightly on a biological level.

A.3 Measurements of biophysical properties of miscellaneous suspension and adherent cells

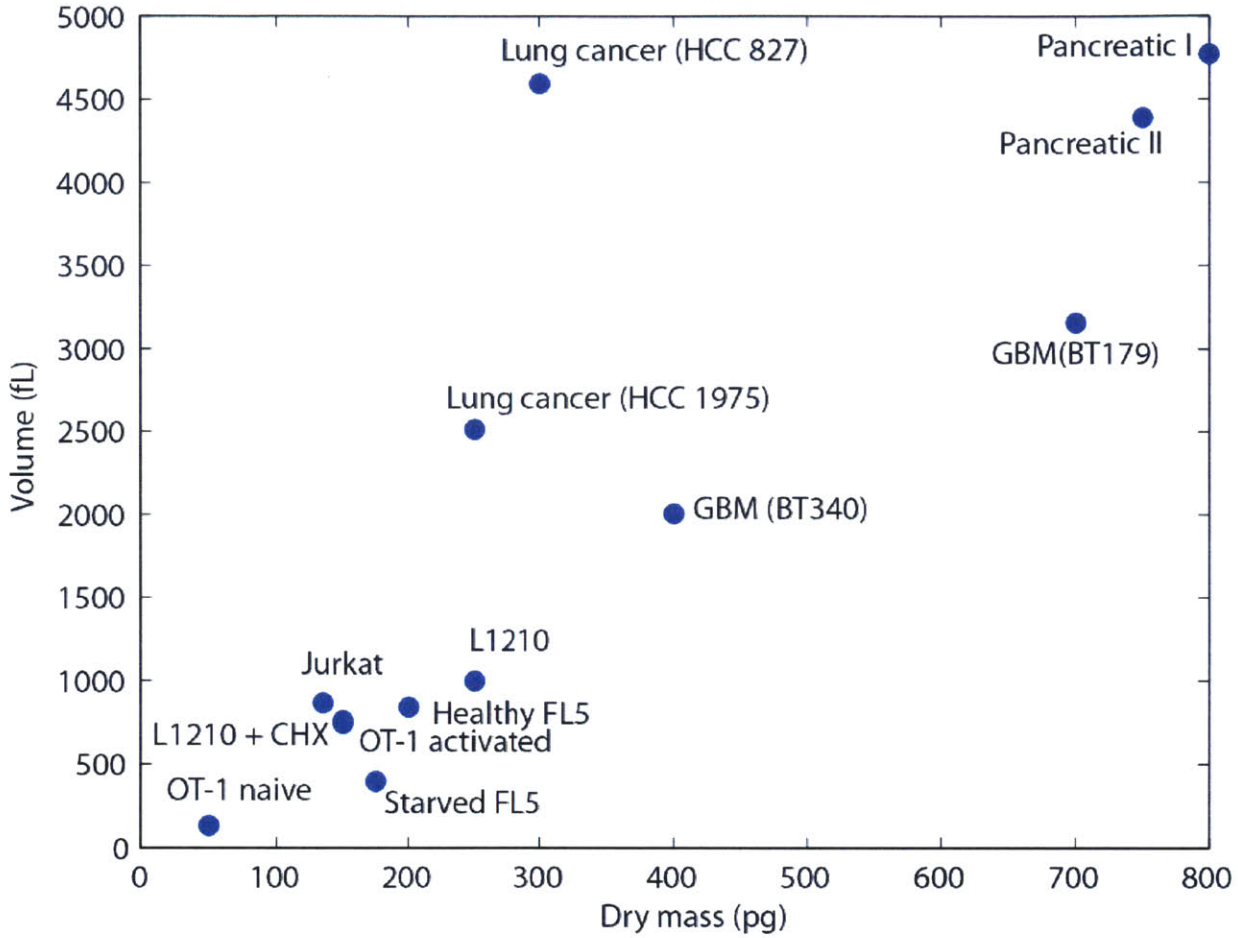

Figure A.3-1. Volume vs. dry mass of multiple adherent and suspension cell lines and primary cells.
Cell volume was measured using a Coulter counter, and cell dry mass was measured with an SMR using the methods described in §1.2.1.1. Adherent cell lines include pancreatic cells and lung cancer cells. Suspension cell lines include L1210, FL5, and Jurkat cells. Starved FL5 refers to cells that have been depleted of IL-3 for 24 h. L1210 + CHX refers to cells that have been treated with 10 μg/mL cycloheximide for 24 h prior to measurement. Primary cells include OT-1 cells. OT-1 cells are CD8+ T cells derived from an OT-1 mouse. Naïve OT-1 refers to cells that have not yet been activated, and OT-1 activated refers to cells that have been activated with 2 μg/mL $OVA_{257-264}$ peptide (SIINFEKL) for 24 h. BT340 and BT179 are patient-derived glioblastoma multiforme (GBM) cell lines.

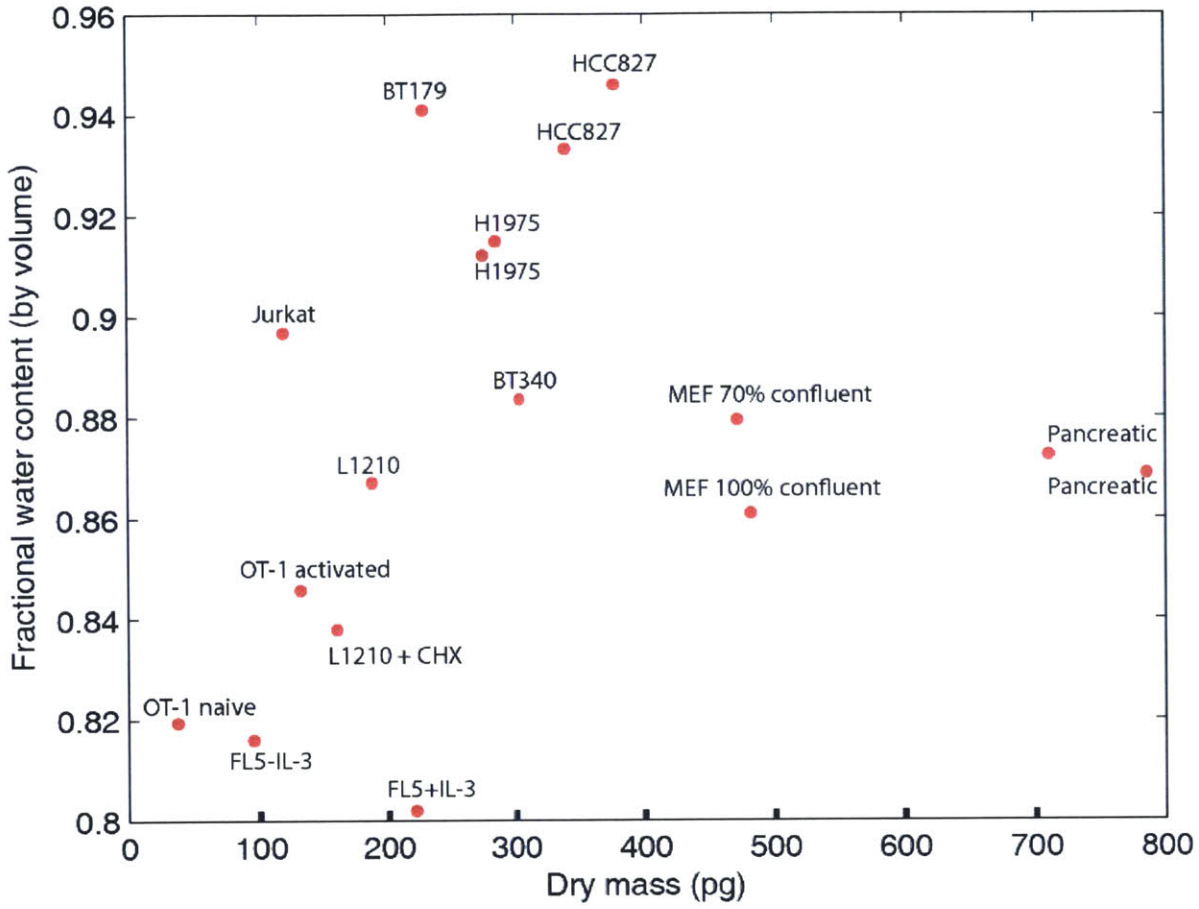

Figure A.3-2. Fractional water content (by volume) vs dry mass of multiple adherent and suspension cell lines and primary cells.
Total water volume was determined based on calculations described in §1.2.1.1. Fractional water volume was determined by dividing total water volume by total cell volume, determined using a Coulter counter. Cells shown in this figure match cells shown in Figure A.3-1. Shown here additionally is a mouse embryonic fibroblast (MEF) cell line cultured to varying levels of confluency (70% or 100%).

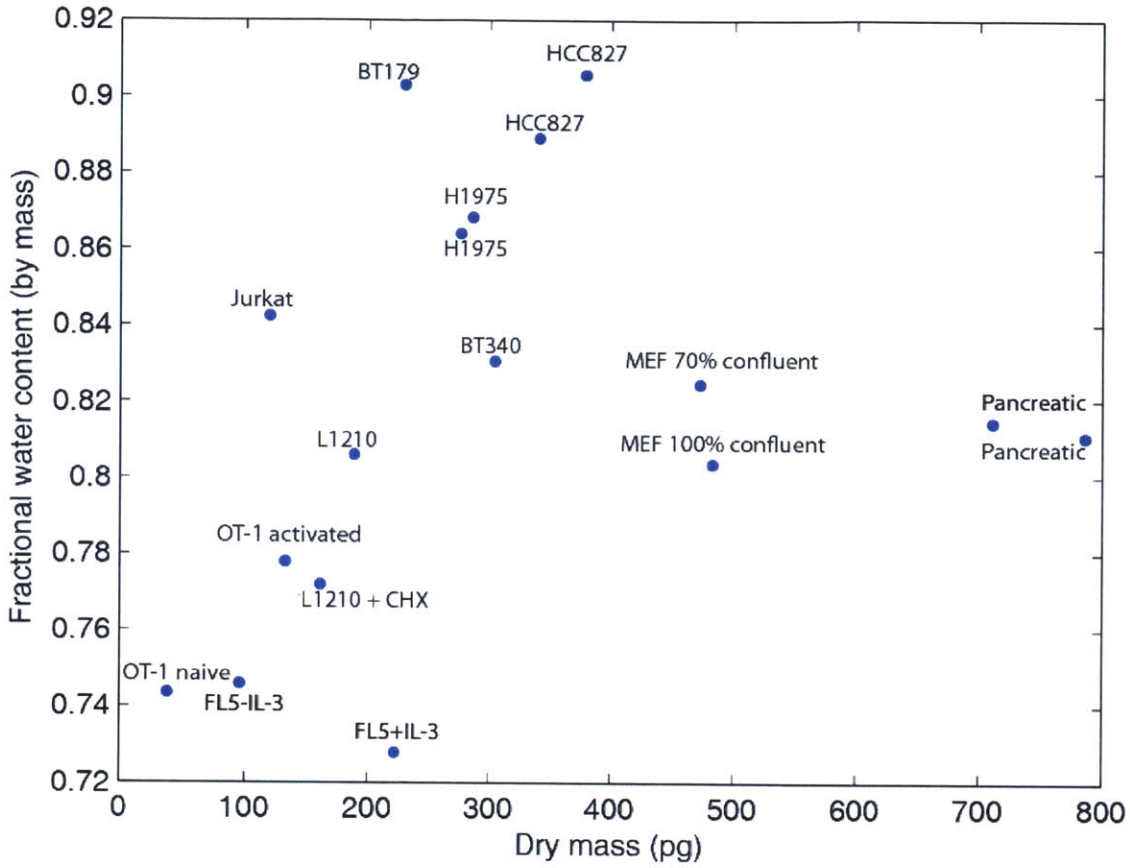

Figure A.3-1. Fractional water content (by mass) vs dry mass of multiple adherent and suspension cell lines and primary cells.
Total water mass was determined based on calculations described in §1.2.1.1. Fractional water volume was determined by dividing total water volume by total cell mass, determined using a volume calculated with Coulter counter and the dry mass measured from an SMR. Cells shown in this figure match cells shown in Figure A.3-.

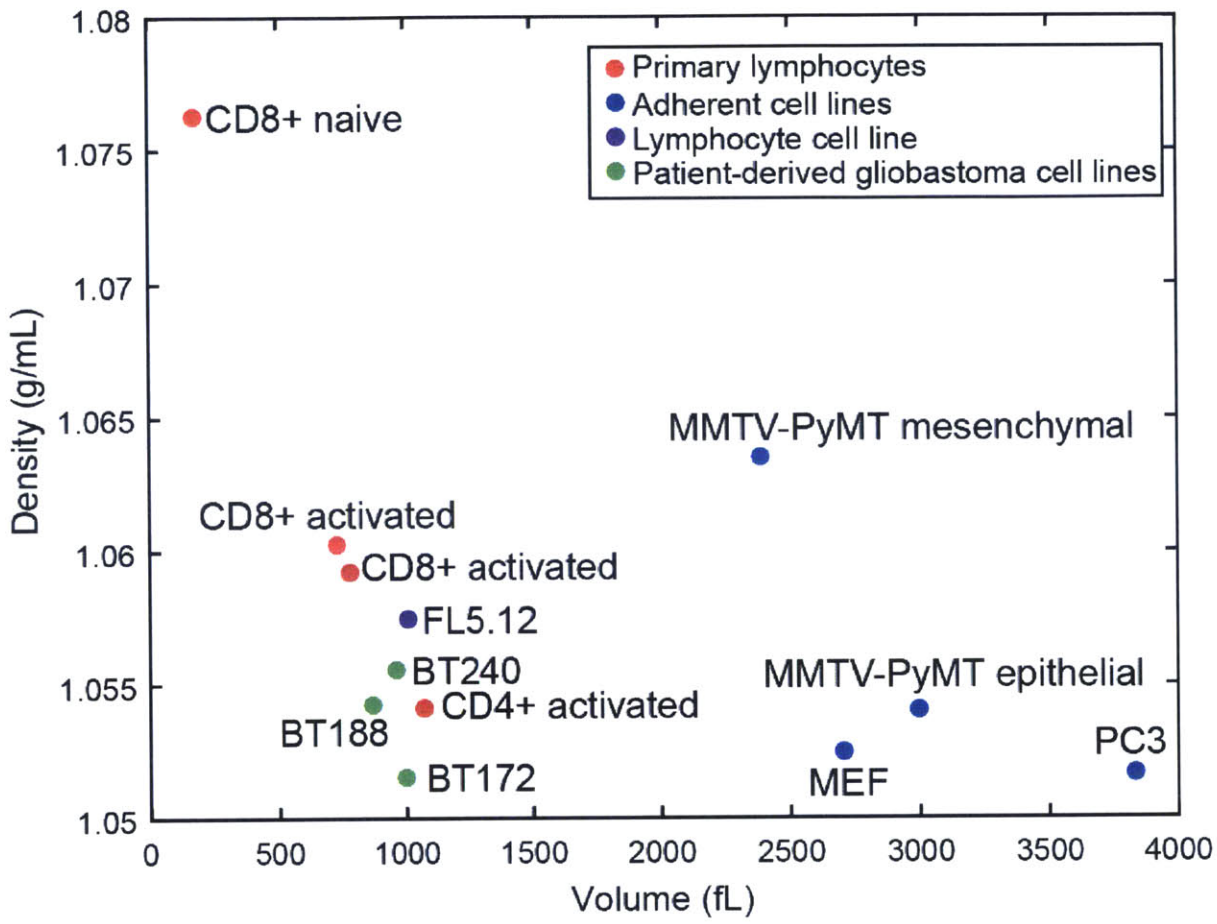

Figure A.3-4. Density vs. volume of multiple cell types.
Primary CD8+ lymphocytes were obtained from an OT-1 mouse and activated as described in Figure A.3-2. Primary CD4+ lymphocytes were obtained from a wild-type human sample. MMTV-PyMT cells are derived from a mammary carcinoma of a *Snail*$^{YFP/+}$*; MMTV-PyMT* mouse, and are differentiated from an epithelial to a mesenchymal phenotype (98). PC3 cells are a human prostate cell cancer line. MEF cells are a mouse embryonic fibroblast cell line. FL5.12 cells are a murine pro-B lymphocyte line, as described in great detail elsewhere in this document, especially Chapter 3. BT172, BT188 and BT240 represent patient-derived cell lines of glioblastoma multiforme.

Bibliography

1. Haussinger, D., F. Lang, and W. Gerok. 1994. Regulation of cell function by the cellular hydration state. Am. J. Physiol. - Endocrinol. Metab. 267: E343–E355.

2. Al-Habori, M. 2001. Macromolecular crowding and its role as intracellular signalling of cell volume regulation. Int. J. Biochem. Cell Biol. 33: 844–864.

3. Ross, C. a, and M. a Poirier. 2004. Protein aggregation and neurodegenerative disease. Nat. Med. 10 Suppl: S10–S17.

4. Ellis, R.J. 2001. Macromolecular crowding: obvious but underappreciated. Trends Biochem. Sci. 26: 597–604.

5. Minton, A.P. 2000. Implications of macromolecular crowding for protein assembly. Curr. Opin. Struct. Biol. 10: 34–39.

6. Ma, Q., J.B. Fan, Z. Zhou, B.R. Zhou, S.R. Meng, J.Y. Hu, J. Chen, and Y. Liang. 2012. The contrasting effect of macromolecular crowding on amyloid fibril formation. PLoS One. 7.

7. Bryan, A.K., A. Goranov, A. Amon, and S.R. Manalis. 2010. Measurement of mass, density, and volume during the cell cycle of yeast. Proc. Natl. Acad. Sci. 107: 999–1004.

8. Son, S., J.H. Kang, S. Oh, M.W. Kirschner, T.J. Mitchison, and S.R. Manalis. Resonant microchannel volume and mass measurements show that suspended cells swell during mitosis. J. Cell Biol. .

9. Bortner, C.D., and J. a Cidlowski. 2004. The role of apoptotic volume decrease and ionic homeostasis in the activation and repression of apoptosis. Pflugers Arch. 448: 313–8.

10. Maeno, E., Y. Ishizaki, T. Kanaseki, a Hazama, and Y. Okada. 2000. Normotonic cell shrinkage because of disordered volume regulation is an early prerequisite to apoptosis. Proc. Natl. Acad. Sci. U. S. A. 97: 9487–92.

11. Poulsen, K. a, E.C. Andersen, C.F. Hansen, T.K. Klausen, C. Hougaard, I.H. Lambert, and E.K. Hoffmann. 2010. Deregulation of apoptotic volume decrease and ionic movements in multidrug-resistant tumor cells: role of chloride channels. Am. J. Physiol. Cell Physiol. 298: C14–25.

12. Zetterberg, A., and D. Killander. 1965. Quantitative cytophotometric and autoradiographic studies on the rate of protein synthesis during interphase in mouse fibroblasts in vitro. Exp. Cell Res. 40: 1–11.

13. Brown, a F., and G. a Dunn. 1989. Microinterferometry of the movement of dry matter in fibroblasts. J. Cell Sci. 92 (Pt 3): 379–89.

14. Davies, H., M. Wilkins, J. Chayen, and L. La Cour. 1954. The Use of the Interference Microscope to Determine Dry Mass In Living Cells and as a Quantitative Cytochemical Method. J. Microscpial Sci. 95: 271–304.

15. Farinas, J., and a S. Verkman. 1996. Cell volume and plasma membrane osmotic water permeability in epithelial cell layers measured by interferometry. Biophys. J. 71: 3511–22.

16. Mir, M., Z. Wang, Z. Shen, M. Bednarz, R. Bashir, I. Golding, S.G. Prasanth, and G. Popescu. 2011. Optical measurement of cycle-dependent cell growth. Proc. Natl. Acad. Sci. U. S. A. 108: 13124–9.

17. Barer, R., K. Ross, and S. Tkaczyk. 1953. Refractometry of Living Cells. Nature. 171: 720–724.

18. Tsuchihashi, H., M. Katagi, M. Nishikawa, M. Tatsuno, H. Nishioka, A. Nara, E. Nishio, and C. Petty. 1997. Determination of Methamphetamine and Its Related Compounds Using Fourier Transform Raman Spectroscopy. Appl. Spectrosc. 51: 1796–1799.

19. Petry, R., M. Schmitt, and J. Popp. 2003. Raman spectroscopy--a prospective tool in the life sciences. Chemphyschem. 4: 14–30.

20. Kang, J.W., N. Lue, C.-R. Kong, I. Barman, N.C. Dingari, S.J. Goldfless, J.C. Niles, R.R. Dasari, and M.S. Feld. 2011. Combined confocal Raman and quantitative phase microscopy system for biomedical diagnosis. Biomed. Opt. Express. 2: 2484.

21. Kang, J.W., F.T. Nguyen, N. Lue, R.R. Dasari, and D. a Heller. 2012. Measuring Uptake Dynamics of Multiple Identi fi able Carbon Nanotube Species via High-Speed Confocal Raman Imaging of Live Cells. .

22. Park, J.-M., J.-Y. Lee, J.-G. Lee, H. Jeong, J.-M. Oh, Y.J. Kim, D. Park, M.S. Kim, H.J. Lee, J.H. Oh, S.S. Lee, W.-Y. Lee, and N. Huh. 2012. Highly efficient assay of circulating tumor cells by selective sedimentation with a density gradient medium and microfiltration from whole blood. Anal. Chem. 84: 7400–7.

23. Friedman, S.L., and F.J. Roll. 1987. Isolation and culture of hepatic lipocytes, Kupffer cells, and sinusoidal endothelial cells by density gradient centrifugation with Stractan. Anal. Biochem. 161: 207–18.

24. Wolff, D.A., and H. Pertoft. 1972. Separation of HeLa cells by colloidal silica density gradient centrifugation. I . Separation and partial synchrony of mitotic cells. J. Cell Biol. 55: 579–585.

25. Burg, T.P., M. Godin, S.M. Knudsen, W. Shen, G. Carlson, J.S. Foster, K. Babcock, and S.R. Manalis. 2007. Weighing of biomolecules, single cells and single nanoparticles in fluid. Nature. 446: 1066–1069.

26. Burg, T. 2005. Suspended microchannel resonators for biomolecular detection. .

27. Son, S., A. Tzur, Y. Weng, P. Jorgensen, J. Kim, M.W. Kirschner, and S.R. Manalis. 2012. Direct observation of mammalian cell growth and size regulation. Nat. Methods. 9: 910–2.

28. Son, S. 2013. Precise single cell monitoring reveals principles of cell growth. .

29. Godin, M., F.F. Delgado, S. Son, W.H. Grover, A.K. Bryan, A. Tzur, P. Jorgensen, K. Payer, A.D. Grossman, M.W. Kirschner, and S.R. Manalis. 2010. Using buoyant mass to measure the growth of single cells. Nat. Methods. .

30. Feijó Delgado, F. 2013. Measuring compositional and growth properties of single cells. .

31. Feijó Delgado, F., N. Cermak, V.C. Hecht, S. Son, Y. Li, S.M. Knudsen, S. Olcum, J.M. Higgins, J. Chen, W.H. Grover, and S.R. Manalis. 2013. Intracellular water exchange for measuring the dry mass, water mass and changes in chemical composition of living cells. PLoS One. 8: e67590.

32. Grover, W.H., A.K. Bryan, M. Diez-Silva, S. Suresh, J.M. Higgins, and S.R. Manalis. 2011. Measuring single-cell density. Proc. Natl. Acad. Sci. U. S. A. 108: 10992–6.

33. Bryan, A.K., V.C. Hecht, W. Shen, K. Payer, W.H. Grover, and S.R. Manalis. 2014. Measuring single cell mass, volume, and density with dual suspended microchannel resonators. Lab Chip. 14: 569–76.

34. Bosslet, K., R. Ruffmann, P. Altevogt, and V. Schirrmacher. 1981. A rapid method for the isolation of metastasizing tumour cells from internal organs with the help of isopycnic density-gradient centrifugation in Percoll. Br. J. Cancer. 44: 356–362.

35. Haff, L.A. 1979. Production of Ficoll, Percoll, and albumin gradients by the freeze-thaw method. Prep. Biochem. 9: 149–156.

36. Van Veldhoven, P.P., E. Baumgart, and G.P. Mannaerts. 1996. Iodixanol (Optiprep), an improved density gradient medium for the iso-osmotic isolation of rat liver peroxisomes. Anal. Biochem. 237: 17–23.

37. Ford, T., J. Graham, and D. Rickwood. 1994. Iodixanol: a nonionic iso-osmotic centrifugation medium for the formation of self-generated gradients. Anal. Biochem. 220: 360–6.

38. Bryan, A. 2011. Measuring single cell density. .

39. Lee, J., A.K. Bryan, and S.R. Manalis. 2011. High precision particle mass sensing using microchannel resonators in the second vibration mode. Rev. Sci. Instrum. .

40. Knudsen, S.M., M.G. von Muhlen, and S.R. Manalis. 2012. Quantifying particle coatings using high-precision mass measurements. Anal. Chem. 84: 1240–2.

41. Short, K.W., S. Carpenter, J.P. Freyer, and J.R. Mourant. 2005. Raman Spectroscopy Detects Biochemical Changes Due to Proliferation in Mammalian Cell Cultures. Biophys. J. 88: 4274–4288.

42. Suresh, S. 2007. Biomechanics and biophysics of cancer cells. Acta Biomater. 3: 413–38.

43. Cross, S.E., Y.-S. Jin, J. Rao, and J.K. Gimzewski. 2007. Nanomechanical analysis of cells from cancer patients. Nat. Nanotechnol. 2: 780–3.

44. Guck, J., S. Schinkinger, B. Lincoln, F. Wottawah, S. Ebert, M. Romeyke, D. Lenz, H.M. Erickson, R. Ananthakrishnan, D. Mitchell, J. Käs, S. Ulvick, and C. Bilby. 2005. Optical deformability as an inherent cell marker for testing malignant transformation and metastatic competence. Biophys. J. 88: 3689–98.

45. Weaver, W.M., P. Tseng, A. Kunze, M. Masaeli, A.J. Chung, J.S. Dudani, H. Kittur, R.P. Kulkarni, and D. Di Carlo. 2014. Advances in high-throughput single-cell microtechnologies. Curr. Opin. Biotechnol. 25: 114–23.

46. Tse, H.T.K., D.R. Gossett, Y.S. Moon, M. Masaeli, M. Sohsman, Y. Ying, K. Mislick, R.P. Adams, J. Rao, and D. Di Carlo. 2013. Quantitative diagnosis of malignant pleural effusions by single-cell mechanophenotyping. Sci. Transl. Med. 5: 212ra163.

47. Wirtz, D., K. Konstantopoulos, and P.C. Searson. 2011. The physics of cancer : the role of physical interactions and mechanical forces in metastasis. Nat. Rev. Cancer. 11: 512–522.

48. Chowdhury, F., S. Na, D. Li, Y.-C. Poh, T.S. Tanaka, F. Wang, and N. Wang. 2010. Material properties of the cell dictate stress-induced spreading and differentiation in embryonic stem cells. Nat. Mater. 9: 82–8.

49. Gossett, D.R., H.T.K. Tse, S.A. Lee, Y. Ying, A.G. Lindgren, O.O. Yang, J. Rao, A.T. Clark, and D. Di Carlo. 2012. Hydrodynamic stretching of single cells for large population mechanical phenotyping. Proc. Natl. Acad. Sci. 109: 7630–7635.

50. Théry, M., and M. Bornens. 2008. Get round and stiff for mitosis. HFSP J. 2: 65–71.

51. Tsai, M.A., R.E. Waugh, and P.C. Keng. 1996. Cell cycle-dependence of HL-60 cell deformability. Biophys. J. 70: 2023–9.

52. Suresh, S., J. Spatz, J.P. Mills, a Micoulet, M. Dao, C.T. Lim, M. Beil, and T. Seufferlein. 2005. Connections between single-cell biomechanics and human disease states: gastrointestinal cancer and malaria. Acta Biomater. 1: 15–30.

53. Lam, W.A., M.J. Rosenbluth, and D.A. Fletcher. 2007. Chemotherapy exposure increases leukemia cell stiffness. Blood. 109: 3505–3509.

54. Pietuch, A., B.R. Brückner, and A. Janshoff. 2013. Membrane tension homeostasis of epithelial cells through surface area regulation in response to osmotic stress. Biochim. Biophys. Acta - Mol. Cell Res. 1833: 712–722.

55. Maroudas, A. 1979. Physicochemical properties of articular cartilage. In: Freeman MAR, editor. Adult Articular Cartilage. Pitman Medical. pp. 215–290.

56. Schneiderman, R., D. Keret, and A. Maroudas. 1986. Effects of mechanical and osmotic pressure on the rate of glycosaminoglycan synthesis in the human adult femoral head cartilage: an in vitro study. J. Orthop. Res. 4: 393–408.

57. Bush, P.G., and A.C. Hall. 2001. The osmotic sensitivity of isolated and in situ bovine articular chondrocytes. J. Orthop. Res. 19: 768–778.

58. Guilak, F., G.R. Erickson, and H.P. Ting-Beall. 2002. The effects of osmotic stress on the viscoelastic and physical properties of articular chondrocytes. Biophys. J. 82: 720–7.

59. Go, W.Y., X. Liu, M.A. Roti, F. Liu, and S.N. Ho. 2004. NFAT5 ¯TonEBP mutant mice define osmotic stress as a critical feature of the lymphoid microenvironment. PNAS. 101: 10673–10678.

60. González-Cruz, R.D., V.C. Fonseca, and E.M. Darling. 2012. Cellular mechanical properties reflect the differentiation potential of adipose-derived mesenchymal stem cells. Proc. Natl. Acad. Sci. U. S. A. 109: E1523–9.

61. Lee, W.C., H. Shi, Z. Poon, L.M. Nyan, T. Kaushik, G. V Shivashankar, J.K.Y. Chan, C.T. Lim, J. Han, and K.J. Van Vliet. 2014. Multivariate biophysical markers predictive of mesenchymal stromal cell multipotency. Proc. Natl. Acad. Sci. U. S. A. 111: E4409–18.

62. Byun, S., S. Son, D. Amodei, N. Cermak, J. Shaw, J.H. Kang, V.C. Hecht, M.M. Winslow, T. Jacks, P. Mallick, and S.R. Manalis. 2013. Characterizing deformability and surface friction of cancer cells. Proc. Natl. Acad. Sci. U. S. A. 110: 7580–5.

63. Miermont, A., F. Waharte, S. Hu, M.N. McClean, S. Bottani, S. Léon, and P. Hersen. 2013. Severe osmotic compression triggers a slowdown of intracellular signaling,

which can be explained by molecular crowding. Proc. Natl. Acad. Sci. U. S. A. 110: 5725–30.

64. Zhou, E.H., X. Trepat, C.Y. Park, G. Lenormand, M.N. Oliver, S.M. Mijailovich, C. Hardin, D. a Weitz, J.P. Butler, and J.J. Fredberg. 2009. Universal behavior of the osmotically compressed cell and its analogy to the colloidal glass transition. Proc. Natl. Acad. Sci. U. S. A. 106: 10632–7.

65. Anderson, N.G., W.W. Harris, A.A. Barber, C.T. Rankin, and E.L. Candler. 1966. Separation of subcellular components and viruses by combined rate- and isopycnic-zonal centrifugation. Natl. Cancer Inst. Monogr. 21.

66. Panijpan, B. 1977. The Buoyant Density of DNA and the G + C Content. J. Chem. Educ. 54: 172–173.

67. Fischer, H., I. Polikarpov, and A.F. Craievich. 2004. Average protein density is a molecular-weight-dependent function. Protein Sci. 13: 2825–2828.

68. Minton, A.P. 2006. How can biochemical reactions within cells differ from those in test tubes? J. Cell Sci. 119: 2863–2869.

69. Bathe, M., A. Shirai, C.M. Doerschuk, and R.D. Kamm. 2002. Neutrophil transit times through pulmonary capillaries: the effects of capillary geometry and fMLP-stimulation. Biophys. J. 83: 1917–33.

70. Steltenkamp, S., C. Rommel, J. Wegener, and A. Janshoff. 2006. Membrane stiffness of animal cells challenged by osmotic stress. Small. 2: 1016–20.

71. Sung, K.L., G.W. Schmid-Schönbein, R. Skalak, G.B. Schuessler, S. Usami, and S. Chien. 1982. Influence of physicochemical factors on rheology of human neutrophils. Biophys. J. 39: 101–6.

72. Spagnoli, C., A. Beyder, S. Besch, and F. Sachs. 2008. Atomic force microscopy analysis of cell volume regulation. Phys. Rev. E. 78: 031916.

73. Xu, J., M. Millard, X. Ren, O.T. Cox, and A. Erdreich-Epstein. 2010. c-Abl mediates endothelial apoptosis induced by inhibition of integrins v 3 and v 5 and by disruption of actin. Blood. 115: 2709–2718.

74. Huang, S., C.S. Chen, and D.E. Ingber. 1998. Control of cyclin D1, p27(Kip1), and cell cycle progression in human capillary endothelial cells by cell shape and cytoskeletal tension. Mol. Biol. Cell. 9: 3179–3193.

75. Stapulionis, R., S. Kolli, and M.P. Deutscher. 1997. Efficient mammalian protein synthesis requires an intact F-actin system. J. Biol. Chem. 272: 24980–24986.

76. Pelling, A.E., F.S. Veraitch, C.P.-K. Chu, C. Mason, and M.A. Horton. 2009. Mechanical dynamics of single cells during early apoptosis. Cell Motil. Cytoskeleton. 66: 409–422.

77. Bruno, S., B. Ardelt, J.S. Skierski, F. Traganos, and Z. Darzynkiewicz. 1992. Different effects of staurosporine, an inhibitor of protein kinases, on the cell cycle and chromatin structure of normal and leukemic lymphocytes. Cancer Res. 52: 470–473.

78. Tee, A.R., and C.G. Proud. 2001. Staurosporine inhibits phosphorylation of translational regulators linked to mTOR. Cell Death Differ. 8: 841–849.

79. Castellano, F., C.L. Clainche, D. Patin, M.F. Carlier, and P. Chavrier. 2001. A WASp-VASP complex regulates actin polymerization at the plasma membrane. EMBO J. 20: 5603–5614.

80. Kuehn, H.S., M.Y. Jung, M.A. Beaven, D.D. Metcalfe, and A.M. Gilfillan. 2011. Prostaglandin E2 activates and utilizes mTORC2 as a central signaling locus for the regulation of mast cell chemotaxis and mediator release. J. Biol. Chem. 286: 391–402.

81. Sun, S.-Y. 2013. mTOR kinase inhibitors as potential cancer therapeutic drugs. Cancer Lett. 340: 1–8.

82. Thoreen, C.C., S. a Kang, J.W. Chang, Q. Liu, J. Zhang, Y. Gao, L.J. Reichling, T. Sim, D.M. Sabatini, and N.S. Gray. 2009. An ATP-competitive mammalian target of rapamycin inhibitor reveals rapamycin-resistant functions of mTORC1. J. Biol. Chem. 284: 8023–32.

83. Laporte, J.D., P.E. Moore, R.A. Panettieri, W. Moeller, J. Heyder, S.A. Shore, D. Johanne, and A. Reynold. 1998. Prostanoids mediate IL-1-beta-induced beta-adrenergic hyporesponsiveness in human airway smooth muscle cells. Am J Physiol. 275: 491–501.

84. Tang, D., J.M. Lahti, J. Grenet, and V.J. Kidd. 1999. Cycloheximide-induced T-cell death is mediated by a Fas-associated death domain-dependent mechanism. J. Biol. Chem. 274: 7245–52.

85. Mattson, M.P., and K. Furukawa. 1997. Anti-apoptotic actions of cycloheximide : blockade of programmed cell death or induction of programmed cell life ? Apoptosis. 2: 257–264.

86. Liu, X., J.-M. Yang, S.S. Zhang, X.-Y. Liu, and D.X. Liu. 2010. Induction of cell cycle arrest at G1 and S phases and cAMP-dependent differentiation in C6 glioma by low concentration of cycloheximide. BMC Cancer. 10: 684.

87. Kerrigan, M.J.P., C.S.V. Hook, A. Qusous, and A.C. Hall. 2006. Regulatory Volume Increase (RVI) by In Situ and Isolated Bovine Articular Chondrocytes. J. Cell. Physiol. 209: 481–492.

88. Wakatsuki, T., B. Schwab, N.C. Thompson, and E.L. Elson. 2001. Effects of cytochalasin D and latrunculin B on mechanical properties of cells. J. Cell Sci. 114: 1025–1036.

89. King, J.T., E.J. Arthur, C.L. Brooks, and K.J. Kubarych. 2014. Crowding induced collective hydration of biological macromolecules over extended distances. J. Am. Chem. Soc. 136: 188–194.

90. Bertrand, R., E. Solary, P. O'Connor, K.W. Kohn, and Y. Pommier. 1994. Induction of a common pathway of apoptosis by staurosporine. Exp. Cell Res. 211: 314–321.

91. Tee, A.R., and C.G. Proud. 2002. Caspase cleavage of initiation factor 4E-binding protein 1 yields a dominant inhibitor of cap-dependent translation and reveals a novel regulatory motif. Mol. Cell. Biol. 22: 1674–1683.

92. Straight, A.F., A. Cheung, J. Limouze, I. Chen, N.J. Westwood, J.R. Sellers, and T.J. Mitchison. 2003. Dissecting temporal and spatial control of cytokinesis with a myosin II Inhibitor. Science. 299: 1743–1747.

93. Okuda, a, and G. Kimura. 1988. Non-specific elongation of cell cycle phases by cycloheximide in rat 3Y1 cells, and specific reduction of G1 phase elongation by simian virus 40 large T antigen. J. Cell Sci. 91 (Pt 2): 295–302.

94. Thoreen, C.C., and D.M. Sabatini. 2009. Rapamycin inhibits mTORC1 , but not completely. Autophagy. 5: 725–726.

95. Terada, N., H.R. Patel, K. Takase, K. Kohno, a C. Nairn, and E.W. Gelfand. 1994. Rapamycin selectively inhibits translation of mRNAs encoding elongation factors and ribosomal proteins. Proc. Natl. Acad. Sci. U. S. A. 91: 11477–11481.

96. Thomas, G., and M.N. Hall. 1997. TOR signalling and control of cell growth. Curr. Opin. Cell Biol. 9: 782–787.

97. Boise, L.H., M. González-García, C.E. Postema, L. Ding, T. Lindsten, L.A. Turka, X. Mao, G. Nuñez, and C.B. Thompson. 1993. bcl-x, a bcl-2-related gene that functions as a dominant regulator of apoptotic cell death. Cell. 74: 597–608.

98. Bagnall, J. 2015. Tumor cell deformability in the metastatic cascade. .

99. Limpert, E., W. a. Stahel, and M. Abbt. 2001. Log-normal Distributions across the Sciences: Keys and Clues. Bioscience. 51: 341.

100. Gabriele, S., M. Versaevel, P. Preira, and O. Théodoly. 2010. A simple microfluidic method to select, isolate, and manipulate single-cells in mechanical and biochemical assays. Lab Chip. 10: 1459–1467.

101. Rathmell, J.C., E.A. Farkash, W. Gao, and C.B. Thompson. 2001. IL-7 enhances the survival and maintains the size of naive T cells. J. Immunol. 167: 6869–76.

102. Mizel, S.B. 1989. The interleukins. FASEB J. 3: 2379–2388.

103. Duke, R., and J. Cohen. 1986. IL-2 addiction: withdrawal of growth factor activates a suicide program in dependent T cells. Lymphokine Res. 5: 289–299.

104. Parijs, L. V., and A.K. Abbas. 1998. Homeostasis and self-tolerance in the immune system: turning lymphocytes off. Science (80-.). 280: 243–248.

105. Valentin, M., and E. Yang. 2008. Autophagy is activated, but is not required for the G0 function of BCL-2 or BCL-xL. Cell Cycle. 7: 2762–2768.

106. Cornish, G.H., L. V Sinclair, D.A. Cantrell, and I. Fields. 2006. Differential regulation of T cell growth by IL-2 and IL-15. Blood. 108: 600–609.

107. Rolf, J., M. Zarrouk, D.K. Finlay, M. Foretz, B. Viollet, and D. a. Cantrell. 2013. AMPKα1: A glucose sensor that controls CD8 T-cell memory. Eur. J. Immunol. 43: 889–896.

108. Pearce, E.L. 2010. Metabolism in T cell activation and differentiation. Curr. Opin. Immunol. 22: 314–20.

109. Goldrath, A.W., P. V Sivakumar, M. Glaccum, M.K. Kennedy, M.J. Bevan, C. Benoist, D. Mathis, and E. a Butz. 2002. Cytokine requirements for acute and basal homeostatic proliferation of naive and memory CD8+ T cells. J. Exp. Med. 195: 1515–1522.

110. Lum, J.J., R.J. DeBerardinis, and C.B. Thompson. 2005. Autophagy in metazoans: cell survival in the land of plenty. Nat. Rev. Mol. Cell Biol. 6: 439–448.

111. Van der Windt, G.J.W., B. Everts, C. Chang, J.D. Curtis, T.C. Freitas, E. Amiel, E.J. Pearce, and E.L. Pearce. 2011. Mitochondrial respiratory capacity is a critical regulator of CD8 + T cell memory development. Immunity. 36: 68–78.

112. Grayson, J.M., A.J. Zajac, J.D. Altman, and R. Ahmed. 2000. Cutting edge: Increased expression of Bcl-2 in antigen-specific memory CD8+ T cells. J. Immunol. 164: 3950–3954.

113. Nunez, G., D. Hockenberry, T. McDonnell, C. Sorensen, and S. Korsmeyer. 1991. Bcl-2 maintains B cell memory. Nature. 353: 71–73.

114. Rathmell, J.C., M.G. Vander Heiden, M.H. Harris, K.A. Frauwirth, and C.B. Thompson. 2000. In the absence of extrinsic signals, nutrient utilization by lymphocytes is insufficient to maintain either cell size or viability. Mol. Cell. 6: 683–92.

115. Xu, X., K. Araki, S. Li, J.-H. Han, L. Ye, W.G. Tan, B.T. Konieczny, M.W. Bruinsma, J. Martinez, E.L. Pearce, D.R. Green, D.P. Jones, H.W. Virgin, and R. Ahmed. 2014.

Autophagy is essential for effector CD8+ T cell survival and memory formation. Nat. Immunol. 15.

116. Berard, M., K. Brandt, S.B. Paus, and D.F. Tough. 2003. IL-15 promotes the survival of naive and memory phenotype CD8+ T cells. J. Immunol. 170: 5018–5026.

117. Vander Heiden, M.G., N.S. Chandel, P.T. Schumacker, and C.B. Thompson. 1999. Bcl-xL prevents cell death following growth factor withdrawal by facilitating mitochondrial ATP/ADP exchange. Mol. Cell. 3: 159–67.

118. Lum, J.J., D.E. Bauer, M. Kong, M.H. Harris, C. Li, T. Lindsten, and C.B. Thompson. 2005. Growth factor regulation of autophagy and cell survival in the absence of apoptosis. Cell. 120: 237–48.

119. Edinger, A.L., and C.B. Thompson. 2002. Akt maintains cell size and survival by increasing mTOR-dependent nutrient uptake. Mol. Biol. Cell. 13: 2276–2288.

120. Lunt, S.Y., V. Muralidhar, A.M. Hosios, W.J. Israelsen, D.Y. Gui, L. Newhouse, M. Ogrodzinski, V. Hecht, K. Xu, P.N.M. Acevedo, D.P. Hollern, G. Bellinger, T.L. Dayton, S. Christen, I. Elia, A.T. Dinh, G. Stephanopoulos, S.R. Manalis, M.B. Yaffe, E.R. Andrechek, S.-M. Fendt, and M.G. Vander Heiden. 2015. Pyruvate kinase isoform expression alters nucleotide synthesis to impact cell proliferation. Mol. Cell. 57: 95–107.

121. Chambliss, A.B., P.H. Wu, W.C. Chen, S.X. Sun, and D. Wirtz. 2013. Simultaneously defining cell phenotypes, cell cycle, and chromatin modifications at single-cell resolution. FASEB J. 27: 2667–76.

122. Levine, B., and D.J. Klionsky. 2004. Development by self-digestion : molecular mechanisms and biological functions of autophagy. Dev. Cell. 6: 463–477.

123. Ayna, G., D. V Krysko, A. Kaczmarek, G. Petrovski, P. Vandenabeele, and L. Fésüs. 2012. ATP release from dying autophagic cells and their phagocytosis are crucial for inflammasome activation in macrophages. PLoS One. 7: e40069.

124. Sekulić, A., C.C. Hudson, J.L. Homme, P. Yin, D.M. Otterness, L.M. Karnitz, and R.T. Abraham. 2000. A direct linkage between the phosphoinositide 3-kinase-AKT signaling pathway and the mammalian target of rapamycin in mitogen-stimulated and transformed cells. Cancer Res. 60: 3504–3513.

125. Wieman, H.L., J.A. Wofford, and J.C. Rathmell. 2007. Cytokine stimulation promotes glucose uptake via phosphatidylinositol-3 kinase/Akt regulation of Glut1 activity and trafficking. Mol. Biol. Cell. 18: 1437–1446.

126. Cruz, R., L. Hedden, D. Boyer, M.G. Kharas, D.A. Fruman, and K.K. Lee-Fruman. 2005. S6 kinase 2 potentiates interleukin-3-driven cell proliferation. J. Leukoc. Biol. 78: 1378–1385.

127. Lum, J.J., D.E. Bauer, M. Kong, M.H. Harris, C. Li, T. Lindsten, and C.B. Thompson. 2005. Growth factor regulation of autophagy and cell survival in the absence of apoptosis. Cell. 120: 237–48.

128. Kabeya, Y., N. Mizushima, T. Ueno, a Yamamoto, T. Kirisako, T. Noda, E. Kominami, Y. Ohsumi, and T. Yoshimori. 2000. LC3, a mammalian homologue of yeast Apg8p, is localized in autophagosome membranes after processing. EMBO J. 19: 5720–8.

129. Vander Heiden, M.G., D.R. Plas, J.C. Rathmell, C.J. Fox, M.H. Harris, and C.B. Thompson. 2001. Growth factors can influence cell growth and survival through effects on glucose metabolism. Mol. Cell. Biol. 21: 5899–5912.

130. Wellen, K.E., C. Lu, A. Mancuso, J.M.S. Lemons, M. Ryczko, J.W. Dennis, J.D. Rabinowitz, H. a. Coller, and C.B. Thompson. 2010. The hexosamine biosynthetic pathway couples growth factor-induced glutamine uptake to glucose metabolism. Genes Dev. 24: 2784–2799.

131. Lunt, S.Y., and M.G. Vander Heiden. 2011. Aerobic glycolysis: meeting the metabolic requirements of cell proliferation. Annu. Rev. Cell Dev. Biol. 27: 441–64.

132. Rathmell, J.C. 2004. B-cell homeostasis: digital survival or analog growth? Immunol. Rev. 197: 116–28.

133. Koppenol, W.H., P.L. Bounds, and C. V Dang. 2011. Otto Warburg's contributions to current concepts of cancer metabolism. Nat. Rev. Cancer. 11: 325–337.

134. Hogquist, K., S.C. Jameson, W.R. Heath, J.L. Howard, M.J. Bevan, and F.R. Carbone. 1994. T cell receptor antagonist peptides induce positive selection. Cell. 76: 17–27.

135. Balkwill, F.R., and F. Burke. 1989. The cytokine network. Immunol. Today. 10: 299–304.

136. Puleston, D.J., H. Zhang, T.J. Powell, E. Lipina, S. Sims, I. Panse, A.S. Watson, V. Cerundolo, A.R. Townsend, P. Klenerman, and A.K. Simon. 2014. Autophagy is a critical regulator of memory CD8(+) T cell formation. Elife. 3: 1–21.

137. Kim, D.-H., and D. Wirtz. 2015. Cytoskeletal tension induces the polarized architecture of the nucleus. Biomaterials. 48: 161–172.

138. Stone, J.D., A.S. Chervin, and D.M. Kranz. 2009. T-cell receptor binding affinities and kinetics: impact on T-cell activity and specificity. Immunology. 126: 165–176.

139. Corse, E., R. a Gottschalk, and J.P. Allison. 2011. Strength of TCR-peptide/MHC interactions and in vivo T cell responses. J. Immunol. 186: 5039–5045.

140. Berzofsky, J. a, J.D. Ahlers, and I.M. Belyakov. 2001. Strategies for designing and optimizing new generation vaccines. Nat. Rev. Immunol. 1: 209–219.

141. Chen, H., Z.M. Ndhlovu, D. Liu, L.C. Porter, J.W. Fang, S. Darko, M. a Brockman, T. Miura, Z.L. Brumme, A. Schneidewind, A. Piechocka-Trocha, K.T. Cesa, J. Sela, T.D. Cung, I. Toth, F. Pereyra, X.G. Yu, D.C. Douek, D.E. Kaufmann, T.M. Allen, and B.D. Walker. 2012. TCR clonotypes modulate the protective effect of HLA class I molecules in HIV-1 infection. Nat. Immunol. 13: 691–700.

142. Xia, Z., H. Chen, S. Kang, T. Huynh, J.W. Fang, P. a Lamothe, B.D. Walker, and R. Zhou. 2014. The complex and specific pMHC interactions with diverse HIV-1 TCR clonotypes reveal a structural basis for alterations in CTL function. Sci. Rep. 4: 4087.

143. McMahan, R.H., J. a McWilliams, K.R. Jordan, S.W. Dow, D.B. Wilson, and J.E. Slansky. 2006. Relating TCR-peptide-MHC affintiy to immunogenicity for the design of tumor vaccines. J. Clin. Invest. 116: 2543–2551.

144. Zhong, S., K. Malecek, L. a Johnson, Z. Yu, E. Vega-Saenz de Miera, F. Darvishian, K. McGary, K. Huang, J. Boyer, E. Corse, Y. Shao, S. a Rosenberg, N.P. Restifo, I. Osman, and M. Krogsgaard. 2013. T-cell receptor affinity and avidity defines antitumor response and autoimmunity in T-cell immunotherapy. Proc. Natl. Acad. Sci. U. S. A. 110: 6973–8.

145. Edwards, L.J., V.I. Zarnitsyna, J.D. Hood, B.D. Evavold, and C. Zhu. 2012. Insights into T cell recognition of antigen: Significance of two-dimensional kinetic parameters. Front. Immunol. 3: 1–9.

146. Altman, J.D., P. a Moss, P.J. Goulder, D.H. Barouch, M.G. McHeyzer-Williams, J.I. Bell, a J. McMichael, and M.M. Davis. 1996. Phenotypic analysis of antigen-specific T lymphocytes. Science. 274: 94–96.

147. Nguyen, B., F. a. Tanious, and W.D. Wilson. 2007. Biosensor-surface plasmon resonance: Quantitative analysis of small molecule-nucleic acid interactions. Methods. 42: 150–161.

148. Dustin, M.L., S.K. Bromley, M.M. Davis, and C. Zhu. 2001. Identification of self through two-dimensional chemistry and synapses. Annu. Rev. Cell Dev. Biol. 17: 133–157.

149. Huppa, J.B., M. Axmann, M. a Mörtelmaier, B.F. Lillemeier, E.W. Newell, M. Brameshuber, L.O. Klein, G.J. Schütz, and M.M. Davis. 2010. TCR-peptide-MHC interactions in situ show accelerated kinetics and increased affinity. Nature. 463: 963–967.

150. Huang, J., V.I. Zarnitsyna, B. Liu, L.J. Edwards, N. Jiang, B.D. Evavold, and C. Zhu. 2010. The kinetics of two-dimensional TCR and pMHC interactions determine T-cell responsiveness. Nature. 464: 932–936.

151. Irvine, D.J., M. a Purbhoo, M. Krogsgaard, and M.M. Davis. 2002. Direct observation of ligand recognition by T cells. Nature. 419: 845–849.

152. Tan, W.-H., and S. Takeuchi. 2007. A trap-and-release integrated microfluidic system for dynamic microarray applications. Proc. Natl. Acad. Sci. U. S. A. 104: 1146–1151.

153. Kimmerling, R.J., G.L. Szeto, J.W. Li, A.S. Genshaft, S.W. Kazer, J. de R. Borrajo, P.C. Blainey, D.J. Irvine, A.K. Shalek, and S.R. Manalis. A microfluidic platform enabling single cell RNA-seq of multigenerational lineages. Nat. Commun. .

154. Verweij, C.L., M. Geerts, and L. a Aarden. 1991. Activation of interleukin-2 gene transcription via the T- cell surface molecule CD28 is mediated through an NF-kB-like response element. J.Biol.Chem. 266: 14179–14182.

155. Rong, Y.-P., G. Bultynck, A.S. Aromolaran, F. Zhong, J.B. Parys, H. De Smedt, G. a Mignery, H.L. Roderick, M.D. Bootman, and C.W. Distelhorst. 2009. The BH4 domain of Bcl-2 inhibits ER calcium release and apoptosis by binding the regulatory and coupling domain of the IP3 receptor. Proc. Natl. Acad. Sci. U. S. A. 106: 14397–14402.

156. Schneider, U., H. Schwenk, and G. Bornkamm. 1977. Characterization of EBV-genome negative "null" and "T" cell lines derived from children with acute lymphoblastic leukemia and leukemic transformed non-Hodgkin lymphoma. Int. J. Cancer. 19: 621–6.

157. Yurinskaya, V.E., A. V. Moshkov, A. V. Wibberley, F. Lang, M. a. Model, and A. a. Vereninov. 2012. Dual Response of Human Leukemia U937 Cells to Hypertonic Shrinkage: Initial Regulatory Volume Increase (RVI) and Delayed Apoptotic Volume Decrease (AVD). Cell. Physiol. Biochem. 30: 964–973.

158. Bortner, C.D., and J. a Cidlowski. 2007. Cell shrinkage and monovalent cation fluxes: role in apoptosis. Arch. Biochem. Biophys. 462: 176–88.

159. Ernest, N.J., C.W. Habela, and H. Sontheimer. 2008. Cytoplasmic condensation is both necessary and sufficient to induce apoptotic cell death. J. Cell Sci. 121: 290–297.

160. Adams, R.L., J.T. Knowler, and D.P. Leader. 1986. The Biochemistry of the Nucleic Acids. 10th ed. New York: Chapman and Hall.